NTNU – Trondheim
Norwegian University of
Science and Technology

Catalytic partial oxidation of methane at moderate temperatures

Sophie Anne Amelie Glas

Chemical Engineering and Biotechnology
Submission date: Januar 2013
Supervisor: De Chen, IKP
Co-supervisor: Anders Holmen, IKP

Norwegian University of Science and Technology
Department of Chemical Engineering

Abstract

Catalytic partial oxidation (CPO) is considered to be a promising route to produce synthesis gas from methane. In this work cobalt supported on $CeO_2-Al_2O_3$ nanocomposites calcined at temperatures ranging from 1173 K to 1473 K have been characterized and tested in a lab-scale reactor. The characterization techniques applied have been N_2 adsorption-desorption, X-ray diffraction (XRD), temperature-programmed reduction (TPR) and H_2 chemisorption. The activity testing has been done at three different furnace temperatures (923 K, 1023 K and 1123 K) at a GSHV of 75 $L_{CH_4}/g_{cat}\cdot h$ with a $CH_4:O_2:N_2$ ratio of 2:1:3.72.

In this work the major objectives have been to investigate the catalytic behavior of $Co/CeO_2-Al_2O_3$ towards CPO of methane, and whether the varying concentration of oxygen vacancies in the ceria lattice influences the catalytic activity.

The BET surface area of $CeO_2-Al_2O_3$ decreased as the calcination temperature increased. Comparison with pure Al_2O_3 calcined at corresponding temperatures confirmed the protective function of CeO_2 against Al_2O_3 phase transformation. With XRD and subsequent Rietveld refinement the crystallite size and lattice parameter of CeO_2 were found. As the former increased with increasing calcination temperature, the determination of the latter showed no clear correlation between the lattice parameter, crystallite size and presence of cobalt.

The dispersion, which was estimated with H_2 chemisorption, of cobalt on $CeO_2-Al_2O_3$ calcined at 1173 K, 1273 K and 1373 K was quite uniform, whereas it decreased for the samples calcined at 1423 K and 1473 K. There is reason to believe that the results are affected by H_2 spillover onto the CeO_2.

Catalytic partial oxidation of methane over the *in situ* reduced catalysts gave high methane conversion and selectivities towards CO and H_2, even at moderate temperatures such as 1023 K. $Co/CeO_2-Al_2O_3$ (1173 K), (1273 K) and (1373 K) showed the best performance. An enhanced activity with decreasing CeO_2 crystallite sizes has not been observed. The results support the indirect partial oxidation pathway with complete combustion in the bed entrance area and endotherm reforming in the lower part of the catalyst.

The stability of the catalysts seems limited, probably due to slow oxidation of the cobalt during time on stream and/or sintering. Mass transfer limitations are also suspected.

A cordierite monolith with an Al_2O_3 washcoat impregnated with CeO_2 and cobalt was tested in methane CPO at 1023 K with a GHSV of 8000 h^{-1}. Even though the CH_4 conversion and selectivity towards H_2 and CO were satisfactory, the stability decreased quickly.

Sammendrag

Katalytisk partiell oksidasjon av metan (CPO) blir sett på som en lovende måte å produsere syntesegass fra metan. Reaksjonen er eksoterm og forholdsvis enkel å starte opp og avslutte.

I denne masteroppgaven har en katalysator bestående av kobolt på en $CeO_2-Al_2O_3$-bærer, som har blitt kalsinert ved 1173 K-1473 K, blitt karakterisert gjennom N_2-adsorpsjon-desorpsjon, røntngendiffraksjon (XRD), temperaturprogrammert reduksjon (TPR) og H_2-kjemisorpsjon. Aktivitetstestingen har blitt utført ved tre ulike ovnstemperaturer (923 K, 1023 K og 1123 K) med en GHSV på 75 $L_{CH_4}/g_{kat}\cdot t$ med et forhold mellom CH_4, O_2 og N_2 på henholdsvis 2, 1 og 3.72.

Formålet med denne oppgaven har vært å undersøke den katalytiske aktiviteten til $Co/CeO_2-Al_2O_3$ i katalytisk partiell oksidasjon av metan ved moderate temperaturer, og om den varierende konsentrasjonen av oksygenledighet i CeO_2-gitteret påvirker den katalytiske aktiviteten.

BET-overflatearealet til $CeO_2-Al_2O_3$ sank ved økende kalsineringstemperatur. CeO_2 har vist seg å beskytte Al_2O_3 mot faseendringer ved høye temperaturer, noe som ble bekreftet ved sammenligning med rent Al_2O_3 kalsinert ved tilsvarende temperaturer som $CeO_2-Al_2O_3$. Krystallstørrelsen og gitterparameteren til CeO_2 ble funnet ved XRD. Krystallstørrelsen økte med økende kalsineringstemperatur, mens det ikke ble funnet noen klar korrelasjon mellom gitterparameteren, krystallstørrelsen og tilstedeværelsen av kobolt.

Dispersjonen til kobolt ble estimert ved H_2-kjemisorpsjon. Det ble funnet at dispersjonen for kobolt på $CeO_2-Al_2O_3$ kalsinert ved 1173 K, 1273 K og 1373 K var like. Dispersjonen for de øvrige katalysatorene økte med bærerens kalsineringstemperatur. Det er grunn til å tro at kjemisorpsjonsresultatene er påvirket av hydrogen "spillover" på CeO_2, noe som betyr at en del av hydrogenmengden er adsorbert av CeO_2. Dette begrenser gyldigheten til resultatene.

Katalytisk partiell oksidasjon av metan over *in situ*-reduserte katalysatorer ga høy omsetning av metan og CO- og H_2-selektivitet. $Co/CeO_2-Al_2O_3$ (1173 K), (1273 K) and (1373 K) viste den beste yteevnen. En økt aktivitet med minkende CeO_2-størrelse ble ikke observert. Resultatene underbygger teorien om en indirekte reaksjonsmekanisme, hvor fullstendig forbrenning foregår øverst i katalysatorlaget, mens endoterme reformeringsreaksjoner skjer nedstrøms i katalysatorlaget.

Stabiliteten til katalysatorene ser ut til å være begrenset, sannsynligvis på grunn av langsom oksidering av kobolt og/eller sintring. Det formodes at massetransport begrenser reaksjonen.

En cordierite monolitt, påført en Al_2O_3-washcoat og impregnert med CeO_2 og kobolt, ble også testet i CPO ved 1023 K med en GHSV på 8000 t^{-1}. Metanomsetningen og selektiviteten til CO og H_2 var relativt høy, men katalysatorens aktivitet sank rimelig raskt.

Preface

This master thesis is written on behalf of the Catalysis group at the Department of Chemical Engineering, NTNU. The work has been performed between September 10, 2012 and February 1, 2013.
The work related to this thesis encompasses the building up of the experimental rig, including thorough leak tests, reactor modification, MFC and GC calibration and trial runs for optimizing the experimental conditions, as well as catalyst characterization and testing. The catalysts used were synthesized during a research project done in the spring semester of 2012, but have to a large extent been characterized during the thesis period unless otherwise stated.

First of all I would like to thank my supervisors Professor De Chen and Prof. Emeritus Anders Holmen for their advice, guidance and support, and for always keeping their office doors open for me. Furthermore, thanks to post. doc. Sara Boullosa Eiras for help with the rig and other practical issues.

Thanks to the administrative and technical staff at the Department of Chemical Engineering at NTNU, and in particular Karin Wiggen Dragsten for practical and mental support during the activities in the lab, Arne Fossum and Harry Brun for supplying chemicals, gases and equipment (especially gloves), Jan Morten Roel and the other guys at the workshop for patience and help while I was starting up the rig (and I apologize for all the times I disturbed during your 2 o'clock coffee break), and Lisbeth Roel for having an answer to everything.
I would also like to thank Asbjørn Lindvåg for teaching me the ins and outs of the GC and for checking in on me from time to time, and glassblower Astrid and her staff for fixing my broken reactors again and again (and again...).

Thanks to Marte and Ingrid for getting me to the top of Kilimanjaro. If we can do that, we can do anything! Special thanks to Christina Carlsen for proofreading the report.
Finally I would like to thank my friends, family and *mijn topvriendje* Daan for the love, support and encouragement.

I hereby declare that this is an independent work according to the exam regulations of the Norwegian University of Science and Technology.

Trondheim, 30.01.2013

Sophie Anne Amelie Glas

Symbols and abbreviations

Symbols

A_0	Area occupied by N_2 at 77 K (0.162 nm^2)
A_m	Cross sectional area of metal atom (nm^2)
d	Lattice spacing [Å]
$d_{\text{bed entrance}}$	Distance from entrance of catalyst bed [cm]
$d_{\text{b.e.}}$	Distance from entrance of catalyst bed [cm]
d_m	Diameter of metal particle [nm]
D	Dispersion [%]
f_s	Surface fraction of the active phase
F	Stoichiometric factor
F_i	Molar flow of component i [mol/s]
k_B	Boltzmann constant (1.3806503 $\cdot$ 10^{-23} J/K)
K	Constant depending on the crystallite shape
L	Length of a particle
m_i	Mass of i [g]
M_i	Molar mass of i [g/mol]
n	Order of reflection
n_i	Mole of i [mol]
N_0	Number of molecules
N_A	Avogadro's number (6.022$\cdot$10^{23} atoms/mol)
P	Pressure [bar]
P_0	Equilibrium pressure [bar]
r	Rate of reaction
S_{BET}	BET surface area [m^2/g]
S_i	Selectivity towards i
S/V	Surface-to-volume ratio
T	Temperature [K] [°C]
$T_{\text{calc.}}$	Calcination temperature of $CeO_2-Al_2O_3$ [K]
v_{ads}	Volume gas adsorbed (chemisorption) [cm^3/g STP]
V_a	Total volume adsorbed (BET) [cm^3/g STP]
V_0	Volume adsorbed in first monolayer [cm^3/g STP]
x_m	Weight fraction of metal
X_i	Conversion of i [%]

Greek symbols

α	Slope of BET plot
β	Full width at half maximum (FWHM)
ΔH^0_{298}	Reaction enthalpy at 298 K [kJ/mol]
ε_C	Error in the carbon balance [%]
η	Intersection of y-axis of BET plot
θ	Adsorption layer
θ	Angle
λ	Wavelength
ρ	Density (kg/m^3)
χ	Ratio of the desorption rate constants

Abbreviations

Ads.	Adsorption
a.u.	Arbitrary units
BET	Brunauer Emmett Teller
BJH	Barrett Joyner Halenda
CA	Citric acid
C-A	Ceria-alumina ($CeO_2-Al_2O_3$)
calc.	Calcination
CPO	Catalytic partial oxidation
CRR	Combustion and reforming reactions
Des.	Desorption
EG	Ethylene glycol
fcc	Face centered cubic
FID	Flame ionization detector
FWHM	Full width at half maximum
GC	Gas chromatograph
GHSV	Gas hourly space velocity
hcp	Hexagonal close-packed
IUPAC	International Union of Pure and Applied Chemistry
M	Metal
MFC	Mass flow controller
OSC	Oxygen storage capacity
PEG	Polyethylene glycol
RT	Response time
STY	Site-time yield
TCD	Thermal conductivity detector
TEM	Transmission electron microscopy
TOF	Turn over frequency
TOS	Time on stream
TPR	Temperature programmed reduction
vol.	Volume
wt.	Weight
XRD	X-ray diffraction

Contents

Chapter 1

Introduction

Proportionally with the world's increasing population, as well as the augmented standard of living in up-and-coming industrializing countries, the energy demand rises relentlessly. One is continuously looking for new energy sources and ways to exploit the resources in a more efficient and sustainable manner. Today, fossil fuels are still the most important and valuable resources, of which natural gas perhaps has the most promising prospectives towards the future, both in abundance, applicability and sustainability [1].

Natural gas, of which methane is the main constituent, is found in large quantities all over the world [2, 3]. Next to methane, natural gas consists of other hydrocarbons, CO_2, N_2 and some elementary sulfur, of which the fractions depend on the origin of the gas [4]. Estimations indicate that at the current consumption level, we look at more than 250 years of recoverable natural gas resources to come [1].

How to convert methane into chemicals of higher value has been a field of study with increasing attention over the past 30 years. However, the industrial implementation has been limited. Using natural gas as feedstock for the synthesis of higher-value hydro carbon products or fuels costs more than using oil as feedstock. Transporting and storing natural gas is also costly, especially in remote areas where the infrastructure is scarce. Research has been done to make the processing, transport and storage of natural gas more feasible and economically profitable [3]. The most economical route for the conversion of methane into chemicals with higher value is to convert it into synthesis gas, also called syngas, a gaseous mixture of CO and H_2. Syngas is mainly used in the methanol synthesis, the hydroformulation of alkenes to aldehydes and alcohols and in the synthesis of larger hydrocarbons (Fischer-Tropsch) [4]. There are three reactions that convert methane into syngas [3]. The only large-scale process is steam reforming, where methane reacts with H_2O. Steam reforming is a highly endothermic reaction and is thermodynamically favored by high temperatures (>1200 °C) and high pressures. The production yields a rather low H_2-to-CO ratio and is limited by the external heat supply rate. Other reactions are dry reforming (reaction between CO_2 and methane) and partial oxidation [3], which forms the background for this research project. Already in 1929 H. Liander suggested that partial combustion of methane would be advantageous in order to

obtain H_2 for ammonia production [5]. From 1929 to the 1980s there was limited interest in partial oxidation of methane, partly due to the start of the oil adventure. During the 1990s and up until today the focus on developing methods for methane processing has increased.

Catalytic partial oxidation (CPO) of methane has an internal energy supply due to its exothermicity which makes it more flexible regarding the production location, changing operation conditions and the total scale of production than for instance steam reforming [6]. The relatively small scale production of hydrogen is in particular interesting for applications such as fuel cells.

A variety of catalysts, both powdered and monolithic, have been tested for catalytic partial oxidation of methane, among them noble metals such as Pd, Pt, Rh and Ru, as well as conventional catalysts such as Co and Ni, on different supports [2]. Prereduced cobalt is known to be active towards CPO [7, 6] and is relative inexpensive compared to noble metals. Al_2O_3 is a widely used support material, and in particular the phase γ-Al_2O_3 due to its large surface area. However, at high temperatures γ-Al_2O_3 undergoes a phase transformation to the less thermally stable low surface area α-Al_2O_3. This structural change might also lead to blocking of pores, making the catalyst physically inaccessible. Coating the alumina with CeO_2 has successfully proved to protect the alumina by delaying the phase transformation with respect to temperature, as well as enhancing the dispersion of the metal [8]. The use of CeO_2 is also of interest due to the oxygen release/storage abilities of ceria [9]. A previous study in this research group has found that heat treatment at different temperatures influences the oxygen vacancies in the ceria lattice, which might contribute to the partial oxidation of methane [8].

This thesis will investigate the catalytic behavior of $Co/CeO_2-Al_2O_3$ and the effect of the calcination temperature of the $CeO_2-Al_2O_3$ nanocomposites on the catalytic partial oxidation of methane. The catalysts will also be characterized by means of conventional characterization methods such as N_2 adsorption-desorption, X-ray diffraction, H_2 chemisorption and temperature-programmed reduction.

Chapter 2

Theory

2.1 Catalytic partial oxidation of methane

Direct catalytic partial oxidation of methane is part of a system of reversible and irreversible reactions. The most important reactions are given in Table 2.1.

Table 2.1: Reactions related to the partial oxidation of methane [2, 3, 6, 8]

	ΔH^0_{298} [kJ/mol]		
$CH_4 + 2\,O_2 \rightarrow CO_2 + 2\,H_2O$	-803	(1)	Total oxidation
$CH_4 + \frac{1}{2}\,O_2 \rightarrow CO + 2\,H_2$	-36	(2)	Direct catalytic partial oxidation
$CH_4 + O_2 \rightarrow CO_2 + 2\,H_2$	-319	(3)	Partial oxidation
$CO + H_2O \rightleftharpoons CO_2 + H_2$	-41	(4)	Water-gas shift (WGS)
$CH_4 + H_2O \rightleftharpoons CO + 3\,H_2$	206	(5)	Steam reforming
$CH_4 + CO_2 \rightleftharpoons 2\,CO + 2\,H_2$	247	(6)	Dry reforming (CO_2 reforming)
$CO + H_2 \rightleftharpoons C + H_2O$	-113	(7)	CO reduction
$CH_4 \rightleftharpoons C + 2\,H_2$	74.9	(8)	Cracking
$2\,CO \rightleftharpoons CO_2 + C$	-172.4	(9)	Boudouard
$CO + \frac{1}{2}\,O_2 \rightarrow CO_2$	-283	(10)	CO preferential route
$H_2 + \frac{1}{2}\,O_2 \rightarrow H_2O$	-242	(11)	H_2 oxidation
$CO + 3\,H_2 \rightleftharpoons CH_4 + H_2O$	-206.2	(12)	Methanation

Reaction (2) in Table 2.1 is the direct route of partial oxidation of methane to synthesis gas. However, all the other equations in Table 2.1 will affect the final product and by-products according to the thermodynamic equilibrium. Quite some work has been done in order to find a catalyst or catalytic system with a high methane conversion and selectivity towards CO and H_2 [6, 10, 11].

As can be seen from Table 2.1 direct catalytic partial oxidation of methane is favored by low pressure, since the forward reaction generates more product molecules than

reactant molecules [12], and low temperatures. Low temperatures also favor total oxidation, whereas the reforming reactions are favored by high temperatures. Next to finding a suitable catalyst that preferentially catalyzes reaction (2), a temperature compromise can give the desired products. Simulations done by Enger et al. show that the conversion and selectivity towards CO and H_2 increase fast at temperatures below 950 K [2]. The increase continues at higher temperatures but flattens out as the value exceeds 90%. The plots in the review of Enger et al. indicate a methane conversion above 90% achieved at temperatures above 1050 K at thermodynamic equilibrium, whereas the CO and H_2 selectivity reaches 90% at 950 K [2].

At high temperatures (>1273 K) H_2 and CO are the favored products [10]. However, at such high temperatures special requirements concerning the reactor material have to be met. In addition, the catalyst stability is a problem at temperatures of this order of magnitude. Thus, for commercial applications this is not optimal. CPO of methane at moderate temperatures, that is, temperatures between 973 K and 1073 K, has several advantages. The construction materials are less expensive as they do not need to be suitable for extreme temperatures. In addition, the start-up and shut-down of the process is faster and solid-state reactions between the components can be suppressed [6]. For industrial use the partial oxidation of methane has not been a great success, mostly due to the fact that oxygen reacts with the primary products, forming CO_2 and water (reaction (10) and (11)). These compounds can be converted to syngas via steam or dry reforming, reactions requiring energy, as can be seen in Table 2.1.

Mass and heat transfer

When an exotherm chemical reaction is catalyzed heat removal from the catalyst is important in order to control the temperature and avoid local hotspots. Catalytic partial oxidation is a reaction where a temperature profile across the catalyst bed is often observed [2]. The nonuniform temperature also hinders investigation of the kinetics and reaction mechanism as such studies require isothermal conditions. A catalyst with excellent thermal conductivity will contribute to a fast transfer of the excess heat away from the part of the catalyst where the reaction takes place.

The use of a monolith catalyst might improve the heat and mass transfer by means of higher space velocity and therefore a shorter residence time.

Reaction mechanism

The reaction mechanism of partial oxidation of methane is widely disputed. There is a number of reasons for why determining the reaction mechanism is not straight forward [13]. CPO is a fast exothermic reaction which complicates the mechanism study [2]. For a reaction system such as the one CPO is a part of (Table 2.1), it is likely that more than one mechanism occurs. A change in operating conditions such as O/C ratio, temperature and space velocity can change the mechanism. When a catalyst is involved the system changes by means of which reaction and mechanism

is the most dominating. Besides, the catalyst can change over time and interact with the support, which might also influence the mechanism.

In literature, two possible reaction mechanisms have been proposed; direct and indirect partial oxidation of methane [2, 13, 14]. The indirect mechanism is also called the combustion-reforming reaction mechanism (CRR). At the beginning of the catalyst bed total oxidation (reaction (1)) takes place, generating CO_2 and H_2O and an extensive amount of heat, followed by the endothermic reforming reactions (reaction (5) and (6)) and water-gas shift reaction (reaction (4)). The theory is often supported by the temperature profile of the catalyst bed [6, 14].

Supporters of the direct route, i.e. reaction (2) in Table 2.1, claim that CO and H_2 are the primary products and that they are produced at the beginning of the catalyst bed or monolith. Hickman and Schmidt proposed a reaction mechanism supporting this theory [15, 16].

Today, the indirect mechanism is the most accepted theory [17]. Schmidt et al. present an overview of literature supporting either the direct or indirect reaction mechanism theory [13], based on the review article of York et al. [14]. This thesis will not elaborate further on the reaction mechanism of catalytic partial oxidation of methane as this is not relevant for the scope of the work.

Kinetics

As with the reaction mechanism, the kinetics of CPO is difficult to determine. First of all it depends on the reaction mechanism. Secondly, the reaction happens fast such that mass transfer limitations might occur. Heat transfer limitations, hotspots, surface coverage and the oxidation state of the active metal can also influence the kinetic measurements [13]. Rule number one is to eliminate the transport limitations. This can be done by using small catalyst particles, obtaining a low conversion and keep a low or moderate temperature, such that there are no temperature gradients [4]. A low metal loading, dilution of the catalyst and/or the reacting species are measures that can be taken.

2.2 The catalyst

The catalytic partial oxidation of methane requires a catalyst that among other things can catalyze the dissociation of H from CH_4. The bond dissociation enthalpy for $H-CH_3$ is 438 kJ/mol. In addition, the catalyst must have a high selectivity towards H_2 and CO, suppress the formation of H_2O and CO_2 and be resistant to deactivation at high temperatures. Coke formation (carbon deposition) and sintering of the metal are the primary reasons for catalyst deactivation in the partial oxidation of methane. During sintering the number of active sites is decreased. It can also speed up the formation of coke due to the large metal ensembles that are formed [18].

Catalysts suitable for CPO of methane are nickel, cobalt, and noble metals such

as iridium, palladium, platinum, rhodium and ruthenium, mostly supported on an oxide-based material [2]. In this work a cobalt catalyst supported on ceria-alumina is employed.

2.2.1   Cobalt

Cobalt has been widely studied as the active metal catalyst in partial oxidation of methane [2, 6, 10, 18, 19]. Even though Pt and Rh are superior catalysts, cobalt is cheaper and hence an attractive alternative. As with all types of catalytic systems there has to be a compromise between conversion, selectivity and costs. The costs are especially related to the abundance of the catalysts and its life-time.

Several researchers have proved that the active site for partial oxidation of methane is the metal [20]. The activity and selectivity of the reaction is dependent of the oxidation state of the metal. Cobalt can exist in two oxidation states, Co^{2+} and Co^{3+}. Co_3O_4 typically catalyses complete oxidation, whereas Co^0 favors partial oxidation [21, 6]. The structural characteristics of the Co catalyst therefore depend on the nature of the support, the calcination temperature and the loading of Co [18]. The size and shape of the metal particles in a reduced catalyst is affected by the reducibility of the catalyst, which again is related to the interaction between the metal and the support. The stronger the interaction, the more difficult the reduction [22]. Cobalt has the tendency to oxidize, so in order to improve the reducibility at lower temperatures a promoter might be added. At temperatures below 690 K cobalt has a hexagonal close-packed (hcp) structure. The crystal structure changes to face-centered cubic (fcc) at temperatures between 690 K and 1766 K, the latter being the melting point of cobalt [23].
When supported by alumina, $CoAl_2O_3$ and Co_2AlO_4 can be formed at high temperatures (>1273 K), leading to deactivation [24]. A lot of other supports have therefore been investigated [2], among other oxides of rare earth metals such as ceria [8]. Other routes to deactivation are carbon deposition at high temperatures [25].

2.2.2   Alumina

Alumina, Al_2O_3, is one of the most used catalyst supports due to its remarkable thermal and mechanical stability. Its non-reducibility is another beneficial property [20]. Alumina exists in different forms, depending on its origin and (heat) treatment. An important precursor for alumina used in catalysis is boehmite [26]. Through dehydration by heating boehmite is transformed to γ-alumina at 500 °C. Further heat treatment gives δ-, θ- and eventually the most stable α-alumina [26]. Sintering of alumina is driven by the desire to lower the total surface energy [8].
A schematic presentation of the phase transition stages at different heat treatment temperatures is given in Figure 2.1.
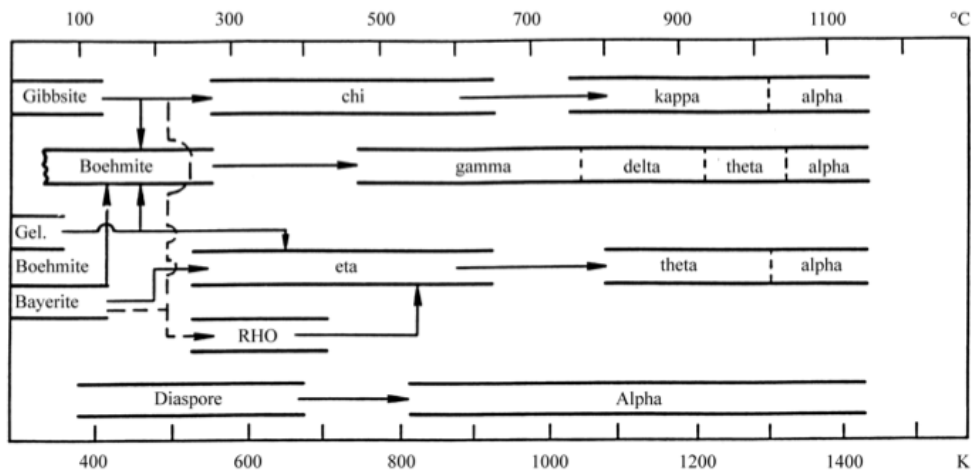
Figure 2.1: Alumina phases as a function of the thermal treatment [27].

α-alumina, is the only type of alumina with a complete crystalline structure. It is a non-porous hcp crystal with surface areas in the range of 3-5 m^2/g. Because of its high stability, α-alumina is much used in processes that require high temperatures [4].

The metastable amorphous γ-alumina is often used as a catalyst support or a membrane [26]. It has mesopores of 5-15 nm and pore volumes of 0.6 cm^3/g. The surface area is about 50-300 m^2/g [4]. Important properties of γ-alumina is its high thermal stability and that it can be formed into extrudates and pellets that are mechanically stable. γ-alumina and the other metastable forms of alumina (δ, θ) have a close packed oxygen sublattice with different interstitial aluminium configurations. α-alumina is formed when the system is approaching equilibrium due to a more ordered structure where the oxygen sublattice becomes hexagonal [28]. In α-alumina the oxygen sublattice is situated in octahedral sites instead of both octahedral and tetrahedral sites as in the metastable aluminas [28].

In solution, alumina is a polyanion of positive charge at pH values below 7, and negative charge at pH values above 7. This property makes it possible to bind many ionic catalyst precursors [4]. Alumina contains several types of hydroxyl groups. These groups play an important role in catalyst preparation because they serve as anchoring sites on the support for the catalyst precursors. The linear hydroxyl groups on alumina have an anionic (basic) character [4]. In water the surface gets an ionic character because the hydroxyls react with H$^+$ and OH$^-$. The surface charges can be determined by the pH of the solution and the isoelectric point of the oxide, the pH at which the oxide surface is neutral. At a pH below the isoelectric point the surface is negatively charged, and at a pH above the isoelectric point the surface is positively charged. The charge of the surface allows catalyst precursors of opposite charge to bind to the support.

2.2.3 Ceria

Ceria, CeO_2, is the oxide of the rare earth metal cerium and is a reducible oxide [20]. Cerium has the ability to alternate between the two oxidation states Ce^{3+} and Ce^{4+} [29, 30]. Due to the Ce^{3+}/Ce^{4+} redox couple CeO_2 can act as an oxygen buffer by storing and releasing O_2. The oxygen storage/release capacity (OSC) of ceria is high and makes ceria an excellent compound for oxidation reactions. By generating oxygen vacancies it forms interfacial active centers [29, 30]. The migration of bulk oxygen to the surface is important both for supplying the reaction with oxygen. Research shows that using ceria as an oxygen carrier enhances the formation of syngas and has a low activity towards the partial oxidation of H_2 and CO [11]. Partial oxidation of methane has even been successful by using CeO_2 as oxidant instead of O_2 [31].

CeO_2 has the crystallic fcc unit cell structure with space group Fm3m. The lattice constant, *a*, is 5.41134(12) nm, but this value changes according to the oxidation state of the oxide [9]. The oxygen storage capacity of ceria can presumably also oxidize deposited carbon, thus increasing the activity and the lifetime of the catalyst by to a certain extent prohibiting coke formation on the catalyst [3, 32]. Ceria stabilizes the support and prevents it from sintering [3], and it also enhances and stabilizes the dispersion of transition metal oxides such as cobalt [30, 33].

2.2.4 Monolithic catalysts

Monoliths are low-surface area macroporous ceramic or metallic structures with arrays of channels. They contain a number of channels oriented either in a structured way (e.g. "honeycombs"), or randomly (foams). When being used for catalytic applications the monolith must be covered with a thin layer of a porous support material, e.g. γ-alumina, by a tecnique known as dipcoating or washcoating, and subsequently a catalytic active component is applied [34, 35, 36] . When deposited on the monolith wall the support material is called the washcoat. The washcoat roughens and adds microporosity to the surface of the monolith [37].

The by far most used application for washcoated cordierite monolithic catalysts is in automotive and industrial emission control systems such as the three way catalyst (TWC) installed in gasoline cars and other environmental applications [38]. Because cordierite is not pure or abundant enough it is usually made synthetically of raw materials with high purity. This also ensures a control of the physical and chemical quality of the cordierite. Synthetic cordierite $(2\,MgO\cdot2\,Al_2O_3\cdot5\,SiO_2)$ has a range of important characteristics: A low thermal expansion coefficient that ensures excellent thermal shock resistance such that it stable at large temperature changes, a porosity and pore size distribution that makes it suitable for washcoat applications and adherence, a high melting point (1450 °C) and a compatibility with washcoats and catalysts [35, 39]. The thermal shock resistance can be improved by heat treatment or incorporating certain components. This, however, decreases the mechanical strength [35].
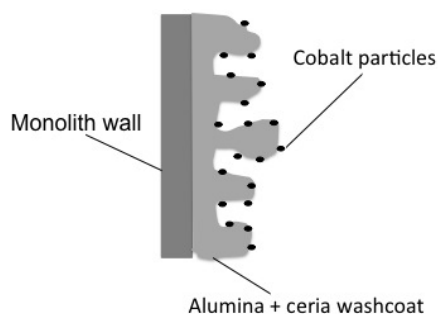
Figure 2.2: An illustration of a monolith coated with alumina-ceria support and cobalt particles

Important for a monolithic catalyst are the loading of the active phase, its dispersion and distribution on the surface of the monolith. Compared to a packed bed reactor, the catalyst content per unit reactor volume is lower with a monolithic catalyst. This implies that the active phase should be highly active by having a high loading, a high dispersion and a uniform phase distribution. The latter is influenced by the drying step in the catalyst preparation [34].

A monolithic catalytic reactor system has several advantages such as thin walls, high geometric surface area, low pressure drop (up to two orders of magnitude lower than packed beds [35]), good mass transfer and easy product separation [40]. The thin catalyst layer ensures short diffusion length and therefore fast access to the active surface of the catalyst [35]. A disadvantage of a monolithic catalyst is the limited temperature control due to the low thermal conductivity [35]. Each channel acts as an adiabatic reactor which is highly unfortunate when the selectivity is governed by the temperature, as with quite a number of endothermic and exothermic reactions [38]. Monoliths are costly and because they are difficult to recover they require stable catalysts [35].

Catalytic partial oxidation of methane over a monolithic catalyst has been done previously [41, 42, 43, 37, 16]. Most of the articles found on the subject used noble metal catalysts such as platinum, palladium and rhodium.

2.2.5   Catalyst synthesis

Impregnation

The method most often used for preparing catalysts is impregnation of a porous support with a solution of the metal precursor. There are two categories of impregnation; "wet" impregnation and "dry" impregnation, the latter also known as incipient wetness impregnation. Both of the impregnation methods are about contacting a dry solid with a solution containing some dissolved metal precursor. In wet impregnation the solid is completely dispersed in the solution, and the solute, e.g. the metal ions, diffuse into the pores. When the interaction between the metal precursor and the support is too weak wet impregnation should not be used.
Incipient wetness impregnation requires that an accurate amount of solution with dissolved precursor is added to the solid support. The exact pore volume has therefore to be determined prior to the synthesis. When adding the solution to the solid pressure driven capillary flow fills the empty pores with the solution [44]. With incipient wetness impregnation it is possible to create small metal particles. The

method is widely used in the laboratory and in the industry. Water is most often used as solvent, but organic solvents can also be used; either alone or mixed with water [45, 46]. The water content of the solvent influences the degree of aggregation of the metal precursor [45].

After impregnation the solids have to be dried in order to remove the solvent. The impregnated solid is heated up to a temperature slightly above the boiling point for the solvent, causing it to evaporate while the precursor concentration increases, leading to crystallization. When a viscous solution is used it might be challenging to replace the air in the pores with the liquid solution [44]. Drying conditions such as heating rate and temperature influence the distribution of the active metal. The metal particles might redistribute during drying because of a limited interaction between the metal and the support [47]. It is quite difficult to obtain a narrow size distribution and uniform shape of the metal particles, factors that are crucial for the catalytic activity [48]. The catalyst support will to some extent influence the morphology of the metal particles [29, 48]. In order to investigate the effect of the calcination temperature of the catalyst support it is of interest that the cobalt particles are as uniform in size and shape as possible. These properties vary when using incipient wetness impregnation with water as a solvent because the metal particles are reduced on the support and they tend to aggregate on the support surface.

Washcoating

In order to increase the specific surface area of a monolith and make the surface receptive towards deposition of the active metal a secondary support material, such as γ-alumina is added by the washcoat method. Nijhuis et al. describe different preparation methods of monolithic catalyst [49]. This thesis will comprise a simple washcoat method since optimizing the method is not a scope of this work.

When washcoating a monolith, the monolith is dipped in a slurry for a short period of time. The excess liquid is blown off with pressurized air to open the blocked channels. The monolith is subsequently dried. The drying step is important in order to obtain an even washcoat on the monolith walls, and preferably the monolith is being rotated around its axis during drying. However, this requires a suitable drying setup. The simplest method is to dry the monoliths in a regular furnace. The monoliths can be calcined after each drying step, or they can be dipped directly after drying. When dipping without calcination, some of the washcoat layer can be dissolved back into the slurry, such that the net uptake is less than when it is calcined between each dipping step. However, calcining after drying is time consuming and does not affect the quality of the final washcoat layer [49].

The slurry should contain particles which are of the same size as the macropores of the monolith, typically 5 μm. The slurry should not have a too high viscosity. A high viscosity might withstand the capillary forces that drag the liquid into the channels, leaving a partly washcoated monolith.

2.3 Catalyst characterization

2.3.1 N$_2$ adsorption-desorption

A tool for finding the specific surface area [m^2/g] of a catalyst or a support is the BET method, a method based on the isotherm of Brunauer, Emmett and Teller [50]. The main idea of this method is that the surface of the catalyst physisorbs an inert gas such as nitrogen or argon in defined layers. The surface area is determined from the amount of gas needed to fill a monolayer (θ) on the catalyst or support.

The BET equation, Equation (2.1), is derived from the rate equations expressing the equilibrium of the adsorption and desorption. It is assumed that the adsorption and desorption rates are equivalent.

$$\frac{P}{V_a(P_0 - P)} = \frac{1}{\chi V_0} + \frac{(\chi - 1)}{\chi V_0} \frac{P}{P_0} \tag{2.1}$$

where χ is the ratio of the desorption rate constants, k_2 and k_1 for the second and first layers, respectively.

Plotting $P/(V_a(P_0 - P))$ versus P/P_0 gives a straight line that intersects the vertical axis at $\eta = 1/(\chi V_0)$ and has the slope $\alpha = (\chi - 1)/(\chi V_0)$. Usually a relative pressure ranging from 0.05 to 0.30 is used because it gives the best fit [51, 52]. From this the volume adsorbed in the first monolayer, V_0 can be calculated by using Equation (2.2)

$$V_0 = \frac{1}{\alpha + \eta} \tag{2.2}$$

The volume adsorbed in the first monolayer is subsequently used to find the number of molecules adsorbed, N_0, given by Equation (2.3)

$$N_0 = \frac{PV_0}{k_B T} \tag{2.3}$$

At 77 K N$_2$ occupies an area of $A_0 = 0.162$ nm^2 [4]. The BET surface area per gram support or catalyst is found by multiplying N_0 by A_0.

There is a number of assumptions related to the BET method. As already mentioned, the rate of adsorption and desorption are assumed to be equal in any layer. The amount of molecules adsorbed on the first layer is equal to the number of adsorption sites and these adsorbed molecules serve as adsorption sites for the subsequent layer. Possible interactions between the adsorbates are neglected, that is, a molecule that is adsorbed will not prevent another molecule from adsorbing onto the adjacent site due to repulsive forces or steric hindrance. As for the layers above the first ($\theta > 1$), the adsorption-desorption conditions are assumed to be equal for all layers. The adsorption energy for the molecules on these layers is the same as the condensation energy. When the pressure equals the saturation pressure the multilayer will grow to infinite thickness.

The adsorption-desorption isotherms are classified according to IUPAC recommendations [52]. The types of physisorption isotherms can be seen in figure 2.3. A phenomenon which is closely related to filling and emptying of mesopores is hysteresis. The types of hysteresis are shown in figure 2.4.
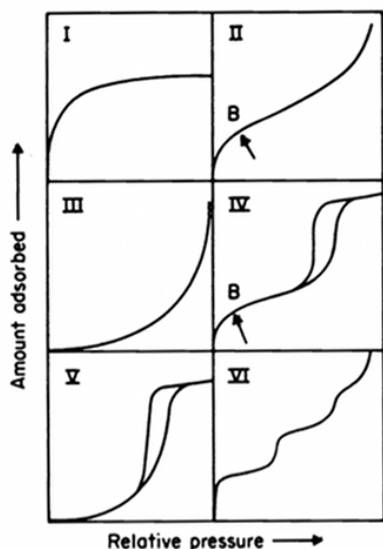
Figure 2.3: The different types of sorption isotherms [52].
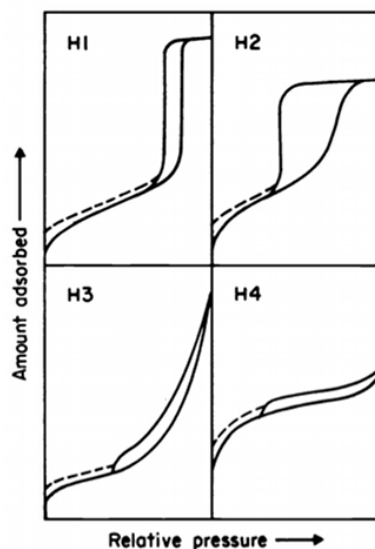
Figure 2.4: The different types of hysteresis loops [52].

The BET method is often not applicable if the isotherm is Type I or Type III. Type II and Type IV isotherms are well suited for the BET method if the BET plot is linear and contains Point B. The Type II isotherm is attained with a non-porous or macroporous compound. Typical for the Type IV isotherm, which is associated with adsorption in mesoporous structures, is the difference between the adsorption and the desorption in the multilayer range. This is explained by the hysteresis effect, a phenomenon related to pressure needed to fill and discharge the pores [4, 51]. Hysteresis is connected to capillary condensation is mesoporous structures. The lower closure point, that is the lower point where the adsorption and desorption curves meet, depends mainly on the nature of the adsorptive and not so much on the porous adsorbent [52]. The shape of the hysteresis loops are often connected to pore structure. H1 is often associated with compacts of more or less uniform spheres, and gives a rather narrow pore size distribution [52].

Hysteresis is usually not seen in the monolayer-micropore filling range. In the case of micropores, the accessibility of the pores limits the nitrogen uptake, not the total surface area. The BET method does not take the filling of micropores into account, meaning that the result may be a wrong representation of the truth [52].

The adsorption-desorption method is also applied in order to retrieve information about the pores such as the pore volume, the pore size distribution and the average pore size. Pores are classified according to their width [53]. Micropores are smaller than 2 nm, mesopores are between 2 and 50 nm, whereas macropores are larger than 50 nm. The method most frequently applied for calculation of the pore size and pore

volume of mesopores is the Barrett-Joyner-Halenda (BJH) method [54]. The method assumes cylindrical pores. The Kelvin equation takes capillary condensation into account. Although it is generally accepted that the Kelvin equation is not suitable for micropores, the validity of the Kelvin equation is not clearly defined [51, 54]. Some claim that the lower pore size limit is as low as 7.5 nm [51].

2.3.2   X-ray diffraction (XRD)

X-ray diffraction (XRD) is used for identification of the crystalline phases in catalysts and to determine the particle size. One major advantage of this technique is that it can be performed *in situ*, and therefore give a good impression of the state and composition of the catalyst. The technique is one of the most applied methods in characterization of catalysts [4].

In XRD X-ray beams are sent towards a crystalline sample. Photons are elastically scattered by atoms in the periodic lattice of the crystal. The monochromatic scattered X-rays (X-rays with a single wavelength) that are in phase will give constructive interference when they collide with a crystal plane that is faced at an angle θ to the incident beam. The strength and angles of the scattered X-ray beams are measured as a function of the angle 2θ.
The lattice spacing, d, between two planes can be derived by using the Bragg relation (2.4)

$$n\lambda = 2d\sin\theta; n = 1, 2, ... \tag{2.4}$$

where λ is the wavelength of the X-rays and θ is the angle between the X-ray beam and the normal to the lattice plane. n is the order of reflection. The lattice spacing can be used to calculate the lattice parameters/constants by the following equation:

$$a = d\sqrt{h^2 + k^2 + l^2} \tag{2.5}$$

where h, k and l are known as the Miller indices describing the orientation of the crystallographic planes. The lattice constant is the distance between the corners in a unit cell. For a cubic structure all lattice constants are equal.

The width of the diffraction peaks provide information about the dimensions of the reflecting planes, and thus the size of the particles. The relation between the peak width and the size is given by the Scherrer formula, Equation (2.6).

$$<L> = \frac{K\lambda}{\beta\cos\theta} \tag{2.6}$$

$<L>$ is the length of the particle in the direction which is perpendicular to the reflection plane, λ and θ have the same definitions as mentioned above, β is the full width at half maximum (FWHM) of the specific peak of the XRD plot and K is a constant that depends on the crystallite shape. It often takes the value 1 [4].

XRD can not detect amorphous particles or particles that are too small. This means that it is impossible to be sure that no other phases are present. Additionally, the surface is not detected by XRD either.

2.3.3   H$_2$ chemisorption

Within catalyst characterization chemisorption is widely used technique to measure the active metal area and the particle size of supported metal catalysts [55]. Chemisorption is a term used for chemical adsorption of a probe molecule, typically hydrogen. Chemisorption is a strong, more or less permanent, adsorption where the molecules or atoms form a chemical bond with the surface. Physical adsorption, physisorption, is another type of adsorption. Physisorption is characterized by weak reversible interactions between the adsorbate and adsorbent [4].
The chemisorption technique is based on assumptions such as a specific H/M stoichiometry and particle geometry, and the fact that the hydrogen must only adsorb on the active metal, which is not necessarily correct or easy to retrieve in all situations [55, 56]. Still this cheap and easy method is widely applied. The scope of the analysis is to measure the amount of H$_2$ adsorbed at different pressures at a specific temperature. The quantity adsorbed is plotted against the pressure from which a smooth adsorption isotherm should be obtained. The amount of hydrogen adsorbed is found by extrapolating the linear part of the isotherm to zero pressure.

Chemisorption is mainly used to estimate the dispersion D of a catalyst. The dispersion is *the percentage of the metal exposed* and is defined as the ratio between the number of surface atoms of the active metal and the total number of metal atoms in the sample, given in Equation (2.7).

$$D = \frac{v_{ads}M_m F}{x_m 22400} \tag{2.7}$$

where v_{ads} [cm^3/g STP] is the adsorbed gas (e.g. H$_2$, CO, O$_2$), M_m is the molecular weight of the metal, F is the stoichiometric factor and x_m is the weight loading of the metal on the catalyst support.

The dispersion can subsequently be used to estimate the metal particle size. The relation between the dispersion and particle size is given in Equation (2.8) It is assumed that the particles are spherical and uniform, with a site density of 14.6 nm^{-2} [57].

$$D = \frac{f_s M_m}{\rho A_m N_A} \frac{S}{V} \tag{2.8}$$

where f_s, taking the value 1, is the surface fraction of the active phase, A_m is the cross sectional area of one metal atom, which is 0.066 nm^2 for cobalt, N_A is Avogadro's number, equal $6.022 \cdot 10^{23}$ atoms/mol and ρ is the density of the metal [57]. S/V is the surface to volume ratio, which for spherical particles with diameter

d_m is equal to $6/d_m$.
Inserting the known numbers Equation (2.8) can be simplified to Equation (2.9)

$$d_m = \frac{99.6}{D} \text{ nm} \tag{2.9}$$

Another application of the dispersion is to find the site-time yield, STY, which is a measure of the catalyst's average activity. The definition of the STY is the number of molecules of a specified product made per active catalyst surface site and time [58], and it is calculated with Equation (2.10).

$$\text{STY} = \frac{rM_m}{x_m D} \tag{2.10}$$

where r is the apparent rate of reaction.
The STY is an alternative to the more common turn over frequency (TOF), which is defined as the number of revelations of the catalytic cycle per unit time [58]. The TOF is only valid under differential conditions.

H$_2$ spillover

The migration of hydrogen atoms from the metal to the support is termed hydrogen spillover. Ceria is receptive towards H_2 spillover during chemisorption. Normally the chemisorption on pure ceria is an activated process which takes place at about 473 K. In presence of a metal the activation temperature might be much lower, as for instance with rhodium where spillover is observed at room temperature [59]. Hydrogen spillover can be detected by comparing the calculated particle size to the one obtained by CO adsorption, X-ray diffraction or transmission electron microscopy (TEM). If hydrogen spillover has taken place, the particles size will be significantly lower than the one found with one of the other techniques [56]. However, these techniques also have their limitations and should be used thereafter.

2.3.4 Temperature programmed reduction (TPR)

Temperature programmed reduction is a characterization method that gives information about the reducibility of an oxide and provides the optimal temperature for complete reduction of the catalyst. During TPR the catalyst is reduced in a flow of diluted H_2 while the temperature is increased linearly as a function of time. The changes in the thermal conductivity of the gas stream is monitored with a thermal conductivity detector (TCD). The signal from the TCD can be plot versus the temperature profile or as a function of time. This provides a spectrum with significant peaks which indicate the maximum rate of reduction. The general reduction reaction is as follows

$$\text{M}_x\text{O}_y(\text{s}) + \text{H}_2(\text{g}) \rightarrow \text{M}(\text{s}) + \text{H}_2\text{O}(\text{g})$$
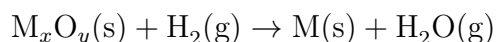
Analyzing TPR results is more about comparing and finding qualitative conformity and/or differences than obtaining quantitative information. Keeping experimental conditions such as the amount of reducible species, the concentration and flow rate of the H_2 and the heating rate constant is critical [60]. The height of the TPR peak depends on experimental conditions such as the mass of the sample and the H_2 flow rate. The location of the peak depends on the material, and is therefore an intrinsic property of the compound that is reduced [61]. Four main features determine the TPR results; the thermodynamics and kinetics related to the reduction of the compound in question, textural changes such as sintering occurring at higher temperatures, and diffusional phenomena within the lattice structure of the compound [61].

2.4   Gas chromatography (GC)

Gas chromatography is a widely applied technique for the identification and quantitative analysis of the product composition of a reaction. The idea is to separate the compounds by temperature-programmed vaporization and pass the separated compounds through detectors. The theory below is taken from [62].

A gas chromatograph consists of an injection port, a column and one or more detectors. A fraction of the product stream is injected into a column which is situated in an oven. After the injection a temperature program governs the temperature in the column, separating the compounds according to their volatility at that specific temperatures. A carrier gas, usually inert such as He, Ar or N_2, transports the compounds through the column and past the detector. The column contains a stationary phase, either solid or liquid, which delays the passage of the components. There are two main types of columns: packed and capillary columns. The components leave the column according to their volatility. The most volatile compounds leave first.
There exists a number of different types of detectors, of which the thermal conductivity detector (TCD) and flame ionization detector (FID) are most common. The FID is sensitive to most organic compounds. The column effluent is passed through a flame of burning hydrogen and air. A small amount of the carbon atoms in the effluent undergo ionization, and the ions are detected by an electrode. The electric current is amplified and gives the chromatographic signal. The TCD measures the the difference in thermal conductivity between the column effluent and the carrier gas, and can therefore detect any compound that has a different thermal conductivity than the carrier gas. The GC analysis provides a chromatogram with peak, where the position of the peak identifies the species and the area of the peak indicates the relative amount of the species.
The gas chromatograph is calibrated with one or more gas mixtures of known constituents and known mole fractions of these. As a result of the calibration each component is labeled with a certain retention time which is the amount of time spent in the column, and gives the position of the peak of the chromatogram. The calibration also provides the response factors for the different components which is the ratio between the amount and the area.

Chapter 3

Experimental procedure

3.1 Catalyst synthesis

The exact amounts and concentrations used in the synthesis of the powder and monolith catalysts are listed in Appendix A.1.

3.1.1 Synthesis of $CeO_2-Al_2O_3$

$20\,wt\%$ $CeO_2-Al_2O_3$ nanocomposites were prepared by an evaporation-drying method [8]. The loading corresponds to the amount of ceria. Cerium nitrate hexahydrate $(Ce(NO_3)_2 \cdot 6\,H_2O)$ was employed as the cerium precursor, whereas the alumina used was a Sasol Puralox SCCa (Puralox).

A specific amount of $Ce(NO_3)_2 \cdot 6\,H_2O$, citric acid (CA) and polyethylene glycol (PEG) (0,1 g/mL) were dissolved in distilled water. The mixture was stirred at room temperature for two hours. Then the alumina powder was added stepwisely under continuous stirring. After the suspension had been stirred for approximately 18 hours at room temperature it was evaporated at 358 K for two days until all the water was evaporated and the solid was left. The solid was subsequently dried at 373 K over night. From the dried solid material five different nanocomposites were made by calcining in air at temperatures ranging from 1173 to 1473 K for 5 hours with a heating rate of 3 K/min.

3.1.2 Synthesis of powdered $Co/CeO_2-Al_2O_3$

The synthesis of the impregnated cobalt catalysts is described in detail elsewhere [63]. The solution used during the incipient wetness impregnation was a mixture of 50 vol.% ethylene glycol and water. The catalysts were calcined at 873 K for 5 hours with a heating rate of 3 K/min.

For the activity testing the catalyst was pelletized and subsequently crushed in order to obtain a desired particle size of 75-150 μm. The catalyst was diluted with α-alumina with a particle size of 150 to 250 μm.

The powdered catalysts are denoted by $Co/CeO_2-Al_2O_3$ ([$T_{calc.}$] K). In some cases, $CeO_2-Al_2O_3$ is abbreviated by C-A.

3.1.3   Syntesis of monolithic Co catalyst

Cylindrical pieces (h = 10 mm, d = 15 mm) of square channeled cordierite, $2\,MgO{\cdot}2\,Al_2O_3{\cdot}5\,SiO_2$ (Corning), were used as support. The cell density is 62.2 cells/cm^2, which equals 400 cpsi (cells per square inch). The properties of the monolith are given in Appendix A.2. The monolith cylinders had a 3 mm hole through the center for the internal thermocouple quartz tube.

A 15 wt.% slurry of Disperal P2 (Sasol) and distilled water was made. The monoliths were dipped in the slurry and the excess water was gently blown off with pressurized air until all the channels were free of slurry. The monoliths were dried at 383-393 K for at least 4 hours. The dipping and drying procedure was repeated until the total weight gain was about 17 wt.%. The washcoated monoliths were calcined at 773 K for 4.5 h with a heating ramp of 5 K/min. After calcination the washcoat layer was approximately 15 wt.%.

The ceria was applied with a similar method as the evaporation-drying method used to prepare the $CeO_2-Al_2O_3$ nanocomposites for the powder catalysts. Specific amounts of $Ce(NO_3)_2{\cdot}6\,H_2O$, CA and PEG (0,1 g/mL) were dissolved in distilled water. The mixture was stirred at room temperature for two hours. The washcoated monolith was put into the solution and left for 5 h. The monolith was dried and calcined at 773 K for 4.5 h with a heating ramp of 5 K/min.

The cobalt was added to the monolith surface by wet impregnation of a solution of $Co(NO_3)_2{\cdot}6\,H_2O$ dissolved in distilled water. The required concentration of cobalt ions in the solution in order to obtain a cobalt loading of 5 wt.% was determined by dipping the washcoated monolith in distilled water prior to the impregnation step. The excess liquid was carefully blown off with pressurized air, and the wet monolith was weighed. The weight difference was used to calculate the water absorption capacity of the monolith. Based on this, a solution of $Co(NO_3)_2{\cdot}6\,H_2O$ and distilled water was prepared to ensure a cobalt loading of 5 wt.%.
After impregnation the monolith was dried at 373 K for 4 hours, and subsequently calcined in air at 873 K for 5 hours with a heating rate of 3 K/min.

3.2   N$_2$ adsorption-desorption

A Micromeritics TriStar 3000 instrument was used to measure the nitrogen adsorption-desorption isotherms of the $CeO_2-Al_2O_3$ nanocomposites and the supported cata-

lysts in order to determine the specific surface area, the pore volume, the average pore size and the pore distribution of the samples.

First the samples were outgassed at 473 K overnight. The samples were weighed before and after the pretreatment. The weight obtained after the pretreatment was used for calculating the specific surface area. The samples were analyzed at 77 K (liquid nitrogen temperature). The specific surface area was determined by the BET method in the 0-0.2 partial pressure range. The pore size distribution is based on the Barrett-Joyner-Halenda (BJH) method by making use of the desorption branch of the isotherm.

3.3 X-ray diffraction (XRD)

X-ray diffraction (XRD) of the $CeO_2-Al_2O_3$ samples was done with a Bruker AXS D8 focus powder diffractometer using $CuK\alpha$ radiation with $\lambda = 1,54 \times 10^{-10}$ m.

The diffraction patterns were measured in the 2θ range from 20° to 85° with a step size of 0.02°/step. The time per step applied was 0.75 s/step. The results were analyzed with the software DIFFRACplus EVA v2.1 (2011) and TOPAS v4.2 (Bruker AXS).

XRD had been done with $Co/CeO_2-Al_2O_3$ before with a Siemens D5005 X-ray diffractometer [63]. The diffraction patterns were measured in the 2θ range from 5° to 80° with a step size of 0.02°/step. The time per step applied was 10 s/step on most of the samples. Otherwise it was 7 s/step.

The Scherrer thickness was calculated in EVA by applying the FWHM with Equation (2.6) for the peak located at $2\theta = 36.8$ °and $2\theta = 28.5$ °for Co_3O_4 and CeO_2, respectively. The shape factor K was set to 0.89 for Co_3O_4 [64]. For CeO_2 it was set to 1. The instrumental line broadening was determined from the XRD analysis of LaB_6 [65]. The lattice parameters of CeO_2 were found by Rietveld refinement in TOPAS based Equation (2.5).

3.4 H$_2$ chemisorption

The dispersion and particle size of the active metal were determined with hydrogen chemisorption using a Micromeritics ASAP 2010 apparatus. The temperature was controlled with a thermocouple placed between the reactor and the inner wall of the furnace. It is assumed that hydrogen adsorbs dissociatively, that is, one hydrogen atom per metal surface area atom [66].

A sample (~200 mg) was weighed before put into a U-shaped quartz reactor which was already loaded with some loosely packed quartz wool. To encapsulate the sample, quartz wool was also put on top of the sample. The reactor was attached to the apparatus. To ensure that the reactor was completely closed to the atmosphere, vacuum was introduced and a leak test was performed.

Prior to the analysis the sample was reduced in flowing H_2 at 923 K for 5 h with a heating rate of 2 K/min. After the reduction the sample was evacuated for 30 min at 603 K and subsequently cooled to 313 K. The adsorption isotherm was measured between 10 and 510 torr at 313 K.

3.5 Temperature programmed reduction (TPR)

Temperature programmed reduction (TPR) was carried in out in order to investigate the reducibility of the supports and catalysts. A sample (~200 mg) was inserted into a U-shaped quartz reactor. The reactor was heated to 1203 K with a heating rate of 10 K/min while 7% H_2 in Ar flowed through. Once reached 1203 K, the temperature was kept constant for 30 min while the gas kept flowing through. A thermal conductivity detector (TCD) recorded the flow of hydrogen. The TCD signal was analyzed by a Shimadzu GC-8A gas chromatography apparatus.

3.6 Activity testing

3.6.1 Set-up

The catalytic partial oxidation of methane was conducted in a cylindrical quartz reactor at atmospheric pressure. The flow scheme is shown in Figure 3.1 and the reactors are shown in Figure 3.2.

Prior to start-up of the activity testing a leak test of the whole system was performed. The flow of the gases were controlled with mass flow controllers (MFC) which were calibrated with a bubble film flow meter. The calibration curves can be found in Appendix D.1.

The products were analyzed with a GC. The GC, an Agilent 6890N, was calibrated with a gas mixture with known constituents. The calibration table is found in Appendix D.2. The calibration with respect to O_2 was done with air, and the calibration with respect to N_2 was done by taking the mean value of the N_2 response factor of the gas mixture and air. The GC consisted of a flame ionization detector (FID) and a thermal conductivity detector (TCD). The specifications of the detectors are listed in Table 3.1. Nitrogen was used as internal standard.

Table 3.1: Specifications of the FID and TCD

Detector	Column	Carrier gas	Compounds
FID	Capillary HP-PLOT	He	CH_4, C2-C5
TCD	Packed carbosieve, 10 ft.	He	H_2, O_2, N_2, CO, CO_2, CH_4

A movable K-type thermocouple (0.5 mm) was placed in a quartz tube in the middle of the reactor such that the axial temperature profile of the gas could be measured. The effect of the thin quartz wall on the registered temperature was neglected. The furnace temperature was measured with a K-type thermocouple placed between the inner wall of the furnace and the outer wall of the quartz reactor on the same axial level as the outlet (lower part) of the catalyst bed/monolith.
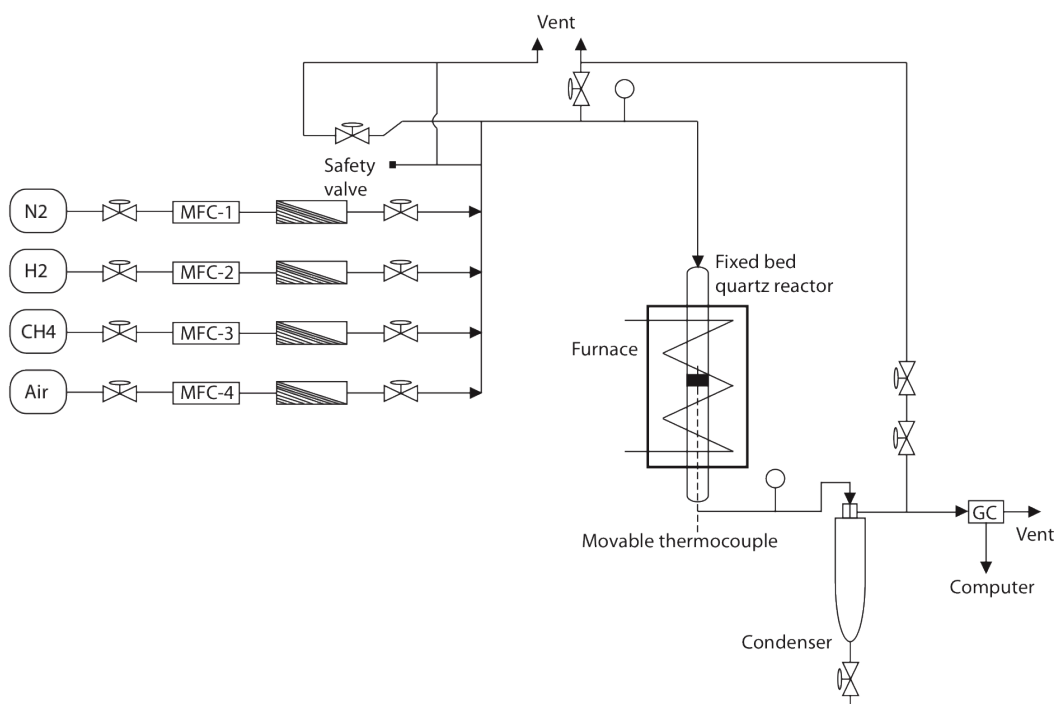
Figure 3.1: A schematic overview of the setup used for catalytic partial oxidation of methane.
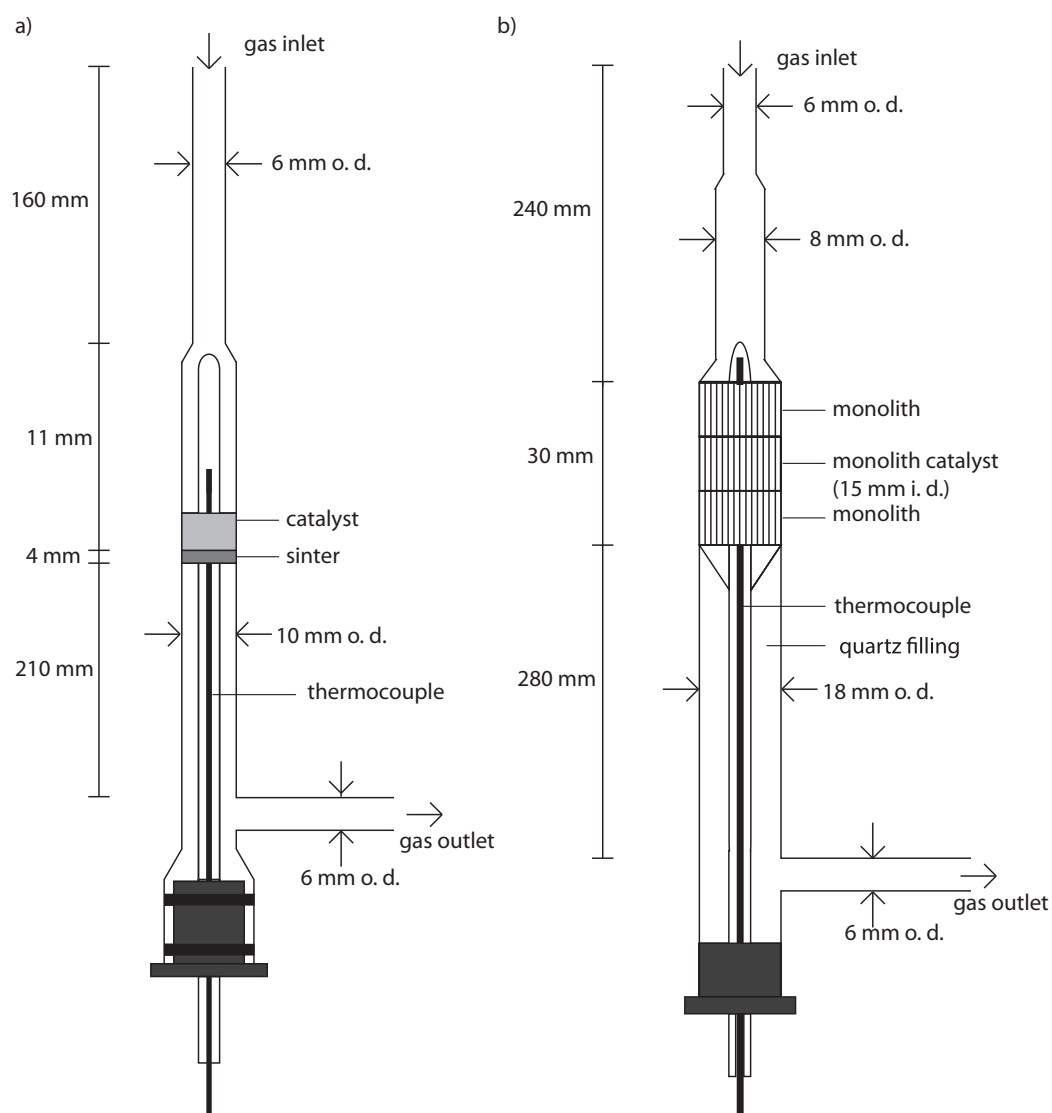
Figure 3.2: An illustration of the reactor used for the activity testing of a) the powder catalysts and b) the monolithic catalysts.

3.6.2   Reaction

The catalyst was pelletized and sieved in order to obtain a particle size of 75-150 μm. 10-100 mg catalyst was diluted with $\sim$150 mg α-alumina (150-250 μm). The mixture was loaded inside the reactor with a layer of $\sim$150 mg α-alumina between the sinter and the catalyst bed.

The catalyst was reduced in situ with 50 mL/min (STP) 50 vol% H_2 in N_2 at 973 K for 2 h with a heating rate of 10 K/min.
The reaction was run at atmospheric pressure. The composition of the CH_4:O_2:N_2 reactant mixture was 2:1:3.72. The furnace temperature was between 623 K and 1123 K and the gas hourly space velocity (GHSV) was 75 L_{CH_4}/g_{cat}h, unless otherwise stated. Methane and air were fed separately and mixed before entering the top of the reactor. The mixture moved downwards through the catalyst bed/monolith and the products and unreacted reactants were withdrawn at the bottom of the reactor. The mixture was sent to a GC for product analysis via a condenser for water removal.

The conditions for each experiment are shown in Appendix D.3.

Chapter 4

Results and discussion

4.1 Catalyst characterization

4.1.1 N$_2$ adsorption-desorption

N$_2$ adsorption-desorption analysis was done for the CeO$_2$−Al$_2$O$_3$ nanocomposites and for Puralox calcined at the same temperatures as the CeO$_2$−Al$_2$O$_3$. The detailed results, isotherms and pore size distribution plots are found in Appendix C.1.

BET surface area and pore volume

The N$_2$ adsorption-desorption gave information about the specific BET surface area of the samples. The specific surface area is calculated based on the 0-0.2 partial pressure range with Equation (2.2) from the plot of Equation (2.1) on page 11. An example of the calculation is given in Appendix B.2. The pore volume is determined by the BJH method by applying the desorption data.

The BET surface area for the CeO$_2$−Al$_2$O$_3$ nanocomposites calcined at temperatures ranging from 1173 K to 1473 K are plotted in Figure 4.1. For comparison purposes the γ-alumina (Puralox) was subjected to the same heat treatment as CeO$_2$−Al$_2$O$_3$. Figure 4.1 shows the anticipated trend of a decreasing surface area with increasing calcination temperature for both of the tested compounds. This is due to sintering of the particles. When exposed to high temperatures γ-alumina will undergo phase transformation via other metastable phases to α-alumina, which is illustrated in Figure 2.1. The Puralox starts out with a higher surface area than the nanocomposite. This might be due to the fact that the presence of ceria blocks some of the pores in the alumina structure and lowers the surface area. The surface area of the Puralox is higher than that of the nanocomposites at 1173 K and 1273 K. With reference to Figure 2.1 on page 7 the alumina is assumed to be in the metastable δ- and θ-phases. At higher temperatures, such as 1373-1473 K, the

alumina transforms into α-alumina which is characterized by a low surface area and small pore volume.
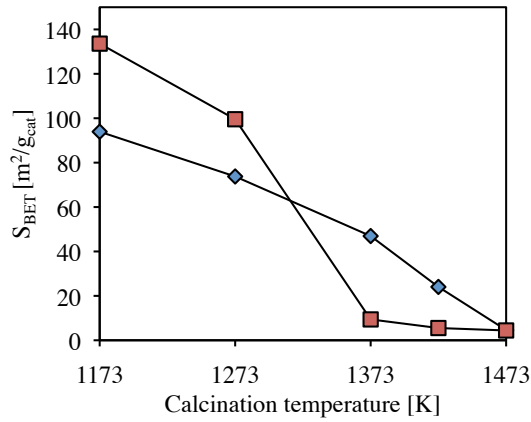
Figure 4.1: The evolution of the BET surface area of ◆ $CeO_2-Al_2O_3$ and ■ pure Puralox as a function of the calcination temperature

The decreasing surface area trend of $CeO_2-Al_2O_3$ is quite linear, whereas the one for the Puralox has a large drop between 1273 K and 1373 K. This is presumably due to the earlier mentioned phase transformation. Earlier studies have shown that the ceria delays this phase transformation which is indicated by the plot representing the $CeO_2-Al_2O_3$ [8].
Figure 4.2 shows a similar trend concerning the pore volume of the samples. A collapse of the pores is indicated by the sudden drop in the pore volume between the samples calcined at 1373 K and 1423 K. Again, the protective function of the ceria is visible.
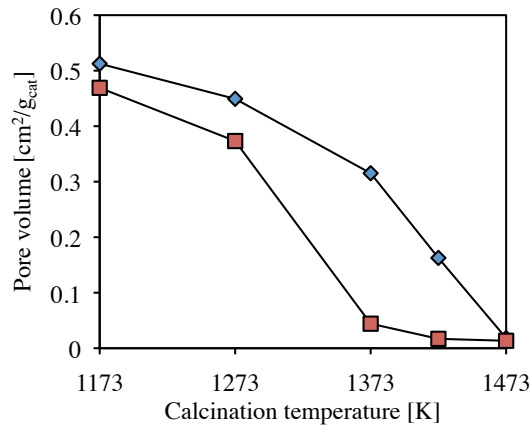
Figure 4.2: The evolution of the BJH cumulative desorption pore volume of ◆ $CeO_2-Al_2O_3$ and ■ pure Puralox as a function of the calcination temperature

In Appendix C.1 the BET surface area of all samples prepared during this work and an earlier study are presented [63]. The results show variations in the surface

area between samples that are prepared with the exact same procedure. The BET surface area estimations are therefore only used to indicate the effect of increasing the calcination temperature of the support and the difference between the nanocomposites and pure Puralox at different calcination temperatures, as shown in Figure 4.1.

The reason for the variation in the estimated BET surface area could be small deviations in the synthesis procedure such as the rate at which the alumina is added to the complex solution, the stirring speed or the evaporation step. It could also be that the variations in the amount of $CeO_2-Al_2O_3$ calcined at the different temperatures influences the surface area. The Puralox was obtained from different sources, but was still the same type from the same producer and was given the same pretreatment, so this should not influence the final result. N_2 adsorption-desorption measurement was done twice on the same sample, giving nearly identical results (see Appendix C.1). This indicates that the apparatus is not causing the differences.

4.1.2   X-ray diffraction (XRD)

The diffraction patterns for $CeO_2-Al_2O_3$ and $Co/CeO_2-Al_2O_3$ are shown in Figure 4.3 and Figure 4.4, respectively. The peaks were identified with the PDF-4+ database. In Figure 4.4 the different species are indicated.
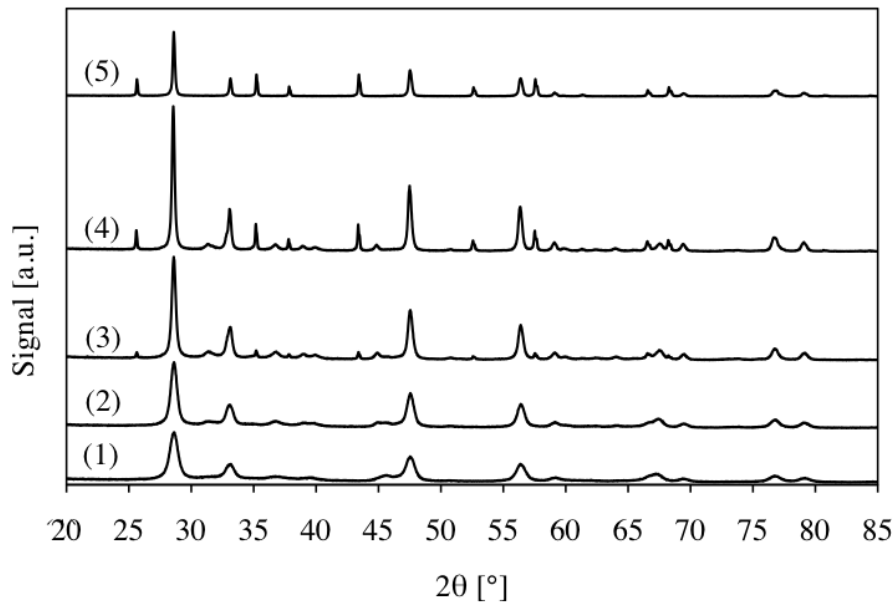
Figure 4.3: The XRD patterns for the $CeO_2-Al_2O_3$ nanocomposites calcined at (1) 1173 K, (2) 1273 K, (3) 1373 K, (4) 1423 K and (5) 1473 K.
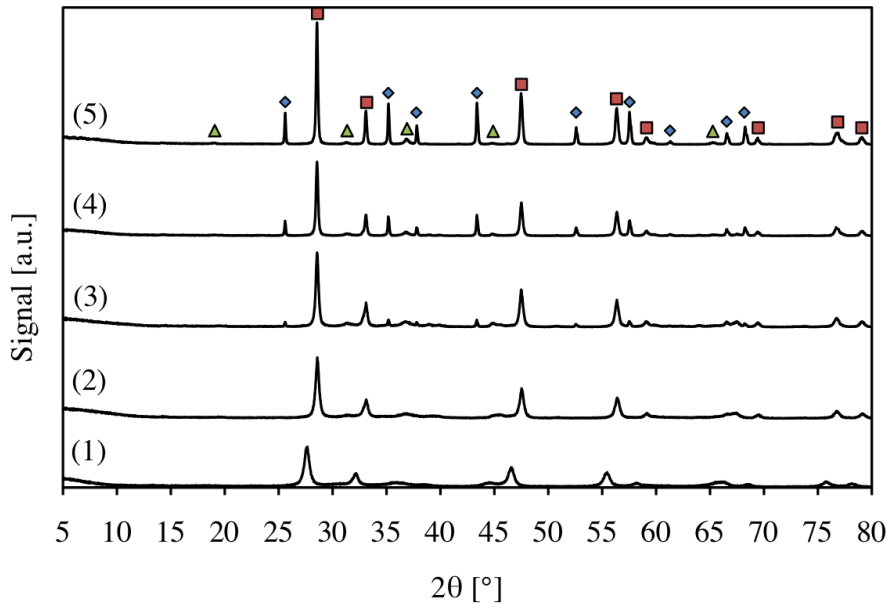
Figure 4.4: The XRD patterns for Co/CeO$_2$−Al$_2$O$_3$ (1) (1173 K), (2) (1273 K), (3) (1373 K), (4) (1423 K) and (5) (1473 K). ◆ Al$_2$O$_3$, ■ CeO$_2$ and ▲ Co$_3$O$_4$ [63].

From Figure 4.3 and 4.4 the increased crystallinity observed by means of less noise and more defined peaks as the calcination temperatures increase. In case of the diffractogram of Co/CeO$_2$−Al$_2$O$_3$ (1173 K) it was a challenge to locate the peaks ascribed to the cobalt oxide. The difficulty of finding Co$_3$O$_4$ by XRD might be ascribed to a well dispersed cobalt phase, amorphous cobalt or the existence of a cobalt ceria solid solution [67, 68]. Differentiating the different phases of Al$_2$O$_3$ is so to speak impossible due to overlapping and similar diffraction patterns. However, the development of the α-Al$_2$O$_3$ phase is easy to detect due to the peak that springs up at around 25° in diffractogram (3) to (5).

Crystallite size

The crystallite sizes of Co$_3$O$_4$ and CeO$_2$ were estimated by EVA. In EVA, the crystallite size is calculated from one of the peaks by applying the Scherrer formula (Equation (2.6)) using the FWHM of a selected peak.

As previously mentioned, the diffraction peaks of Co$_3$O$_4$ are undistinguishable from cobalt aluminate, CoAl$_2$O$_4$ [63]. It is assumed that the peaks can be ascribed to the cobalt oxide, and are therefore used in the estimation of the crystallite size. The reported crystallite sizes of Co$_3$O$_4$ are calculated by using the peak at a 2θ position around 28.6°.

Table 4.1: Crystallite sizes of Co_3O_4 calculated by applying the FWHM.

Catalyst	$d_{Co_3O_4}$ [nm]
Co/C-A (1173 K)	6.6
Co/C-A (1273 K)	7.2
Co/C-A (1373 K)	12.8
Co/C-A (1423 K)	20.0
Co/C-A (1473 K)	22.9

The trend of the estimated sizes of Co_3O_4 correspond tolerably well to the Co^0 particle sizes found with H_2 chemisorption, which are presented in Section 4.1.3. It must be emphasized that the estimated crystallite sizes presented in Table 4.1 should be interpreted critically. In the first place, the peaks in the XRD patterns, and perhaps especially for cobalt, are not all free-standing. This is related to the width of the peak and neighboring peaks. Secondly, the more noise present in the diffractogram, the less defined the peak will appear, especially for peaks with low intensity. The position, the height and the width of the diffractograms are all influenced by the sample preparation. Small particles and poor crystallinity can hinder phases from being detected by XRD.

The evolution of the crystallite size of CeO_2 as a function of calcination temperature is shown in Figure 4.5.
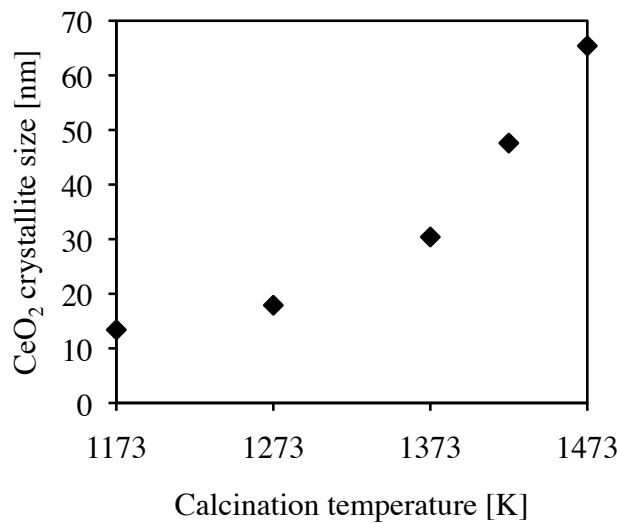
Figure 4.5: The size of the CeO_2 crystallites as a function of the calcination temperature of the $CeO_2-Al_2O_3$ nanocomposites

The crystal size of CeO_2 increases as the heat treatment becomes more severe, which was also found by Boullosa et al. [28]. This is due to sintering.

It is also common to estimate the crystallite sizes with the software TOPAS. In TOPAS the whole diffraction pattern is fitted iteratively by Rietveld refinement which is used to calculate the FWHF, as opposed to EVA where the crystallite sizes are determined directly from the diffraction pattern. The calculated crystallite sizes for CeO_2 and Co_3O_4 appear to vary with the calculation method (see Appendix C.2). Poor crystallinity of the samples and low quality of the diffraction patterns can make the fitting in TOPAS inaccurate, which again influences the results.

Lattice parameters

The lattice parameters were found by fitting the peak position by iteration in TOPAS for CeO_2 for the $CeO_2-Al_2O_3$ nanocomposites and the $Co/CeO_2-Al_2O_3$ catalysts. The results are listed in Table 4.2.

Table 4.2: Lattice parameters of CeO_2

Calc. T	Lattice parameter [Å]	
	$CeO_2-Al_2O_3$	$Co/CeO_2-Al_2O_3$
1173 K	5.446	5.504
1273 K	5.444	5.412
1373 K	5.414	5.415
1423 K	5.415	5.415
1474 K	5.417	5.414

It has been suggested that the lattice parameter for CeO_2 might be lower for the samples with cobalt than for the samples without because Ce^{4+} is substituted by the smaller Co^{2+} [69]. The numbers shown in Table 4.2 do not confirm this theory. The lattice parameters for the samples calcined at 1373 K, 1423 K and 1473 K do not seem to change at all when cobalt is added, while the lattice parameters for the ones calcined at 1173 K and 1273 K increase and decrease, respectively. More samples have to be analyzed in order to state whether these results are coincidental or if there is a scientific explanation.

Another expected trend would be that the lattice parameter of CeO_2 increases with decreasing crystallite size [70]. It has been suggested that the lattice parameter increases as the particle size of CeO_2 decreases because of the changing density of the oxygen vacancies in the lattice and the transition from Co^{4+} to Co^{3+}, inducing strain in the lattice [70]. The oxygen vacancies occur in order to preserve the electron neutrality [71]. Again, the results presented in Table 4.2 do not fully agree. When comparing the numbers in Table 4.2 with the CeO_2 sizes found in Figure 4.5 it is obvious that the evolution of the crystalline size and the lattice parameter do not follow each other systematically. There is a clear change in the lattice parameters at the transition between 1273 K and 1373 K for $CeO_2-Al_2O_3$ and between 1173 K and 1273 K for $Co/CeO_2-Al_2O_3$. Apart from that, the lattice parameters appear to be quite constant.

So, in this case there might exist a mechanism increasing the lattice parameter, i.e. smaller particles, and a mechanism decreasing the lattice parameter, i.e. substitution of cerium ions by cobalt ions. The lack of an unambiguous trend was also observed by Lovón et al. [68] .

4.1.3   H$_2$ chemisorption

H$_2$ chemisorption was done on the impregnated and calcined catalysts. The dispersion of the metal on the support was calculated by applying Equation (2.7). The dispersion was subsequently used to estimate the metal particle size by Equation (2.8). The results are listed in Table 4.3. The adsorption plots and detailed data are found in Appendix C.3.

Table 4.3: The dispersion and metal particle size of the Co/CeO$_2$−Al$_2$O$_3$ catalysts estimated from H$_2$ chemisorption measurements.

Catalyst	D [%]	d [nm]
Co/C-A (1173 K)	8.1	12.4
Co/C-A (1273 K)	8.9	11.2
Co/C-A (1373 K)	8.9	11.2
Co/C-A (1423 K)	4.7	21.2
Co/C-A (1473 K)	3.5	28.3

The particle size estimations given in Table 4.3 for Co/CeO$_2$−Al$_2$O$_3$ (1173 K) - (1373 K) indicate that the use of ethylene glycol as solvent in incipient wetness impregnation gives quite uniform metal particles, even though the nature of the support varies, as was suggested by Borg et al.[45]. It is also suggested that the ceria enhances the dispersion of the metal [67]. The qualitative effect of the ceria could be investigated further by comparing the effect of different ceria loadings. The relatively low dispersion of cobalt on Co/CeO$_2$−Al$_2$O$_3$ (1423 K) and (1473 K) can be seen in connection to the low specific surface area of these catalysts.

A previous study with exactly the same catalysts indicated that reducing the catalyst at 623 K for 10h was not sufficient [63]. Little hydrogen was adsorbed onto the catalyst, indicating that the catalyst had not been reduced. The reduction conditions applied are widely used when doing H$_2$ chemisorption studies on cobalt catalysts. It was suggested that the results were due to H$_2$ spillover to the ceria. Hydrogen spillover is the migration of hydrogen atoms from the metal onto the support. However, the total volume H$_2$ adsorbed was too low to explain the results with H$_2$ spillover.

When increasing the reduction temperature to 923 K, the results improved remarkably, and reasonable dispersions were obtained. The necessity of such a high reduction temperature could be due to a strong interaction between the cobalt and the ceria, or that the cobalt is embedded in the ceria structure. Normally the

chemisorption on pure ceria is an activated process which takes place at about 473 K. In presence of a metal the activation temperature might be much lower, as for instance with rhodium where spillover is observed at room temperature [59]. It has been reported that catalysts containing ceria are subject to hydrogen spillover during H_2 chemisorption [8, 9, 55, 59]. The adsorption plots (see Appendix C.3) show an increased hydrogen consumption at higher pressures, whereas a "normal" plot would flatten out at higher pressures. This might be an indication of hydrogen spillover onto the ceria. The adsorption data will thus probably include the total adsorption of H_2 on both the active metal and CeO_2. A way to circumvent the spillover effect is to decrease the analysis temperature and use low pressures within a narrow range, which has been done for noble metal catalyst [8, 56, 72, 73]. Optimizing the H_2 chemisorption conditions has not been a scope of this work.

4.1.4   Temperature-programmed reduction (TPR)

Temperature-programmed reduction was done with the supported Co catalysts and the $CeO_2-Al_2O_3$ nanocomposites. The plots of the temperatures and signals as functions of time are shown in Figure 4.6 and 4.7 for $CeO_2-Al_2O_3$ and $Co/CeO_2-Al_2O_3$, respectively.
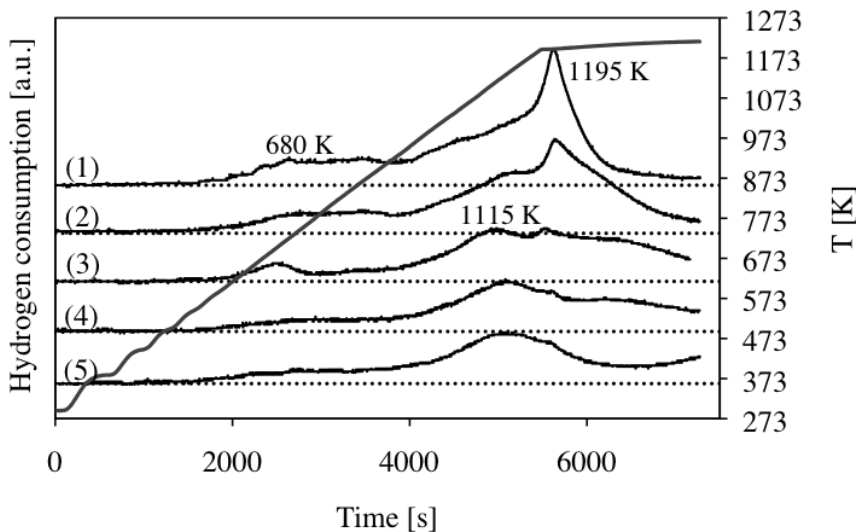
Figure 4.6: Plots of the TPR profiles of $CeO_2-Al_2O_3$ calcined at (1) 1173 K, (2) 1273 K, (3) 1373 K, (4) 1423 K and (5) 1473 K and the temperature profile as a function of time. TPR was done in 7% H_2 in Ar with a heating rate of 10 K/min from ambient to 1203 K. The dotted lines show the baseline.
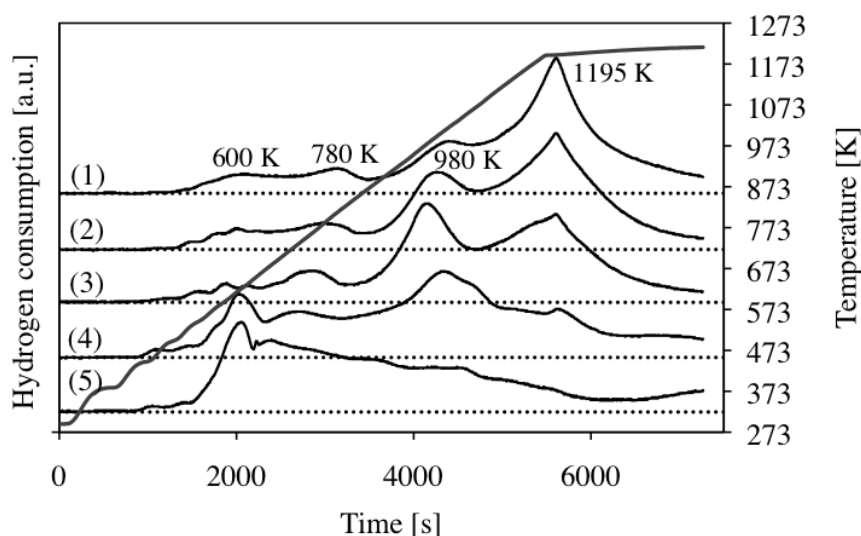
Figure 4.7: Plots of the TPR profiles of $Co/CeO_2-Al_2O_3$ (1) (1173 K), (2) (1273 K), (3) (1373 K), (4) (1423 K) and (5) (1473 K) and the temperature profile as a function of time. TPR was done in 7% H_2 in Ar with a heating rate of 10 K/min from ambient to 1203 K. The dotted lines show the baseline.

Comparing the TPR plots with literature should be done with caution due to the factors that influence the results. The position and shape of the TPR pattern depends on the catalyst preparation method, the species it consists of, the crystallinity of its constituents and the dispersion [33, 74, 75, 76]. The reduction properties of a supported metal oxide could be influenced by the nature of its support. The metal support interaction might promote or inhibit reduction at a certain temperature [77]. The results are also influenced by experimental conditions such as the H_2 flow rate, the heating rate and the amount of sample.

Reduction of $CeO_2-Al_2O_3$

It is generally believed that the reduction of CeO_2 occurs at in two stages. The reduction of surface oxygen species takes place at around 800 K, whereas the reduction of bulk oxygen happens around 1100 K [33, 78, 79, 80, 81]. The results from the TPR analysis of $CeO_2-Al_2O_3$ (Figure 4.6) show that the reduction of CeO_2 starts at around 600 K and continues beyond the final temperature of 1195 K. It is assumed that the broad area between 600 and 950 K is attributed to the reduction of surface oxygen and that the peak at 1115 K is related to the reduction of bulk oxygen.

The reduction patterns for $CeO_2-Al_2O_3$ calcined at 1423 K and 1473 K are quite similar. The high calcination temperature has led to a collapse of the porous Al_2O_3 structure and larger CeO_2 particles, which was detected by N_2 adsorption-desorption measurements and XRD analysis, respectively. This might have led to a decreased

amount of CeO_2 available for reduction. The energy required to reduce ceria increases with the particle size, which can explain the somewhat delayed reduction of the samples containing larger CeO_2 particles [82]. However, the TPR patterns in Figure 4.6 also show that the samples containing small particles have a reduction peak at 1195 K, which is absent for the samples with small crystallite sizes. The intensity of this peak seems to decrease with increasing CeO_2 particle size. Oxygen diffusion within the ceria might affect the shape of the TPR profiles [61]. When doing TPR on CeO_2 the consumption of H_2 can be due to hydrogen storage and the reduction of carbonate- and nitrate species [83].

Reduction of $Co/CeO_2-Al_2O_3$

The reduction of Co_3O_4 is widely documented and discussed. Even though Arnoldy and Moulijn reported that Co_3O_4 was reduced in one single step [76], the most common understanding is that Co_3O_4 is reduced in two stages; from Co_3O_4 to CoO and subsequently to Co [33, 46, 78, 84, 85]. Figure 4.8 shows the TPR plot of 20 wt.% Co/Al_2O_3 which was done for comparison reasons.

The first peak can be ascribed to the removal of remaining nitrates from the synthesis procedure. The sharp peak at 650 K is the reduction from Co_3O_4 (Co^{3+}) to CoO (Co^{2+}). The second reduction step (Co^{2+} to Co^0) is at 900 K. The temperature at which cobalt is reduced is strongly dependent on the oxidation state of cobalt and on the neighboring metal cations and/or oxide phases [79]. The presence of neighboring Al^{3+} increases the reduction temperature for Co^{2+}. The peak at around 1000 K could be ascribed to the reduction of cobalt aluminate. However, cobalt aluminate is expected to be reduced at temperatures above 1100 K [76, 86].
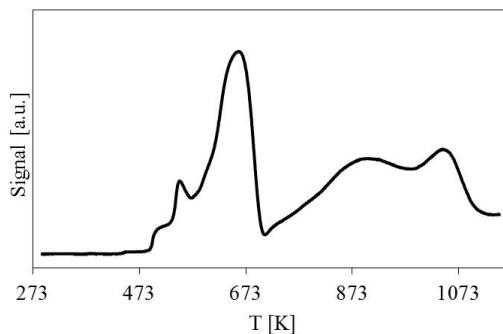
Figure 4.8: The TPR plot for 20 wt.% Co/Al_2O_3. TPR was done in 7% H_2 in Ar with a heating rate of 10 K/min from ambient to 1150 K.

Figure 4.7 shows the TPR plot of $Co/CeO_2-Al_2O_3$. The TRP pattern is complex and the mutual effect of the ceria and cobalt makes it difficult to interpret. One interpretation can be that the two first peaks at 600 K and 780 K are related to the reduction of cobalt, whereas the two last peaks at 980 K and 1195 K are related to the reduction of ceria. The reduction of cobalt ions is expected to take place over a wide range of temperatures because of the many factors that affect the peak position [76]. Furthermore it can be assumed that as the size of the cobalt and/or ceria crystallites increases, the peak temperature for the reduction of CoO shifts towards lower temperatures. It has been suggested that the ceria weakens the cobalt-oxygen bonds in the cobalt oxides and facilitates the removal of oxygen from the crystal lattice of the cobalt oxides [87]. This can explain the temperature

shift. The peaks at around 980 K could be attributed to the reduction of ceria, corresponding to the peak located at 1115 K in Figure 4.6. This peak has shifted towards lower temperatures in the presence of cobalt and has become more intense. A possible explanation could be that the presence of cobalt leads to an increased amount of reduced ceria and that the reduction takes place at lower temperatures. This is also supported by Liotta et al. who found that the peak related to the reduction of bulk ceria shifted towards lower temperatures with 5 wt.% Co on CeO_2 with respect to pure CeO_2 [84]. The metallic cobalt created during the reduction of Co_3O_4 might facilitate the reduction of CeO_2. This can induce reduction of ceria even at temperatures below 800 K [87]. The reduction of cobalt oxide requires an excess amount of hydrogen, which again enhances the reduction of ceria due to the spillover effect [33].

The TPR plots of $Co/CeO_2-Al_2O_3$ (1423 K) and (1473 K) in Figure 4.7 show a distinct peak at 600 K. The corresponding peaks for the other catalysts are much smaller. With H_2 chemisorption it was found that the dispersion for these two catalysts was significantly lower than for the three other catalysts. This means that a smaller amount of cobalt is in direct or close contact with the support, and could therefore be reduced more easily. Large particles of Co_3O_4 are expected to reduce in one step, whereas small particles are reduced in two steps due to their strong interaction with ceria [33]. The presence of a clear and sharp peak at 600 K for $Co/CeO_2-Al_2O_3$ (1423 K) and (1473 K) supports this. It seems that most of the cobalt oxide is reduced at 600 K for these two catalysts. The reducibility of cobalt on ceria is somewhat enhanced compared to the reducibility of Co_3O_4 on alumina [79].

The peak found at 780 K seems to shift towards lower temperatures as the calcination temperature of $CeO_2-Al_2O_3$ increases. The degree of reduction of a metal is closely related to the interaction between the metal and the support[88]. The fact that ceria enhances the dispersion of metal particles, might imply a lowered reducibility of these metal particles due to strong interactions between the metal and the support. There is therefore reason to believe that the reduction of cobalt oxide requires higher temperatures as the cobalt particle size decreases. The peak that shifts from 670 K to 780 K could be associated with the reduction of CoO to Co^0. It is suggested that ceria lowers the reduction temperature of cobalt oxide [89].

From Figure 4.6 and Figure 4.7 it is evident that the supported cobalt catalysts consume more H_2 than the $CeO_2-Al_2O_3$ nanocomposites alone. This is most likely due to the reduction of cobalt oxide, but could also be attributed to a higher degree of reduction of ceria due to the presence of cobalt. The apparatus applied is not suitable for a quantitative measurement of the H_2 consumption, and there might exist differences between the analyses due to varying amounts of sample and H_2 pressure. The sharp peak at the maximum temperature in both figures indicates that complete reduction of the sample was not obtained at that temperature.

It is difficult to state how the presence of CeO_2 and Co_3O_4 influences the reduction abilities of one another. There exists no exact solution concerning the peak temperature, and the TPR results show that H_2 is consumed continuously from 550 K. A

general conclusion can be that the cobalt oxides are reduced at lower temperatures, whereas the ceria is reduced at higher temperatures.

4.2   Activity testing

Catalytic partial oxidation (CPO) of methane was done as described in Chapter 3.6. The equations used for calculating the molar flows of the products, conversion, selectivity and site-time yield, as well as example calculations, are shown in Appendix B. The amounts of other hydrocarbons (ethane, propane, etc.) produced were small and therefore neglected during further processing of the results. In Appendix D.3 all the details regarding the product analysis can be found.

CPO was done at different furnace temperatures and varying GHSV over reduced $Co/CeO_2-Al_2O_3$ and with a monolithic Co catalyst. The detailed results are found in Appendix D.4. Experiments were also done over unreduced $Co/CeO_2-Al_2O_3$ which are to be found on the CD enclosed to this report.
The catalysts are denoted with the calcination temperature of $CeO_2-Al_2O_3$ in parentheses after the chemical formula of the catalyst, e.g. $Co/CeO_2-Al_2O_3$ (1173 K). This should not be confused with the furnace temperature.

Since He was used as GC carrier gas, the amount of H_2 in the product stream was determined by the hydrogen balance in the system. However, at low H_2 production, i.e. when complete oxidation dominated, this calculation method gave negative values of H_2. This is probably due to small errors in the GC and/or MFC calibrations. In these cases the mole flow of H_2 was calculated directly from the GC analysis, such as with the other components. This should, however, give fairly correct numbers since calculations (not included in the thesis report) indicate that the difference between the two methods is small, around 5%.

4.2.1   CPO at different temperatures

Catalytic partial oxidation of methane was performed at furnace temperatures of 923 K, 1023 K and 1123 K. The results presented here are based on experiment number 7, 8, 12, 13 and 14. Three subsequent GC analyses were done at each furnace temperature, and the results are based on the average of the three analyses.

Figure 4.9 (a) and (b) show the conversion of methane for the catalysts as a function of the furnace temperature and the temperature at the catalyst bed exit, respectively. Plots of the selectivity towards the main products as functions of the bed exit temperatures are shown in Figure 4.10. The temperature profiles for the different catalysts are presented in Figure 4.11. Figure 4.12 shows the difference between the maximum and minimum temperature in the catalyst bed. The site-time yield (STY) and site yield of the production of the different products are displayed in Figure 4.13 and Figure 4.14.

Conversion
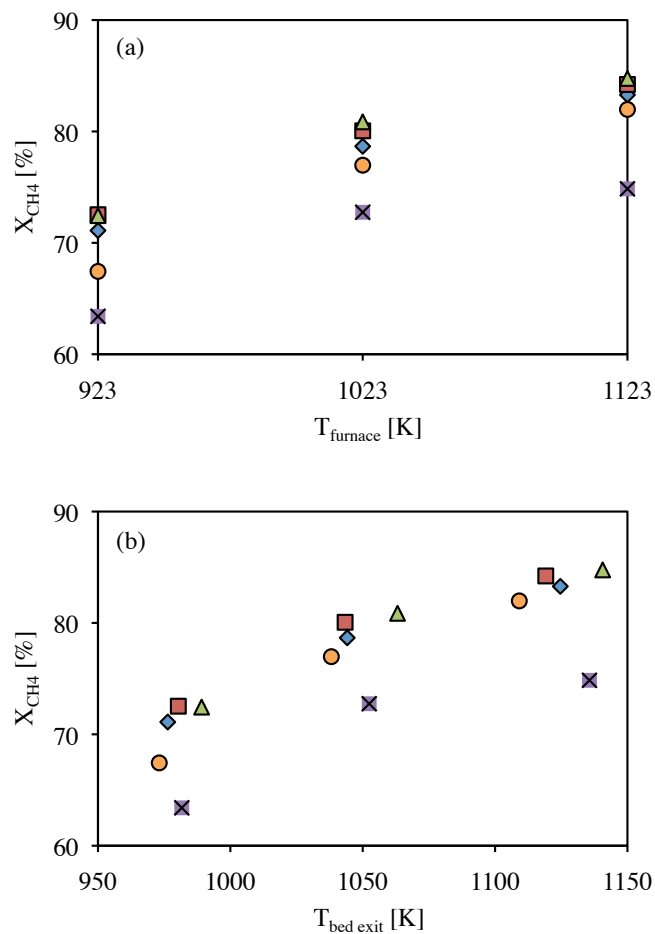
Figure 4.9: The conversion of CH_4 as a function of (a) the furnace temperature and (b) the catalyst bed exit temperature for CPO over $Co/CeO_2-Al_2O_3$ ◆ (1173 K), ■ (1273 K), ▲ (1373 K), ● (1423 K) and ✖ (1473 K). The furnace temperature was increased from 923 K to 1123 K. GHSV = 75 $L_{CH_4}/g_{cat}\cdot h$, P_{tot} = 1 atm, $CH_4:O_2:N_2$ = 2:1:3.72.

Selectivity
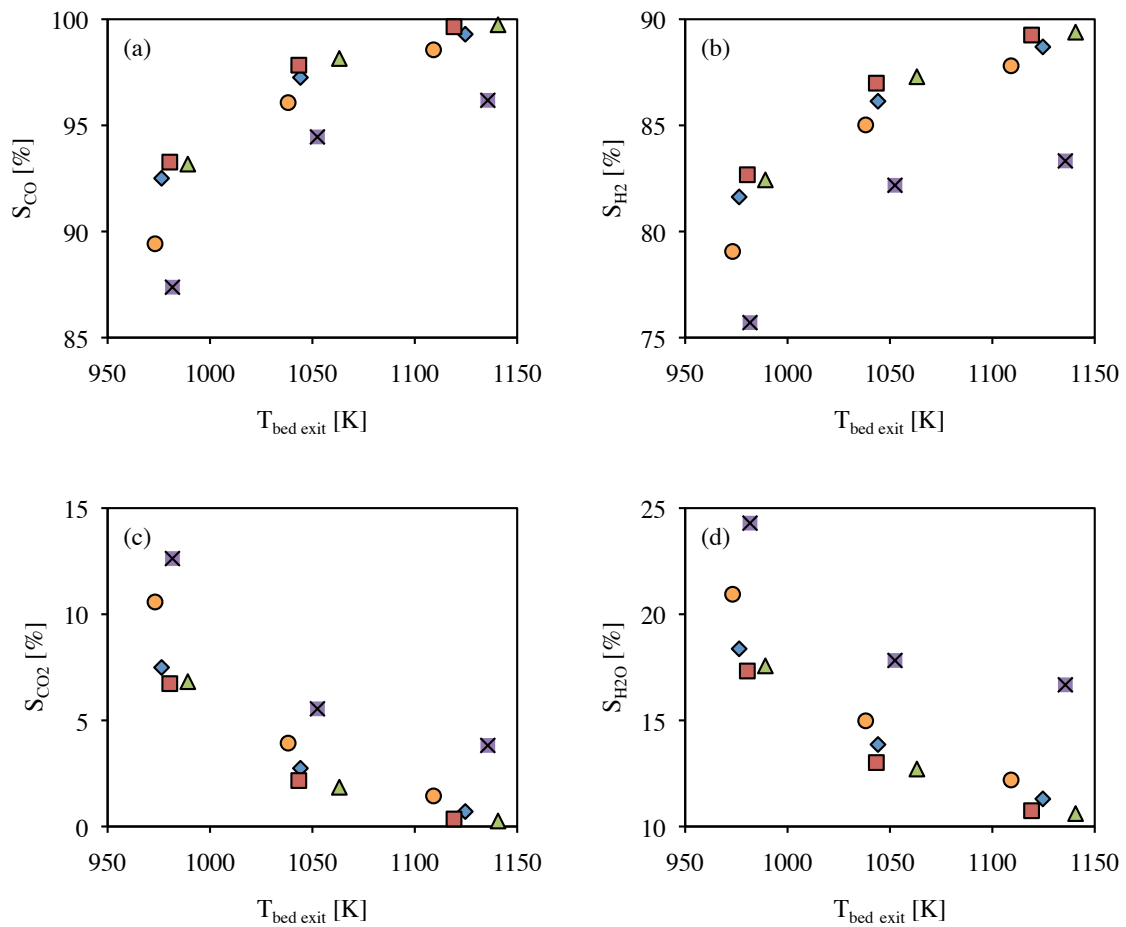
Figure 4.10: The selectivity towards (a) CO, (b) H_2, (c) CO_2 and (d) H_2O as a function of the catalyst bed exit temperature during CPO over $Co/CeO_2-Al_2O_3$ ◆ (1173 K), ■ (1273 K), ▲ (1373 K), ● (1423 K) and ✖ (1473 K) at furnace temperatures ranging from 923 K to 1123 K and a GHSV of 75 $L_{CH_4}/g_{cat}\cdot h$, P_{tot} = 1 atm, $CH_4:O_2:N_2$ = 2:1:3.72.

Temperature profile
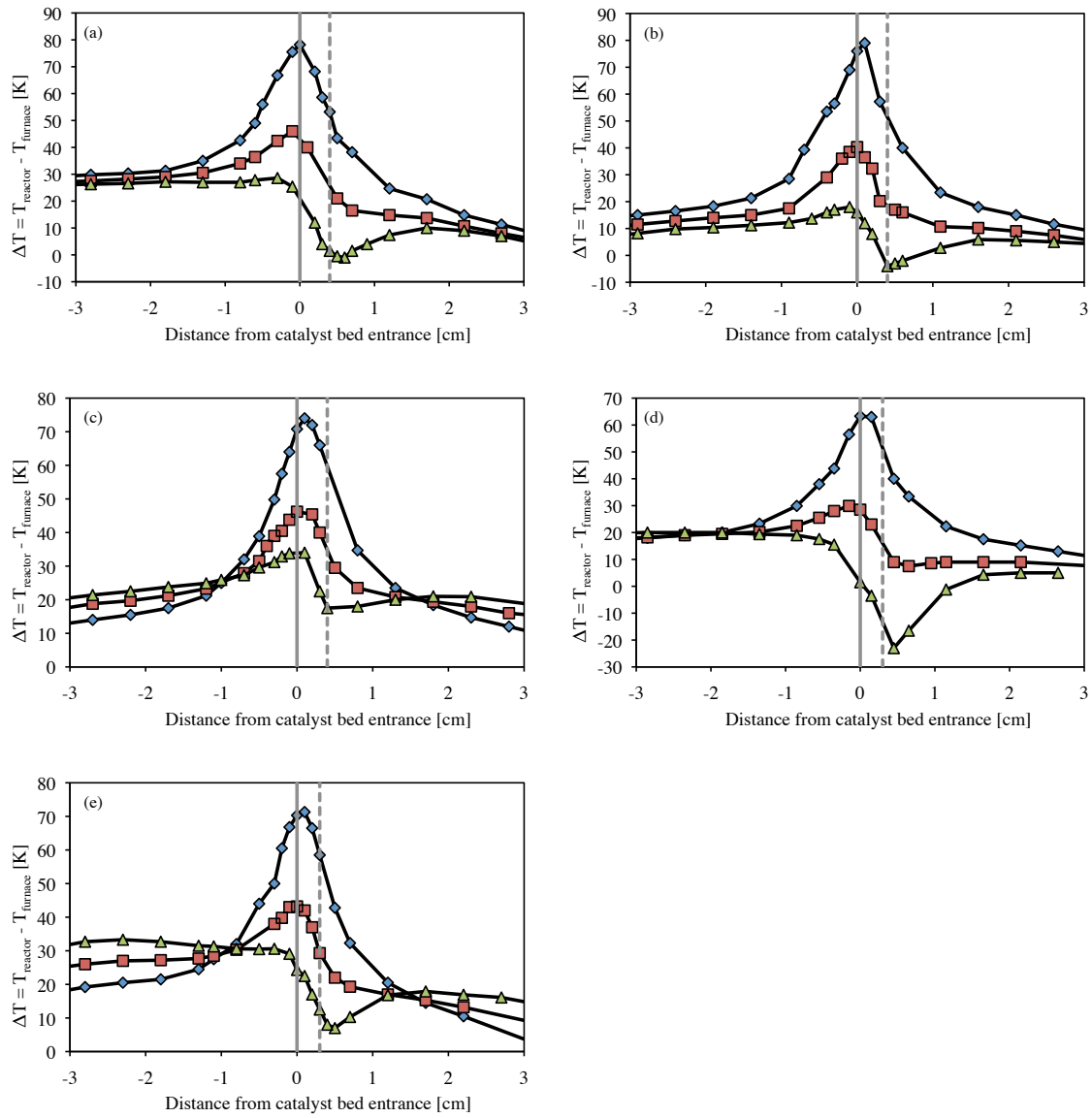
Figure 4.11: The temperature profiles for CPO experiments over Co/CeO_2-Al_2O (a) (1173 K), (b) (1273 K), (c) (1373 K), (d) (1423 K), (e) (1473 K) at different furnace temperatures. $T_{furnace} = 923$ K, $T_{furnace} = 1023$ K, $T_{furnace} = 1123$ K. Bed entrance and bed exit. GHSV of 75 $L_{CH_4}/g_{cat}\cdot$h, $P_{tot} = 1$ atm, $CH_4:O_2:N_2 = 2:1:3.72$.
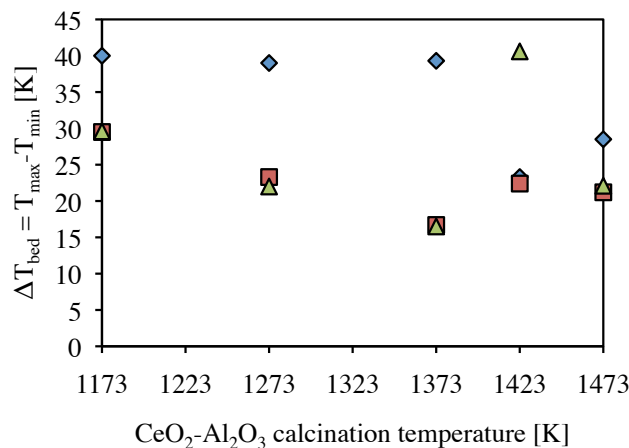
Figure 4.12: The difference between the highest and lowest temperature in the catalyst bed as a function of the $CeO_2-Al_2O_3$ calcination temperature for CPO over $Co/CeO_2-Al_2O_3$ at ◆ $T_{furnace}$ = 923 K, ■ $T_{furnace}$ = 1023 K and ▲ $T_{furnace}$ = 1123 K. GHSV = 75 $L_{CH_4}/g_{cat}\cdot$h, P_{tot} = 1 atm, CH_4:O_2:N_2 = 2:1:3.72. In the cases of no temperature minimum around the catalyst bed exit, T_{min} was determined to be the temperature slightly after the catalyst bed exit.

Site time yield
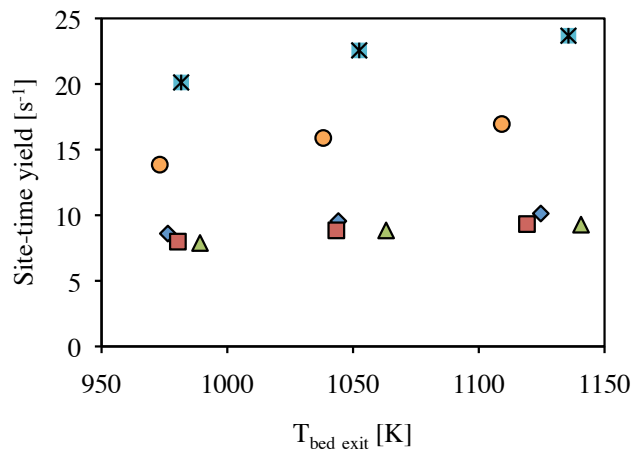
Figure 4.13: The site time yield of $Co/CeO_2-Al_2O_3$ ◆ (1173 K), ■ (1273 K), ▲ (1373 K), ● (1423 K) and ✳ (1473 K) as a function of the catalyst bed exit temperature. GHSV = 75 $L_{CH_4}/g_{cat}\cdot$h, P_{tot} = 1 atm, CH_4:O_2:N_2 = 2:1:3.72.
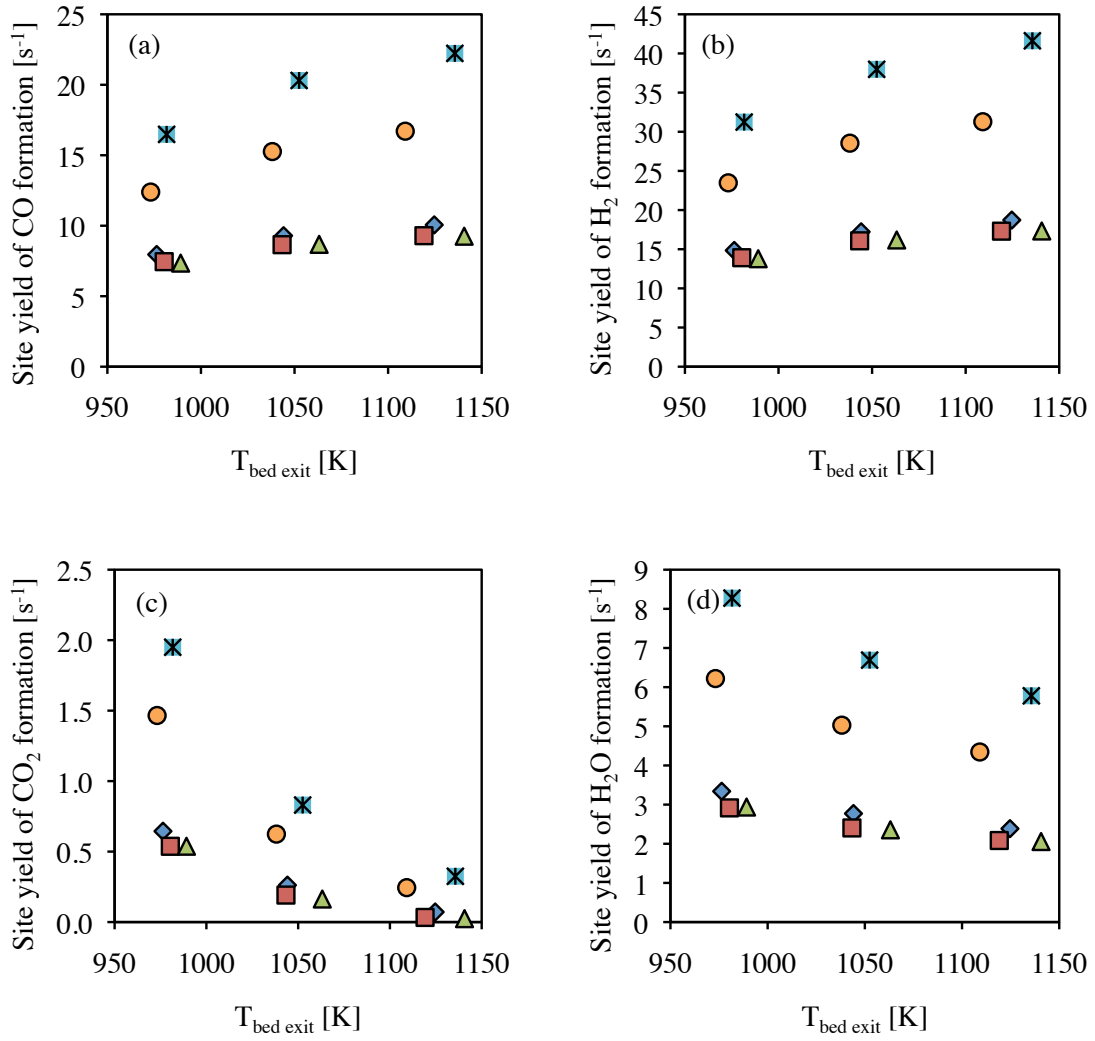
Figure 4.14: The site yield of (a) CO, (b) H_2, (c) CO_2 and (d) H_2O production for Co/CeO$_2$−Al$_2$O$_3$ ◆ (1173 K) and ■ (1273 K), △ (1373 K), ⬤ (1423 K) and ✳ (1473 K) as a function of the catalyst bed exit temperature. GHSV = 75 L$_{CH_4}$/g$_{cat}$·h, P$_{tot}$ = 1 atm, CH$_4$:O$_2$:N$_2$ = 2:1:3.72.

Effect of the furnace temperature

Figure 4.9 (a) shows an increasing conversion of methane as the furnace temperature increases. The results show that the conversion is acceptable at moderate temperatures such as 1023 K. The relative difference in the methane conversion between the furnace temperatures is larger for the transition from 923 K to 1023 K than for 1023 K to 1123 K.

Figure 4.9 (b) confirms that the conversion increases as a function of temperature at the catalyst bed exit, a trend that is anticipated based on thermodynamic considerations which are discussed in Section 2.1. The plot indicates a pattern of a gradual increase of the conversion which flattens out towards higher temperatures.
The selectivity towards CO and H_2 is, as expected, quite high in the high temperature range. For CO the selectivity is almost 100% at a furnace temperature of 1123 K. The selectivity towards H_2 is somewhat lower, which might be due to the water-gas shift reaction and perhaps the reduction of oxidized cobalt. The H_2/CO ratio is about 1.9 (see Appendix D.3) which is also found in literature [90]. This value is slightly lower than the stoichiometric. The selectivity towards CO and H_2 increases as a function of the temperature. As with the methane conversion it seems like the evolution of the selectivities follows a clear pattern. Even though the direct route to partial oxidation is an exotherm reaction, simulations show that the CH_4 conversion and selectivity towards CO and H_2 increase with temperature [2], which is reflected in the results shown here. For CO_2 and H_2 the trend is opposite. The selectivities decrease as a function of temperature, which is related to the higher degree of reforming at higher temperatures.

The temperature difference between the furnace and the catalyst bed decreases as the furnace temperature increases. From Figure 4.11 it can be seen that a furnace temperature of 923 K gives the highest temperature difference with a peak at around $\Delta T = 70$ K, whereas the two other furnace temperatures investigated give lower differences. Complete combustion becomes more dominating at lower temperatures, which explains the height of the peak. At higher temperatures the combustion reaction diminishes, which lowers the temperature peak, while there still is enough heat to drive the reforming reactions. These results are consistent with [90]. The sharp peaks ($\Delta T > 0$) indicate the formation of hotspots due to poor heat transfer in the catalyst. The grey vertical lines show the entrance and the exit of the catalyst bed. The temperature maximum is located at or slightly after the catalyst bed entrance which indicate that the highly exothermic complete oxidation takes place at the beginning of the catalyst bed, and that the temperature decreases quickly downwards through the bed. For the highest furnace temperature, the temperature difference between the bed and the furnace near the bed exit was even negative in some experiments, indicating that a endothermic reaction such as steam or dry reforming takes place.

In order to get a better impression of the temperature drop over the catalyst bed, the difference between the highest and the lowest temperature as a function of the $CeO_2-Al_2O_3$ calcination temperature is plotted in Figure 4.12. When merely

looking at the different furnace temperatures the trend indicates that a furnace temperature of 1023 K and 1123 K give about the same temperature difference over the bed, whereas the lowest furnace temperature gives a significantly higher temperature difference.

Figure 4.13 shows that the site-time yield increases as the temperature increases. The site yields of formation of the different products show the same trend as the selectivity.

Effect of the support calcination temperature

The results indicate that all the reduced cobalt catalysts give an overall high methane conversion and high selectivities towards CO and H_2. When comparing the CH_4 conversion of the different catalysts showed in Figure 4.9 (a) it is clear that the catalysts supported on $CeO_2-Al_2O_3$ calcined at the lowest temperatures give the highest conversion of methane. Figure 4.9 (b) shows that the difference in the conversion for the samples calcined at 1173 K to 1373 K are quite similar, whereas the samples calcined at 1423 K and 1473 K show a lower conversion. $Co/CeO_2-Al_2O_3$ (1273 K) shows the highest conversion as a function of the catalyst bed exit temperature. The same trend is observed for the selectivities, shown in Figure 4.10.

Due to a high conversion, temperature (and possibly concentration) gradients inside and between the catalyst particles, getting kinetic information from the reaction is quite challenging. The cobalt loading of 5 wt.% was chosen in an attempt to obtain low conversion. The results depicted in Figure 4.9 indicate that even with such a low cobalt loading the conversion is too high for differential conditions.

The N_2 adsorption-desorption measurements in Chapter 4.1.1 indicated a low surface area and H_2 chemisorption indicated low dispersion, thus large metal particles for $Co/CeO_2-Al_2O_3$ (1423 K) and (1473 K), which can explain the somewhat lowered conversion and selectivity. The conversion and selectivities of $Co/CeO_2-Al_2O_3$ (1173 K), (1273 K) and (1373 K) are quite similar. The estimated cobalt particle size for these catalyst are quite uniform, but their surface area and the CeO_2 crystallite size differs. Due to mass transfer limitations, fast oxidation reactions are not able to exploit a high surface area [6]. This implies that there exists an optimal catalyst surface area and that an increase in the surface area beyond a certain level does not enhance the catalytic activity. The results also point towards an apparent lack of contribution from the varying CeO_2 crystallite size, indicating that the increased molar fraction of oxygen vacancies, as the crystallite size of CeO_2 decreases, does not influence the partial oxidation of methane. The results cannot confirm or disclaim the contribution of oxygen from ceria on the reaction and stability of the catalyst, as was indicated in literature [31, 32].

In Figure 4.13 and Figure 4.14 the site-time yield and site yield of product formation are shown. The site-time yield is defined as the amount of methane converted per cobalt site per time. The data should be interpreted with care since it is obvious

from the temperature profiles in Figure 4.11 that there are no differential conditions in the reaction system, but rather different reactions and reaction rates inside the reactor. The quantitative formation of product per site is therefore an indication of the average activity and the relative differences between the different catalysts.

The STY and the site yields of the different products are more or less constant for the catalysts supported on $CeO_2-Al_2O_3$ calcined at 1173, 1273 and 1373 K. However, for those calcined at 1423 and 1473 K the STY and site yields are significantly higher, indicating that each catalytic site on these catalysts consumes and produces more per time relative to the other catalysts.

A first thought is that this is related to the cobalt particle size, and that larger particles exert higher activity than the smaller ones. A similar observation was done with the TOF for the Fischer-Tropsch reaction over a cobalt catalyst [91, 92]. In these cases the cobalt particle sizes were <10 nm. The surface structure of metal particles depend to a certain extent on the particle size. As the particle size increases the fraction of plane faces increases, whereas the fraction of low coordination corner and edge site decreases. However, beyond a certain particle size the ratio between the face sites and corner/edge sites is no longer influenced by the particle size [93]. This is supported by Van Hardeveld and Hartog who investigated the particle size effects on the surface structure and state that particles above about 6-7 nm predominantly contain surface atoms on the plane faces, and do not influence the catalytic activity due to their surface structure [94]. Bezemer et al. observed this effect for particles up to 8 nm. They explain the enhanced particle size effect with CO-induced surface reconstruction and nonclassical surface sensitivity [91]. There are some uncertainties related to the estimation of the cobalt particle size. However, if some of the H_2 were spilled onto the ceria the amount chemisorbed by cobalt would have been lower than anticipated, giving a lower dispersion and a larger particle size. It is therefore quite unlikely that the particles are smaller than estimated and that the results can be explained by the classical surface structure theory.

It could be speculated that the size of the particles and/or interaction with the support influences the bonding strength of a species, for example oxygen, and that this enhances or retards the overall catalytic activity. Small particles might show a stronger interaction with the support which in turn can influence their reducing and catalytic behavior. In addition, vacancies and impurities can influence the catalytic activity. The electronic and/or geometric surface structure can be altered by adsorption of another species in order to change the reactivity or improve the efficiency [95].

The high reaction rate and temperature gradients could induce transport limitations in and/or outside the catalyst particles. If the reaction happens faster than the diffusion of reactants into the pores, a fraction of the catalyst will be unavailable for the reacting species. The plots of the BET surface area and pore volume (Figure 4.1 and 4.2) of the support indicate that the $CeO_2-Al_2O_3$ calcined at 1423 K and 1473 K barely contain pores. The presence of heat and mass transfer limitations has been reported in the literature [2]. The transport of oxygen from the bulk gas phase to the catalyst is suggested to be the rate limiting step, and that there exists a

temperature gradient between the solid catalyst particles and the gas phase [96, 97].

Obtaining knowledge about the active sites on a catalyst surface and detailed information about the interaction between the catalyst and the reactants is a major challenge within catalysis, especially in complex reaction systems such as the one methane partial oxidation is a part of.
It must be stressed that due to the temperature gradient in the catalyst bed, the catalyst particles in the upper and lower part of the bed are not under the same conditions. Considering the indirect reaction mechanism, it can be assumed that they do not even have the same task. The calculated values for the STY and the site yield of product formation are average values and could be misleading because little of the actual reaction mechanism and kinetics is known.

There is considerable uncertainty related to the reaction mechanism of CPO. The interaction between the catalyst and the reacting species is therefore not fully understood. For the catalysts supported on $CeO_2-Al_2O_3$ calcined at 1173 K to 1373 K, there is an indication that the difference in the nature of the support does not influence the activity. The fact that $Co/CeO_2-Al_2O_3$ (1423 K) and (1473 K) show a lower catalytic activity could primarily be related to the increased cobalt particle size. Larger particles leave a larger fraction of the total amount of metal unused because the surface-to-volume ratio is lower than for smaller particles. Smaller particles give a net higher methane conversion and selectivity towards CO and H_2 because more of the cobalt can be utilized. The CeO_2 of these catalysts is expected to exhibit a lower degree of oxygen vacancy due to increased crystallite size of CeO_2. Since no relation between the ceria crystallite size and catalytic activity was detected for the (1173 K), (1273 K) and (1373 K) samples, it is assumed that this did not influence the result with $Co/CeO_2-Al_2O_3$ (1423 K) and (1473 K) either, and that the reduced activity is merely due to the increased cobalt particle size. The experimental reaction rate, i.e. the conversion of CH_4 or generation of product per mass of the catalyst per time (not shown here), shows no clear trend when comparing the different catalysts.

When considering the temperature profiles with respect to the different catalysts, Figure 4.12 gives an indication of the state of matter saying something about the vigorosity of the reaction and the interplay between the oxidation and reforming reactions. From Figure 4.12 is seems that the temperature difference follows no clear trend with respect to the different catalysts. For the highest furnace temperatures it appears to decrease as the calcination temperature of $CeO_2-Al_2O_3$ increases up to 1373 K, while for $T_{furnace} = 923$ K it stays constant. For the latter there was no clear temperature minimum around the catalyst bed exit, and the temperature decrease continues with the same ramp some distance after the bed exit, as can be seen in Figure 4.11. The decreasing temperature difference can be seen in connection to the decreasing conversion in Figure 4.9. $Co/CeO_2-Al_2O_3$ (1423 K) stands out. The high temperature difference at $T_{furnace} = 1123$ K indicates that this catalyst is highly active towards reforming (reaction (5) and (6) in Table 2.1 on page 3), causing a large temperature drop.
The difference between the temperature difference upstream and downstream of the

catalyst bed seen in Figure 4.11 could be owed to poor insulation and/or gas phase reaction outside of the catalyst bed. Gas phase chemistry related to back diffusion effects and insufficiently high linear gas velocity has been reported by Lødeng et al. [6].

CPO with unreduced catalyst

Experiments indicate that an unreduced cobalt catalyst (not shown) primarily generates CO_2 and H_2O. These findings are consistent with literature [21, 80, 84]. Hence, it can be suggested that the oxygen in the reactant gas mixture oxidizes the reduced cobalt as it hits the top of the catalyst bed, generating cobalt oxide in that area. The cobalt oxide catalyzes complete combustion of methane. The products CO_2 and H_2O are subsequently converted to CO and H_2 by dry and steam reforming, respectively. Further down in the reactor cobalt is in its metal form and heat generated from the combustion reaction shifts the reforming equilibrium. Steam and dry reforming can be catalyzed by cobalt catalysts [22, 98]. This supports the indirect reaction theory.

4.2.2 CPO at different GHSV

In order to locate the O_2 breakthrough an experiment was run at a fixed furnace temperature (1023 K) while increasing the GHSV gradually from 150 to 450 $L_{CH_4}/g_{cat}\cdot h$ over reduced $Co/CeO_2-Al_2O_3$ (1273 K). The results are based on experiment number 17. During the experiment, the analyses were done with 23 minute intervals, starting immediately after the reactants were introduced into the reactor. Finally, the space velocity was reset to 150 $L_{CH_4}/g_{cat}\cdot h$. The conversion of CH_4 and O_2 are plotted as functions of the time on stream in Figure 4.15 and the selectivity towards CO, H_2, CO_2 and H_2O are shown in Figure 4.16.
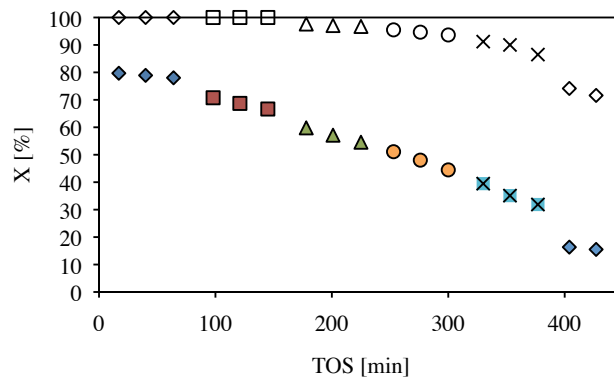
Figure 4.15: The conversion of CH_4 (filled makers) and O_2 (unfilled markers) at a GHSV of ◇ 150, ■ 250, △ 350, ● 400 and ✳ 450 $L_{CH_4}/g_{cat}\cdot h$ for $Co/CeO_2-Al_2O_3$ (1273 K) reduced *in situ* at a furnace temperature of 1023 K. P_{tot} = 1 atm, $CH_4:O_2:N_2$ = 2:1:3.72.
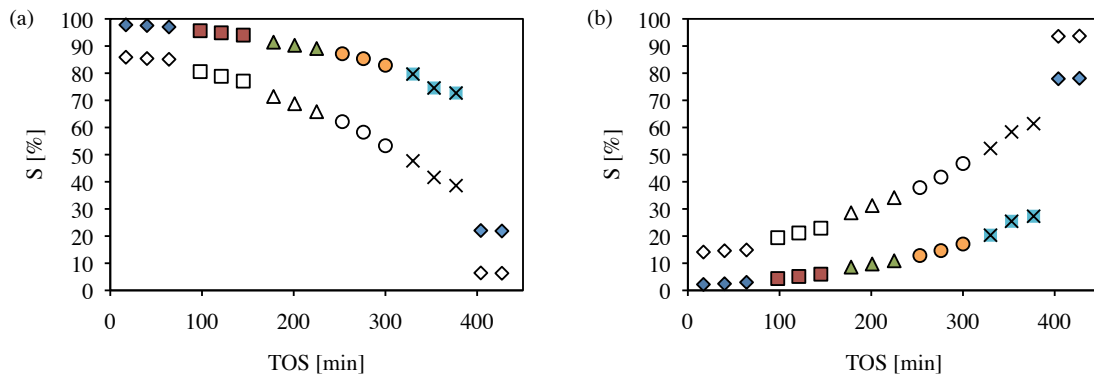
Figure 4.16: The selectivity of (a) CO (filled makers), H_2 (unfilled markers) and (b) CO_2 (filled makers) and H_2O (unfilled markers) at a GHSV of ◇ 150, ■ 250, △ 350, ● 400 and ✳ 450 $L_{CH_4}/g_{cat}\cdot h$ for $Co/CeO_2-Al_2O_3$ (1273 K) reduced *in situ* at a furnace temperature of 1023 K. P_{tot} = 1 atm, $CH_4:O_2:N_2$ = 2:1:3.72.

Figure 4.15 shows that the conversion of CH_4 and O_2 decreases as a function of the time on stream. Because of this, it is difficult to show the effect of the GHSV. The steps between the different space velocities, especially between 150, 250 and 350 $L_{CH_4}/g_{cat}\cdot h$, might indicate that a higher GHSV reduces the conversion of CH_4 and O_2 because the amount of catalyst naturally does not increase with the GHSV. This is also supported by Maestri et al. [97]. However, at higher GHSV the transition seems to be the due to the time on stream because of the apparent gradual transition between the different space velocities. It is also noteworthy that the conversion at 150 $L_{CH_4}/g_{cat}\cdot h$ after 400 minutes on stream is significantly lower than at the same space velocity at the beginning of the experiment. The methane conversion is controlled by a chemical regime at low flow rates and mass transfer at high flow rates due to higher catalyst bed temperatures [97]. Figure 4.16 (a) also shows a gradual decrease of the selectivity towards CO and H_2. The selectivity towards H_2 decreases faster than the selectivity towards CO. The selectivity towards CO_2 and H_2O increases correspondingly, as shown in Figure 4.16 (b).

At high flow rates the combustion of O_2 is not complete. The relative amount of H_2 and CO is controlled by the rate of consecutive combustions of which the oxidation of H_2 is much faster than the oxidation of CO. The amount of CO and H_2 in the product stream might be influenced by the oxidation of these two compounds since the conversion of O_2 is not complete, as well as by the equilibrium. As the conversion of O_2 drops below 100% it is likely that the oxygen present in the catalyst bed will oxidize the reduced cobalt metal, lowering the amount of catalyst available for CPO. Oxidized cobalt catalyzes the complete combustion of methane, and shows a lower degree of methane conversion than Co^0. The oxygen breakthrough will slowly lead to extinction of the reaction [6].

It is reported that the methane conversion and CO and H_2 selectivity increase as the GHSV increases [96]. This cannot be confirmed with the findings in this report, but is probably true for lower space velocities where oxygen breakthrough does not occur.

Figure 4.17 shows the profile of the temperature difference inside the reactor at different GHSV during CPO. The GHSV was increased from 150 to 450 $L_{CH_4}/g_{cat}\cdot h$, and then decreased to 150 $L_{CH_4}/g_{cat}\cdot h$ again.

The figure shows that the temperature difference between the catalyst bed and the furnace increases as the GHSV increases, indicating an increase of the exotherm nature of the process. This is due to the presence of more combustible reactants and is consistent with the findings by Boullosa and Maestri et al. [8, 97]. The increased space velocity gives a decreased contact time, enhanced heat and mass transfer coefficients and an increased average catalyst bed temperature. Complete combustion becomes more dominating, probably due to the oxidation of the catalyst.
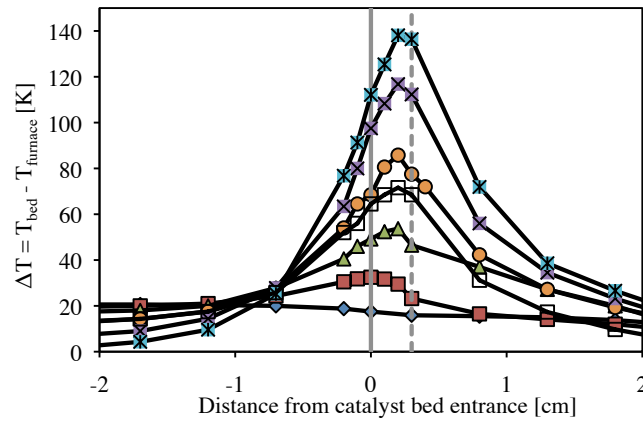
Figure 4.17: The temperature profile at different GSHV for CPO with $Co/CeO_2-Al_2O_3$ (1273 K) at 1023 K. ◆ No reaction, ■ 150, ▲ 250, ● 350, ✖ 400, ✕ 450 and ⊟ 150 $L_{CH_4}/g_{cat}\cdot h$. $P_{tot} = 1$ atm, $CH_4:O_2:N_2 = 2:1:3.72$.

Liu et al. assert that there exists a maximum for the CH_4 conversion and H_2 selectivity with respect to the flow rate and hence the resulting temperature profile inside the reactor [17]. At low flow rates the heat production from the oxidation is relatively low. This also gives a low degree of stream reforming, which is favored by high temperatures. When increasing the flow rate, more heat is released from the combustion reaction which shifts the reforming equilibrium. At high flow rates, however, the heat is quenched by the incoming "cold" gas and the CH_4 conversion and H_2 selectivity decreases. The maximum temperature inside the reactor reaches 1160 K, which probably causes sintering of the catalyst and hence deactivation of the catalyst, indicated by the reduced conversion.

Another observation from Figure 4.17 is that the temperature upstream of the catalyst bed is lower for the high GHSV and higher for the lower GHSV. Downstream, the trend is opposite. The increased flow rate provides more heat released by the reaction, giving a higher temperature inside the catalyst bed and therefore downstream of the catalyst bed. It also enhances the convective heat transfer by the incoming gas stream such that the area before the catalyst bed is cooled down [17].

4.2.3 Stability

In order to check the stability of $Co/CeO_2-Al_2O_3$ (1273 K), an experiment was run at a fixed GHSV and furnace temperature, respectively 75 $L_{CH_4}/g_{cat}\cdot h$ and 1023 K. The results are based on experiment number 19. The conversion of CH_4 and selectivities towards CO, H_2, CO_2 and H_2O are shown in Figure 4.18 (a) and (b), respectively.
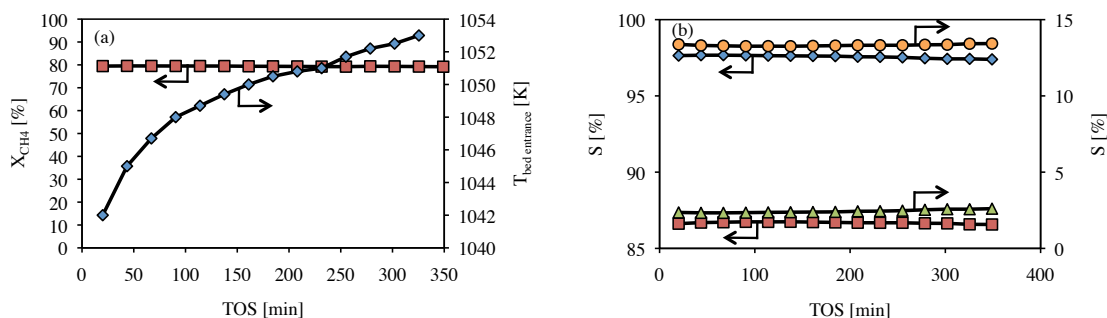
Figure 4.18: (a) The conversion of CH_4 and the temperature at the bed entrance and (b) the selectivity of ◆ CO, ■ H_2, ▲ CO_2 and ● H_2O as functions of the time on stream for $Co/CeO_2-Al_2O_3$ (1273 K) at a furnace temperature of 1023 K. GHSV = 75 $L_{CH_4}/g_{cat}\cdot$h, P_{tot} = 1 atm, $CH_4{:}O_2{:}N_2$ = 2:1:3.72.

These figures show that the conversion and selectivities stay more or less constant over the given time interval. Still a small decrease in the methane conversion and H_2 and CO selectivity, as well as a correspondingly small increase in the CO_2 and H_2O selectivity is observed. It is expected that the pre-reduced cobalt is not stable over time due to oxidation, which can explain the slightly visible trends shown in Figure 4.18 [7]. Running the experiment over a longer period of time will give more robust information about the catalyst stability.

Figure 4.18 (a) also shows the temperature at the catalyst bed entrance as a function of the time on stream. The plot shows that the temperature increases rapidly in the beginning and changes into a linear graph after approximately 90 minutes. This indicates that the system is not completely stabilizing even though the experimental conditions are kept constant and the conversion and selectivities are apparently stable. Linear regression of the linear part of the graph (not shown here) shows that the temperature changes with about 0.02 K per minute. The change is marginal in a short period of time. In order to be able to control the temperature at one fixed location in the reactor the thermocouple must preferably not be moved during the experiment. This is due to quite large temperature deviations over small steps in the axial position of the reactor which makes it difficult to place the thermocouple back on the same spot. This temperature evolution is therefore not recorded during other experiments where the thermocouple has been moved.

4.2.4 Structural changes during CPO

CPO experiments were run with both reduced and unreduced catalysts, giving variations in the physical properties of the spent catalyst. At the end of the experiments where the catalysts were reduced *in situ*, the top of the catalyst was blue, whereas the rest of the catalyst was dark grey or black. The catalysts that were not reduced were completely blue. A blue colour might indicate the presence of cobalt aluminate, $CoAl_2O_4$, whereas metallic cobalt and cobalt oxide are gray or black [99]. Arnoldy et al. report that catalysts calcined between 575 and 975 K are dark green to black, whereas catalysts calcined at temperatures above 1025 K turn blue [76]. Unreduced catalysts appeared to be more selective towards the total oxidation products CO_2 and H_2O and therefore became subject to a higher temperature as a consequence of that. High temperatures might induce the formation of cobalt aluminate. The spent catalyst from two experiments, one with catalyst reduc-

Figure 4.19: The XRD diffractograms of (1) fresh $Co/CeO_2-Al_2O_3$ (1273 K), (2) Spent $Co/CeO_2-Al_2O_3$ (1273 K) reduced *in situ* (Experiment 8) and (3) spent unreduced $Co/CeO_2-Al_2O_3$ (Experiment 16). Both experiments: $T_{furnace} = [923, 1023, 1123]$ K, GHSV = 75 $L_{CH_4}/g_{cat}\cdot h$, $P_{tot} = 1$ atm, $CH_4:O_2:N_2 = 2:1:3.72$.

tion and one with no reduction, were analyzed with XRD in order to detect any changes of the structure. The XRD diffractograms are shown in Figure 4.19. A clear difference between the diffractograms of the two spent catalysts can be seen. Identification of the peaks shows that the peaks formed with the unreduced catalyst (Figure 4.19 (3)) are indications of α-Al_2O_3. The diffractogram of the spent catalyst which was reduced *in situ* (Figure 4.19 (2)) is not significantly different from the one for the fresh catalyst (Figure 4.19 (1)).

To sum up, an unreduced catalyst catalyzes complete oxidation which causes a high temperature inside the reactor, which again induces structural changes of the catalyst, involving the transition to α-Al_2O_3 and $CoAl_2O_4$.

4.2.5 CPO with a monolithic catalyst

CPO with a monolith coated with alumina and impregnated with cerium and cobalt was done at a furnace temperature of 1013 K and at a GHSV of 8000 h^{-1}. The results are based on experiment number 18. The product gas was analyzed with intervals of 23 minutes, and the temperature at the top of the monolithic catalyst was surveilled during the whole experiment. When the temperature had stabilized the temperature profile inside the reactor was measured.

Figure 4.20 shows the evolution of the temperature at the top of the monolithic catalyst and the conversion of CH_4 as functions of the time on stream, given in minutes.
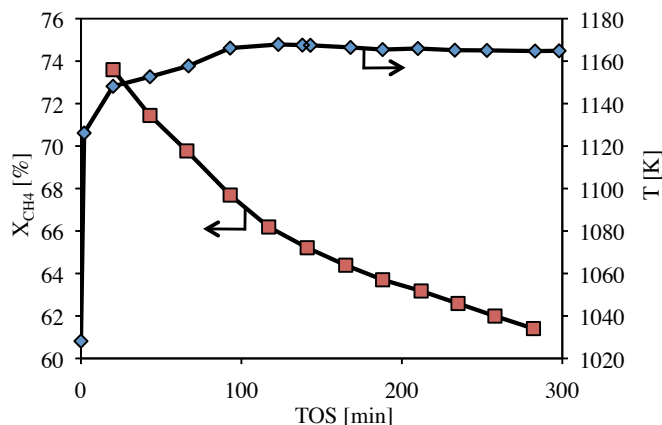
Figure 4.20: The temperature at the entrance of the 5 wt.%Co/[$CeO_2-Al_2O_3$] monolith and the conversion of CH_4 at different TOS. $\diamond$ $T_{\text{cat. entrance}}$ [K], $\blacksquare$ X_{CH_4} [%]. T_{furnace} = 1013 K, GHSV = 8000 h^{-1}, P_{tot} = 1 atm, CH_4:O_2:N_2 = 2:1:3.72.

Figure 4.20 shows that it took quite some time for the temperature to stabilize. In addition, the conversion showed a decreasing trend, even after the temperature at the bed entrance was stable. However, slope of the decreasing conversion became less steep and quite linear as the temperature stabilized. The conversion of O_2 was 100% during the whole experiment.

After impregnation with cobalt the monolith was calcined at 873 K. As the temperature in the reactor was higher than the calcination temperature, it is probable that the catalyst was subject to sintering during the course of the experiment. Sintering lowers the catalytic activity of a catalyst. It has previously been shown that ceria to some degree protects the alumina from sintering. However, the loading of CeO_2 on the alumina washcoat is unknown. Additionally, the cobalt loading was not confirmed.

The plots of the selectivities towards CO, H_2, CO_2 and H_2O given in Figure 4.21 show that the selectivity towards the two former products decreases as a function of time on stream, whereas the two latter increase, even when the temperature tends to settle at a fixed value (1165 K). The evolution of the selectivities give an indication of a slowly oxidizing cobalt catalyst. The temperature plot in Figure 4.20 indicates that the complete oxidation stays relatively constant. There is therefore reason to believe that the reforming in the lower part of the catalyst becomes less pronounced during the TOS.
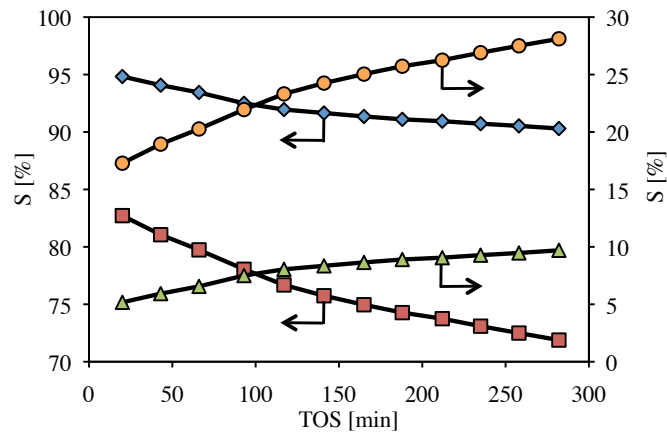
Figure 4.21: The selectivity [%] towards ◆ CO, ■ H_2, ▲ CO_2 and ● H_2O for the monolithic $Co/CeO_2-Al_2O_3$ catalyst at $T_{furnace}$ = 1013 K, GHSV = 8000 h^{-1}. P_{tot} = 1 atm, CH_4:O_2:N_2 = 2:1:3.72.

Figure 4.22 shows how the temperature changed in the axial direction of the reactor.
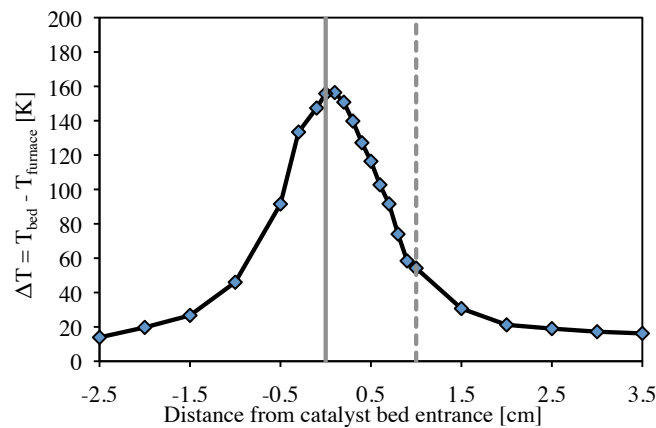
Figure 4.22: The temperature profile recorded at TOS = 190 min during the experiment with the $Co/CeO_2-Al_2O_3$ monolith. ◆ T [°C], ■ X_{CH_4} [%], ── Monolithic cat. entrance, ▬▬▬ Monolithic cat. exit. $T_{furnace}$ = 1013 K, GHSV = 8000 h^{-1}. P_{tot} = 1 atm, CH_4:O_2:N_2 = 2:1:3.72.

As it is generally believed that complete oxidation dominates at the top of the catalyst, and reforming closer to the bottom, it would have been convenient to rather focus on the temperature at the bottom instead of at the top. Still the temperature difference between the furnace and the catalyst bed at different positions is significantly higher than for the powdered catalyst, actually more comparable to the experiments with no reduction of the catalyst. The temperature and its effect on the catalyst can to a large degree explain the decreasing CH_4 conversion and selectivity towards CO and H_2.

The GHSV in the experiment was limited by the overall pressure drop over the system. In order to minimize the pressure drop, the GHSV was chosed to be 8000

h$^-$1. The GHSV in this experiment was quite low compared to similar experiments found in literature [37, 7, 15, 16, 43, 41, 42]. These articles predominantly involve Rh or Pt based catalysts.

4.3   Recommendations for further work

It must be emphasized that the validity of these results is limited because the results are based on one series of experiments. Reproduction of the results would give more structured results and enhance the understanding of the interplay between the heat formation and consumption. It is recommended to continue the investigation of the catalyst and the testing conditions.

During the experiments there was a problem with a pressure drop building up over the reactor. The pressure drop seemed only dependent on the temperature and gas flow, and there were no indications on coke formation, such as continuously increasing pressure at constant experimental conditions, catalyst deactivation or depositions on the reactor wall.
The catalyst powders were sieved again in order to exclude a larger fraction of fines. It appeared that the powders were fragile and fragmented easily after pelletizing. A solution could be to dilute the catalyst powder with γ-Al$_2$O$_3$ prior to pelletizing and sieving. The catalyst loading should of course be re-calculated.
The pressure drop over an empty reactor was tested with increasing flow rate of N$_2$ at standard pressure and temperature conditions. It appeared that a pressure drop started to build up at a flow rate of about 450 mL/min (STP). At about 560 mL/min (STP) the pressure drop was 0.1 bar. The pressure drop over the sinter might be caused by catalyst fines inside the sinter, as well as a too small diameter of the reactor. At a higher diameter-to-length ratio of the bed, the pressure drop should be lower. The pressure drop increases at higher temperatures, implying that the maximum flow rate giving no pressure drop decreases as the temperature increases, and that there by default exists a pressure drop at a certain temperature and gas flow rate. This limit should be found for the system, or a new reactor should be designed. The packing of the bed should also influence the pressure drop. However, with too loosely packed beds, gas channeling might occur. The gas penetrates the catalyst bed through channels, which severely inhibits the contact between the catalyst particles and the reactant gas.

The cobalt loading was chosen to be low (5 wt.%) in order to approach differential conditions in the reactor, low conversion and a slow reaction. In order to be able to investigate the kinetics of CPO of methane over cobalt catalysts the experimental conditions have be tuned such that the conversion is low and the temperature difference in the axial direction of the reaction is much lower. Diluting the feed gas could reduce the temperature gradients in the reactor and contribute to isothermal conditions.

In order to achieve a higher accuracy of the GC analyses, it is recommended to recalibrate the GC using gas mixtures with different composition. The calibration

curve will consist of more points and therefore provide reliable data at high and low concentrations of a compound. During the calibration of the GC one gas mixture was used and between each analysis small deviations were detected. When regarding the product analysis in Appendix D.4 and on the CD the error in the carbon balance is quite high in some cases (>5 %). It is suspected that this is due to an incorrect recording of CO_2. This matter should be investigated further. For the purposes of this work these issues have been regarded as negligible.

Even though the H_2 chemisorption provided reasonable information, there is still reason to believe that the use of CeO_2 invalidates the assumption that H_2 only adsorbs on the reduced cobalt. It would be interesting to optimize this technique for catalysts containing CeO_2.

The use of monoliths was briefly investigated in this thesis. Clearly, both the preparation method, characterization and activity testing must be given much more attention. The time limit of this work restricted the amount of time available for the monoliths a the construction of the rig and analyzing the powdered Co catalysts were prioritized. A more systemized and thorough investigation procedure of the preparation and characterization of the monoliths would therefore enhance the understanding of the catalytic behavior. Due to the weight loss after each calcination, it was difficult to determine the loading of the monolith. The loading was therefore estimated to be the same as the intended amount impregnated, i.e. 5 wt.%. Another challenge was that sheets of the washcoat as well as pieces of the cordierite structure tended to fall off during handling of the monolith.

Chapter 5

Conclusion

In this work 5 wt.% $Co/[CeO_2-Al_2O_3]$ catalysts have been characterized by N_2 adsorption-desorption, X-ray diffraction, temperature-programmed reduction and H_2 chemisorption, and their catalytic activity towards catalytic partial oxidation of methane has been tested in a lab-scale reactor. The catalysts differ by means of the calcination temperature of the $CeO_2-Al_2O_3$.

The BET surface area and pore volume decrease as the $CeO_2-Al_2O_3$ calcination temperature increases. The TPR analyses confirmed the reducibility of CeO_2 and that the interaction between cobalt and ceria mutually influences their reducibility. The cobalt particle size was estimated by H_2 chemisorption giving cobalt sizes of about 12 nm for $Co/CeO_2-Al_2O_3$ (1173 K), (1273 K) and (1373 K) and 21 and 28 nm for $Co/CeO_2-Al_2O_3$ (1423 K) and (1473 K), respectively. There is reason to believe that hydrogen spillover onto the ceria occurred during H_2 chemisorption and that the cobalt particles therefore are larger than estimated. The XRD analysis could not give an unambiguous relation between the lattice parameters, CeO_2 crystallite size and presence of cobalt.

The catalytic partial oxidation of methane has successfully been done over all the catalysts, obtaining high CH_4 conversion and selectivity towards CO and H_2. $Co/CeO_2-Al_2O_3$ (1173 K), (1273 K) and (1373 K) showed the best performance, followed by $Co/CeO_2-Al_2O_3$ (1423 K) and (1473 K). The catalysts with low surface area and low cobalt dispersion gave lower conversion than the catalysts with higher surface area and higher dispersion.
No evident correlation between the particle size of the CeO_2 and the catalytic activity was discovered. The results also indicate that the reaction is limited by mass transfer.

A monolith has been coated with Al_2O_3 and impregnated with ceria and cobalt (5 wt.%). CPO over the monolith showed adequately high conversion and selectivity. However, the stability of the catalyst was low which probably is due to sintering of the particles.

Bibliography

[1] Xyntéo. The future role of natural gas. A position paper by the European Gas Avocacy Forum, May 2011.

[2] B. C. Enger, R. Lødeng, and A. Holmen. A review of catalytic partial oxidation of methane to synthesis gas with emphasis on reaction mechanisms over transition metal catalysts. *Applied Catalysis A: General*, 346:1–27, 2008.

[3] A. P. E. York, T. Xiao, and M. L. H. Green. Brief overview of the partial oxidation of methane to synthesis gas. *Topics in Catalysis*, 22:345–358, 2003.

[4] I. Chorkendorff and J. W. Niemantsverdriet. *Concepts of modern catalysis and kinetics*. WILEY-VCH Verlag GmbH & Co., 2nd edition, 2007.

[5] H. Liander. The utilisation of natural gases for the ammonia process. *Transactions of the Faraday Society*, 25:462–472, 1929.

[6] R. Lødeng, E. Bjørgum, B. C. Enger, J. L. Eilertsen, A. Holmen, B. Krogh, M. Rønnekleiv, and E. Rytter. Catalytic partial oxidation of CH_4 to H_2 over cobalt catalysts at moderate temperatures. *Applied Catalysis A: General*, 333:11–23, 2007.

[7] S. Cimino, G. Landi, L. Lisi, and G. Russo. Development of a dual functional structured catalyst for partial oxidation of methane to syngas. *Catalysis Today*, 105:718–723, 2005.

[8] S. Boullosa Eiras. *Comparative study of selected catalysts for methane partial oxidation*. PhD thesis, Norwegian University of Science and Technology, 2010.

[9] A. Trovarelli, editor. *Catalysis by ceria and related materials*, volume 2 of *Catalytic Science Series*. Imperial College Press, 2002.

[10] B. C. Enger, R. Lødeng, and A. Holmen. Modified cobalt catalysts in the partial oxidation of methane at moderate temperatures. *Journal of Catalysis*, 262:188–198, 2009.

[11] M. Fathi, E. Bjørgum, T. Viig, and O. A. Rokstad. Partial oxidation of methane to synthesis gas: Elimination of gas phase oxygen. *Catalysis Today*, 63:489–497, 2000.

[12] J. A. Moulijn, M. Makkee, and A. van Diepen. *Chemical process technology.* John Wiley & Sons, Ltd., 2001.

[13] M. W. Smith and D. Shekhawat. *Fuel Cells*, chapter 5, pages 73–128. Elsevier B.V., 2001.

[14] A. P. E. York, T. Xiao, M. L. H. Green, and J. B. Claridge. Methane oxyforming for synthesis gas production. *Catalysis Reviews*, 49:511–560, 2007.

[15] D. A. Hickman and L. D. Schmidt. Production of syngas by direct catalytic oxidation of methane. *Science*, 259:343–346, 1993.

[16] D. A. Hickman, E. A. Haupfear, and L. D. Schmidt. Synthesis gas formation by direct oxidation of methane over Rh monoliths. *Catalysis Letters*, 17:223–237, 1993.

[17] T. Liu, C. Snyder, and G. Veser. Catalytic partial oxidation of methane: Is a distinction between direct and indirect pathways meaningful? *Industrial & Engineering Chemistry Research*, 46:9045–9052, 2007.

[18] H. Y. Wang and E. Ruckenstein. Partial oxidation of methane to synthesis gas over alkaline earth metal oxide supported cobalt catalysts. *Journal of Catalysis*, 199:309–317, 2001.

[19] Å. Slagtern, H. M. Swaan, U. Olsbye, I. M. Dahl, and C. Mirodatos. Catalytic partial oxidation of methane over Ni-, Co- and Fe-based catalysts. *Catalysis Today*, 46:107–115, 1998.

[20] E. Ruckenstein and H. Y. Wang. Effect of support on partial oxidation of methane to synthesis gas over supported rhodium catalysts. *Journal of Catalysis*, 187:151–159, 1999.

[21] L. F. Liotta, G. Di Carlo, G. Pantaleo, and G. Deganello. Catalytic performance of Co_3O_4/CeO_2 and Co_3O_4/CeO_2-ZrO_2 composite oxides for methane combustion: Influence of catalyst pretreatment and oxygen concentration in the reaction mixture. *Applied Catalysis B: Environmental*, 70:314–322, 2007.

[22] E. Ruckenstein and H. Y. Wang. Carbon dioxide reforming of methane to synthesis gas over supported cobalt catalysts. *Applied Catalysis A: General*, 204:257–262, 2000.

[23] *ASM Handbook: Properties and selection: Nonferrous alloys and special-purpose materials. Vol 2.* ASM International, 1990.

[24] H. Y. Wang and E. Ruckenstein. Conversions of methane to synthesis gas over co/γ-Al_2O_3 by CO_2 and/or O_2. *Catalysis Letters*, 75:13–18, 2001.

[25] E. Ruckenstein and H. Y. Wang. Carbon deposition and catalytic deactivation during CO_2 reforming of CH_4 over Co/γ-Al_2O_3 catalysts. *Journal of Catalysis*, 205:289–293, 2002.

[26] T. Tsukada, H. Segawa, A. Yasumori, and K. Okada. Crystallinity of boehmite and its effect on the phase transition temperature of alumina. *Journal of Materials Chemistry*, 9:549–553, 1999.

[27] P. S. Santos, H. S. Santos, and S. P. Toledo. Standard transition aluminas. Electron microscopy studies. *Materials Research*, 3:104–114, 2000.

[28] S. Boullosa Eiras, E. Vanhaecke, T. Zhao, D. Chen, and A. Holmen. Raman spectroscopy and X-ray diffraction study of the phase transformation of $ZrO_2-Al_2O_3$ and $CeO_2-Al_2O_3$ nanocomposites. *Catalysis Today*, 166:10–17, 2011.

[29] S. Eriksson, U. Nyklén, S. Rojas, and M. Boutonnet. Preparation of catalysts from microemulsions and their applications in heterogeneous catalysis. *Applied Catalysis A: General*, 265:207–219, 2004.

[30] B. M. Reddy, K. N. Rao, and P. Bharali. Copper promoted cobalt and nickel catalysts supported on ceria-alumina mixed oxide: Structural characterization and CO oxidation activity. *Industrial & Engineering Chemistry Research*, 48:8478–8486, 2009.

[31] K. Otsuka, Y. Wang, E. Sunada, and I. Yamanaka. Direct partial oxidation of methane to synthesis gas by cerium oxide. *Journal of Catalysis*, 175:152–160, 1998.

[32] F. A. Silva, D. S. Martinez, J. A. C. Ruiz, L. V. Mattos, C. E. Hori, and F. B. Noronha. The effect of the use of cerium-doped alumina on the performance of $Pt/CeO_2/Al_2O_3$ and $Pt/CeZrO_2/Al_2O_3$ catalysts on the partial oxidation of methane. *Applied Catalysis A: General*, 335:145–152, 2008.

[33] J.-Y. Luo, M. Meng, X. Li, X.-G. Li, Y.-Q. Zha, T.-D. Hu, Y.-N. Xie, and J. Zhang. Mesoporous $Co_3O_4-CeO_2$ and $Pd/Co_3O_4-CeO_2$ catalysts: Synthesis, characterization and mechanistic study of their catalytic properties for low-temperature CO oxidation. *Journal of Catalysis*, 254:310–324, 2008.

[34] T. Vergunst, F. Kapteijn, and J. A. Moulijn. Monolithic catalysts — non-uniform active phase distribution by impregnation. *Applied Catalysis A: General*, 213:179–187, 2001.

[35] A. Cybulski and J. A. Moulijn. Monoliths in heterogeneous catalysis. *Catalysis Reviews: Science and Engineering*, 36:179–270, 1994.

[36] J. W. Geus and J. C. van Giezen. Monoliths in catalytic oxidation. *Catalysis Today*, 47:169–180, 1999.

[37] A. S. Bodke, S. S. Bharadwaj, and L. D. Schmidt. The effect of ceramic supports on partial oxidation of hydrocarbons over noble metal coated monoliths. *Journal of Catalysis*, 179:138–149, 1998.

[38] R. M. Hech, S. Gulati, and R. J. Farrauto. The application of monoliths for gas phase catalytic reactions. *Chemical Engineering Journal*, 82:149–156, 2001.

[39] I. M. Lachman and J. L. Williams. Extruded monolithic catalyst supports. *Catalysis Today*, 14:317–329, 1992.

[40] J. L. Williams. Monolith structures, materials, properties and uses. *Catalysis Today*, 69:3–9, 2001.

[41] J. K. Hochmuth. Catalytic partial oxidation of methane over a monolith supported catalyst. *Applied Catalysis B: Environmental*, 1:89–100, 1992.

[42] R. Schwiedernoch, S. Tischer, C. Correa, and O. Deutschmann. Experimental and numerical study on the transient behavior of partial oxidation of methane in a catalytic monolith. *Chemical Engineering Science*, 58:633–642, 2003.

[43] S. Kado, K. Imagawa, A. Kiryu, F. Yagi, T. Minami, H. Kawai, K. Kawazuishi, K. Tomishige, A. Nakamura, and Y. Suehiro. Syngas production from natural gas via catalytic partial oxidation using ceramic monolith catalyst at short contact time and elevated pressure. *Catalysis Today*, 171:97–103, 2011.

[44] K. P. de Jong. Synthesis of supported catalysts. *Current Opinion in Solid State & Materials Science*, 4:55–62, 1999.

[45] Ø. Borg, P. D. C. Dietzel, A. I. Spjelkavik, E. Z. Tveten, J. C. Walmsley, S. Diplas, S. Eri, A. Holmen, and E. Rytter. Fischer-Tropsch synthesis: Cobalt particle size and support effects on intrinsic activity and product distribution. *Journal of Catalysis*, 259:161–164, 2008.

[46] H. Song and U. S. Ozkan. The role of impregnation medium on the activity of ceria-supported cobalt catalysts for ethanol steam reforming. *Journal of Molecular Catalysis A: Chemical*, 318:21–29, 2010.

[47] A. J. van Dillen, R. J. A. M. Terörde, D. J. Lensveld, J. W. Geus, and K. P. de Jong. Synthesis of supported catalysts by impregnation and drying using aqueous chelated metal complexes. *Journal of Catalysis*, 216:257–264, 2003.

[48] A. Miyazaki, I. Balint, K. Aika, and Y. Nakano. Preparation of Ru nanoparticles supported on γ-Al_2O_3 and its novel catalytic activity for ammonia synthesis. *Journal of Catalysis*, 204:364–371, 2001.

[49] T. A. Nijhuis, A. E. W. Beers, T. Vergunst, I. Hoek, F. Kapteijn, and J. A. Moulijn. Preparation of monolithic catalysts. *Catalysis Reviews*, 43:345–380, 2001.

[50] S. Brunauer, P. H. Emmett, and E. Teller. Adsorption of gases in multimolecular layers. *Journal of the American Chemical Society*, 60:309–319, 1938.

[51] K. S. W. Sing. The use of nitrogen adsorption for the characterisation of porous materials. *Colloids and Surfaces A: Physicochemical and Engineering Aspects*, 187-188:3–9, 2001.

[52] K. S. W. Sing, D. H. Everett, R. A. W. Haul, L. Moscou, R. A. Pierotti, J. Rouquérol, and T. Siemieniewska. Reporting physisorption data for gas/solid systems with special reference to the determination of surface area and porosity. *Pure & Applied Chemistry*, 57:603–619, 1985.

[53] J. Rouquerol, D. Avnir, C. W. Fairbridge, D. H. Everett, J. H. Haynes, N. Pernicone, J. D. F. Ramsay, K. S. W. Sing, and K. K. Unger. Recommendations for the characterization of porous solids. *Pure & Applied Chemistry*, 66:1739–1758, 1994.

[54] K. S. W. Sing. Adsorption methods for the characterization of porous materials. *Advances in Colloid and Interface Science*, 76-77:3–11, 1998.

[55] R. Di Monte, P. Fornasiero, J. Kaspar, P. Rumori, G. Gubitosa, and M. Graziani. $Pd/Ce_{0.6}Zr_{0.4}O_2/Al_2O_3$ as advanced materials for three-way catalysts. Part 1. Catalyst characterisation, thermal stability and catalytic activity in the reduction of NO by CO. *Applied Catalysis B: Environmental*, 24:157–167, 2000.

[56] P. A. Sermon and G. C. Bond. Hydrogen spillover. *Catalysis Reviews*, 8:211–239, 1974.

[57] S. P. Rane. *Relation between catalyst properties and selectivity in Fischer-Tropsch synthesis*. PhD thesis, Norwegian University of Science and Technology, 2011.

[58] M. Boudart. Turnover rates in heterogeneous catalysis. *Chemical Review*, 95:661–666, 1995.

[59] S. Bernal, J. J. Calvino, G. A. Cifredo, A. Laachir, V. Perrichon, and J. M. Herrmann. Influence of the reduction/evacuation conditions on the rate of hydrogen spillover on Rh/CeO_2 catalysts. *Langmuir*, 10:717–722, 1994.

[60] P. Malet and A. Caballero. The selection of experimental conditions in temperature programmed reduction experiments. *Journal of the Chemical Society, Faraday Transactions*, 84:2369–2375, 1988.

[61] F. Giordano, A. Trovarelli, C. de Leitenburg, and M. Giona. A model for the temperature-programmed reduction of low and high surface area ceria. *Journal of Catalysis*, 193:273–282, 2000.

[62] P. J. Baugh, editor. *Gas chromatography: a practical approach*. II. Series. Oxford University Press, 1993.

[63] S. A. A. Glas. Catalytic partial oxidation of methane at moderate temperatures. TKP 4510, 2012.

[64] J. L. Lemaitre, P. G. Menon, and F. Delannay. *Characterization of heterogeneous catalysts*, volume 15. Marcel Dekker Inc., 1984.

[65] B. C. Enger, R. Lødeng, J. Walmsley, and A. Holmen. Inactive aluminate spinels as precursors for design of CPO and reforming catalysts. *Applied Catalysis A: General*, 383:119–127, 2010.

[66] C. H. Bartholomew. Hydrogen adsorption on supported cobalt, iron and nickel. *Catalysis Letters*, 7:27–52, 1990.

[67] J. Liu, Z. Zhao, J. Wang, C. Xu, A. Duan, G. Jiang, and Q. Yang. The highly active catalysts of nanometric CeO_2-supported cobalt oxides for soot combustion. *Applied Catalysis B: Environmental*, 84:185–195, 2008.

[68] A. S. P. Lovón, J. J. Lovón-Quintana, G. I. Almerindo, G. P. Valença, M. I. B. Bernardi, V. D. Araújo, T. S. Rodrigues, P. A. Robles-Dutenhefner, and H. V. Fajardo. Preparation, structural characterization and catalytic properties of Co/CeO_2 catalysts for the steam reforming of ethanol and hydrogen production. *Journal of Power Sources*, 216:281–289, 2012.

[69] S. Kumar, Y. J. Kim, B. H. Koo, H. Choi, and C. G. Lee. Structural and magnetic properties of Co doped CeO_2 nano-particles. *IEEE Transactions on magnetics*, 45:2439–2441, 2009.

[70] J. E. Spanier, R. D. Robinson, F. Zhang, S.-W. Chang, and I. P. Herman. Size-dependent properties of CeO_{2-y} nanoparticles as studied by Raman scattering. *Physical Review B*, 64:245407, 2001.

[71] X. Wang, J. A. Rodriguez, J. C. Hanson, D. Gamarra, A. Martínez-Arias, and M. Fernández-García. In situ studies of the active sites for the water gas shift reaction over $Cu-CeO_2$ catalysts: Complex interaction between metallic copper and oxygen vacancies of ceria. *Journal of Physical Chemistry B*, 110:428–434, 2006.

[72] J. M. Gatica, R. T. Baker, P. Fornasiero, S. Bernal, G. Blanco, and J. Kaspar. Rhodium dispersion in a $Rh/Ce_{0.68}Zr_{0.32}O_2$ catalyst investigated by HRTEM and H_2 chemisorption. *Journal of Physical Chemistry B*, 104:4667–4672, 2000.

[73] J. M. Gatica, R. T. Baker, P. Fornasiero, S. Bernal, and J. Kaspar. Characterization of the metal phase in $NM/Ce_{0.68}Zr_{0.32}O_2$ (NM: Pt and Pd) catalysts by hydrogen chemisorption and HRTEM microscopy: A comparative study. *Journal of Physical Chemistry B*, 105:1191–1199, 2001.

[74] L. Sparado, F. Arena, M. L. Granados, M. Ojeda, J. L. G. Fierro, and F. Frusteri. Metal-support interactions and reactivity of Co/CeO_2 catalysts in the Fischer-Tropsch synthesis reaction. *Journal of Catalysis*, 234:451–462, 2005.

[75] A. I. Kozlov, D. H. Kim, A. Yezerets, P. Andersen, H. H. Kung, and M. C. Kung. Effect of preparation method and redox treatment on the reducibility and structure of supported ceria-zirconia mixed oxide. *Journal of Catalysis*, 209:417–426, 2002.

[76] P. Arnoldy and J. A. Moulijn. Temperature-programmed reduction of CoO/Al_2O_3 catalysts. *Journal of Catalysis*, 93:38–54, 1985.

[77] N. W. Hurst, S. J. Gentry, A. Jones, and B. McNicol. Temperature programmed reduction. *Catalysis Reviews: Science and Engineering*, 24:233–309, 1982.

[78] L. A. Bruce, M. Hoang, A. E. Hughes, and T. W. Turney. Ruthenium promotion of Fischer-Tropsch synthesis over coprecipitated cobalt/ceria catalysts. *Applied Catalysis A: General*, 100:51–67, 1993.

[79] P. G. Harrison, I. K. Ball, W. Daniell, P. Lukinskas, M. Cépedes, E. E. Miró, and M. A. Ulla. Cobalt catalysts for the oxidation of diesel soot particulate. *Chemical Engineering Journal*, 95:47–55, 2003.

[80] L. F. Liotta, G. Di Carlo, G. Pantaleo, and G. Deganello. Co_3O_4/CeO_2 and Co_3O_4/CeO_2-ZrO_2 composite catalysts for methane combustion: Correlation between morphology reduction properties and catalytic activity. *Catalysis Communications*, 6:329–336, 2005.

[81] M.-F. Luo, J.-M. Ma, J.-Q. Lu, Y.-P. Song, and Y.-J. Wang. High-surface area $CuO-CeO_2$ catalysts prepared by a surfactant-templated method for low-temperature CO oxidation. *Journal of Catalysis*, 246:52–59, 2007.

[82] H. Cordatos, D. Ford, and R. J. Gorte. Simulated annealing study of the structure and reducibility in ceria clusters. *Journal of Physical Chemistry*, 100:18128–18132, 1996.

[83] F. M. Z. Zotin, L. Tournayan, J. Varloud, V. Perrichon, and R. Fréty. Temperature-programmed reduction: limitation of the technique for determining the extent of reduction of either pure ceria or ceria modified by additives. *Applied Catalysis A: General*, 98:99–114, 1993.

[84] L. F. Liotta, G. Di Carlo, G. Pantaleo, A. M. Venezia, and G. Deganello. Co_3O_4/CeO_2 composite oxides for methane emissions abatement: Relationship between $Co_3O_4-CeO_2$ interaction and catalytic activity. *Applied Catalysis B: Environmental*, 66:217–227, 2006.

[85] H.-Y. Lin and Y.-W. Chen. The mechanism of reduction of cobalt by hydrogen. *Materials Chemistry and Physics*, 85:171–175, 2004.

[86] B. Jongsomjit, J. Panpranot, and J. G. Goodwin Jr. Co-support compound formation in alumina-supported cobalt catalysts. *Journal of Catalysis*, 204:98–109, 2001.

[87] A. Machocki, A. Denis, W. Grzegorczyk, and W. Gac. Nano- and micro-powder of zirconia and ceria-supported cobalt catalysts for the steam reforming of bio-ethanol. *Applied Surface Science*, 256:5551–5558, 2010.

[88] S. Storsæter, B. Tøtdal, J. Walmsley, B. S. Tanem, and A. Holmen. Characterization of alumina-, silica-, and titania-supported cobalt Fischer-Tropsch catalysts. *Journal of Catalysis*, 236:139–152, 2005.

[89] C.-L. Yu, J.-B. Hu, W.-Z. Weng, X.-C. Zhou, and X.-R. Chen. Preparation of $Co/Ce_{0.5}Zr_{0.5}O_2$ catalysts and their catalytic performance in methane partial oxidation to produce synthesis gas. *Journal of Fuel Chemistry and Technology*, 40:418–423, 2012.

[90] S. Boullosa Eiras, T. Zhao, E. Vanhaecke, D. Chen, and A. Holmen. Partial oxidation of methane to synthesis gas on $Rh/Zr_xCe_{1-x}O_2 - Al_2O_3$. *Catalysis Today*, 178:12–24, 2011.

[91] G. L. Bezemer, J. H. Bitter, H. P. C. E. Kuipers, H. Oosterbeek, J. E. Holewijn, X. Xu, F. Kapteijn, A. J. van Dillen, and K. P. de Jong. Cobalt particle size effects in the Fischer-Tropsch reaction studied with carbon nanofiber supported catalysts. *Journal of the American Chemical Society*, 128:3956–3964, 2006.

[92] N. Fischer, E. van Steen, and M. Claeys. Structure sensitivity of the Fischer-Tropsch activity and selectivity on alumina supported cobalt catalysts. *Journal of Catalysis*, 299:67–80, 2013.

[93] J. T. Richardson. *Principles of catalyst development*. Fundamental and applied catalysis. Plenum Press, 1989.

[94] R. van Hardeveld and F. Hartog. The statistics of surface atoms and surface sites on metal crystals. *Surface Science*, 15:189–230, 1969.

[95] E. M. McCash. *Surface chemistry*. Oxford University Press, 2001.

[96] M. Bizzi, L. Basini, G. Saracco, and V. Specchia. Short contact time catalytic partial oxidation of methane: analysis of transport phenomena effects. *Chemical Engineering Journal*, 90:97–106, 2002.

[97] M. Maestri, A. Beretta, G. Groppi, E. Tronconi, and P. Forzatti. Comparison among structured and packed-bed reactors for the catalytic partial oxidation of CH_4 at short contact times. *Catalysis Today*, 105:709–717, 2005.

[98] L. P. R. Profeti, E. A. Ticianelli, and E. M. Assaf. Co/Al_2O_3 catalysts promoted with noble metals for production of hydrogen by methane steam reforming. *Fuel*, 87:2067–2081, 2008.

[99] D. A. Lide, editor. *Handbook of chemistry and physics*. CRC Press.

Appendix A

Catalyst

A.1 Catalyst synthesis

Powdered catalyst

The amounts and concentrations of the various chemicals used in order to make the $CeO_2(20 \text{ wt\%})$-Al_2O_3 support are listed in Table A.1 and A.2.

Table A.1: The amounts used during the synthesis of 20 wt.% $CeO_2-Al_2O_3$ during spring 2012 [63].

Chemical	First batch	Second batch
γ-Al_2O_3 Puralox	20.0065 g	20.0148 g
$Ce(NO_3)_3 6 H_2O$	12.6130 g	12.6178 g
CA	11.1337 g	11.4204 g
PEG	~15 g	~15 g
Distilled water	150 mL	150 mL

Table A.2: The amounts used during the synthesis of 20 wt.% $CeO_2-Al_2O_3$ 17.09.2012.

Chemical	Amount
γ-Al_2O_3 Puralox	20.0019 g
$Ce(NO_3)_3 \cdot 6H_2O$	12.6168 g
CA	12.2080 g
PEG	15.4695 g
Distilled water	150 mL

The amounts used to synthesize the cobalt catalysts are listed in Table A.3.

Table A.3: The amounts used in the synthesis of 5 wt.% $Co/CeO_2-Al_2O_3$

Chemical		(1173 K)	(1273 K)	(1373 K)	(1423 K)	(1473 K)
Support	[g]	4.3251	4.3487	4.0098	1.1113	1.3005
$Co(NO_3)_2 6\,H_2O$, calc.	[g]	1.0680	1.0738	0.9901	0.9986	0.9917
$Co(NO_3)_2 6\,H_2O$, added	[g]	1.0688	1.0768	0.9956	0.9970	0.9941
H_2O+EG, calc.	[mL]	3.5320	2.9705	1.9670	1.4205	1.1179
H_2O+EG, added	[mL]	3.5	2.9	1.9670	1.2	0.9

Monolithic catalyst

One $Co/CeO_2-Al_2O_3$ monolith was prepared. First a washcoat layer of approximately 15 wt.% was applied, then impregnation in a solution containing ceria, and finally impregnation in a cobalt solution. In Table A.4 the details after each washcoat cycle (dip, blow, dry, weigh) are listed.

Table A.4: Monolithic catalyst preparation

	m [g]	$\mathbf{m_{diff.}}$ [g]	$\mathbf{m_{total\ diff.}}$ [g]	**Wt.% washcoat** [%]
		Al_2O_3-washcoat		
Start	0.6940			
1	0.7276	0.0336	0.0336	4.6
2	0.7589	0.0313	0.0649	8.6
3	0.7869	0.028	0.0929	11.8
4	0.8198	0.0329	0.1258	15.3
5	0.9602	0.0404	0.1662	19.3
Calcination	0.8227	-0.0375	0.1287	15.6

	$\mathbf{m_{after\ drying}}$ [g]	$\mathbf{m_{diff.}}$ [g]	$\mathbf{m_{after\ calc.}}$ [g]	$\mathbf{m_{diff.}}$ [g]
		CeO2 impregnation		
1	0.8331	0.0104	0.8132	-0.0199
2	0.8223	0.0091	0.8043	-0.0176

$\mathbf{m_{before}}$ [g]	$\mathbf{m_{after}}$ [g]	$\mathbf{m_{H_2O\ absorbed}}$ [g]
	Distilled H_2O	
0.8018	1.0206	0.2188

$\mathbf{m_{after\ drying}}$ [g]	$\mathbf{m_{after\ calc.}}$ [g]
	Co impregnation
0.8173	

A.2   Properties of chemicals

Puralox SCCa (Sasol)

The chemical and physical properties of Puralox SCCa (Sasol) are given in Table A.5.

Table A.5: Puralox SCCa (Sasol)

Al_2O_3	[%]	98
Na_2O	[%]	0.002
L.O.I.	[%]	4.0
Loose bulk density	[g/L]	600-850
Packed bulk density	[g/L]	700-1150
Particle size	[μm]	60-150
Range of surface area (BET)	[m^2/g]	90-210
Pore volume	[mL/g]	0.35-0.5
Pore radius	[nm]	4-10
Thermal stability		
Surfae area: 24h/1100 °C	[m^2/g]	15
Surfae area: 24h/1200 °C	[m^2/g]	5

Disperal P2 (Sasol)

The chemical and physical properties of γ-Al_2O_3 Disperal P2 from Sasol are given in Table A.6.

Table A.6: Properties of Disperal P2 (Sasol)

Al_2O_3	[%]	72
Na_2O	[%]	0.002
NO_3	[%]	4.0
Loose bulk density	[g/L]	850
Particle size	[μm]	45
Surface area (BET)	[m^2/g]	260
Pore volume	[mL/g]	0.5
Crystallite size	[nm]	4.5
Dispersed particle size	[nm]	25
Water dispersibility	[%]	97

Cordierite (Corning)

The properties of the cordierite monolith are given in Table A.6.

Table A.7: Properties of cordierite monolith

Cell geometry	Square
Cell density	62.2 cells/cm^2
Wall thickness	0.16 mm
Hydraulic diamter	1.1 mm
Open area	76%
Surface/volume	2790 m^2/m^3
Open porosity	33%
Mean pore size	3.5 μm
Thermal expansion coefficient	10 $\cdot$ 10^{-7} °C
Axial rupture strength	3000 psi
Melting point	1450 °C

Appendix B

Calculations

B.1 Equations

The software connected to the GC provided the volume percentages of the different compounds detected by the GC which are based on the following equation:

$$y_{i(\text{GC})} = A_i \cdot RF_i \tag{B.1}$$

where A_i is the integrated area and RF_i is the response factor of compound i. The response factors for the different compounds can be found in Appendix D.2.

The reported volume fractions of the different compounds in the product stream detected by the TCD were normalized. The normalized volume fractions are found by dividing the volume fraction given by the GC by the sum of all compounds. Please note that H_2 is excluded due to inaccuracies related to the use of He as carrier gas.

$$y_{i(\text{GC, norm})} = \frac{y_{i(\text{GC})}}{(y_{N_2} + y_{CO} + y_{CO_2} + y_{CH_4})_{\text{GC}}} \tag{B.2}$$

N_2 was used as an internal standard. This gives the assumption that the amount of N_2 fed into the reactor equals the amount of N_2 in the product gas, since N_2 does not take part in any reaction.

$F_{N_2(\text{feed})}$ was found by applying the ideal gas law to the known volume flow [mL/min] of N_2 in the feed gas.

Since the molar flow of N_2 is known $(F_{N_2} = F_{tot(\text{feed})} \cdot y_{N_2(\text{feed})})$, the total molar flow of the product gas can be found by B.3.

$$F_{tot(\text{prod.})} = \frac{F_{N_2}}{y_{N_2(\text{GC, norm})}} \tag{B.3}$$

The molar flows of the different compouds are subsequently found by multiplying the normalized mole fraction with the total product mole flow.

$$F_{i(\text{prod.})} = y_{i(\text{GC, norm})} \cdot F_{tot\text{prod.}} \tag{B.4}$$

The material balance over the different components was set up according to the following, using C as an example:

$$F_C = F_{CO} + F_{CO_2} + F_{CH_4} + 2 \cdot F_{\text{Etan}} + 2 \cdot F_{\text{Eten}} + 3 \cdot F_{\text{Propen}} + ... \tag{B.5}$$

The amounts of H_2 and H_2O produced were calculated by using the material balance over O and H.

The mole flow of O through H_2O is given by

$$F_{O(H_2O)} = F_{O(\text{feed})} - F_{O(CO,CO_2)} \tag{B.6}$$

which gives a molar production rate of H_2O of

$$F_{H_2O} = F_{O(H_2O)} \tag{B.7}$$

The H provided by H_2 is defined as

$$F_{H(H_2)} = F_{H(\text{feed})} - F_{H(HC)} - 2 \cdot F_{O(H_2O)} \tag{B.8}$$

where HC stands for hydrocarbons. The expression for the flow rate of H_2 is

$$F_{H_2} = \frac{F_{H(H_2)}}{2} \tag{B.9}$$

The conversion

The conversion of CH_4, X_{CH_4}, is defined as the number of moles CH_4 converted divided by the number of moles CH_4 in the feed.

$$X_{CH_4} = \frac{y_{CO} + y_{CO_2}}{y_{CO} + y_{CO_2} + y_{CH_4}} \tag{B.10}$$

The selectivity

The selectivity is defined as the ratio between the number of moles of the desired product and the number of moles reactant converted. The selectivity with respect to CO is given in equation B.11

$$S_{CO} = \frac{y_{CO}}{y_{CO} + y_{CO_2}} \tag{B.11}$$

The selectivity towards H_2 is given in Equation B.12

$$S_{H_2} = \frac{y_{H_2}}{y_{H_2} + y_{H_2O}} \tag{B.12}$$

The same equations can be applied in order to calculate S_{CO_2} and S_{H_2O}, by changing the numerator in Equation B.11 and B.12, respecitvely.

The yield

The yield of a certain compound is defined as the ratio between the molar flow of that compound in the product stream and the theoretical

$$Y_{H_2} = \frac{F_{H_2}}{2 \cdot F_{CH_4(in)}} \tag{B.13}$$

The site time yield (STY)

The site-time yield is calculated like the turn-over frequency (TOF).

$$\text{STY} = \frac{r_{CH_4} \cdot M_{Co}}{x_{Co} \cdot D_{Co}} \tag{B.14}$$

where r_{CH_4} [mol/(g$_{cat.}$·s)] is the experimental reaction rate with respect to the conversion of CH_4, M_{Co} [g/mol] the molar mass of Co, x_{Co} [-] the weight fraction of Co on the catalyst and D_{Co} [-] the dispersion of Co.

The rate of reaction is calculated by

$$r_{CH_4} = \frac{F_{CO} + F_{CO_2}}{m_{catalyst}}$$

The site yield of formation of the products is calculated in the same way as the STY, but with the rate of formation of the individual products instead of the total conversion of methane.

$$\text{Site yield of formation of } i = \frac{r_i \cdot M_{Co}}{x_{Co} \cdot D_{Co}} \tag{B.15}$$

where i is either CO, H_2, CO_2 or H_2O, $r_{H_2} = \frac{F_{H_2}}{m_{catalyst}}$ and the other factors are the same as mentioned above.

B.2   Examples

Synthesis

The starting point of calculating the amount needed in order to prepare CeO_2(20 wt.%)-Al_2O_3 was the desired total mass of the support, e.g. 25 g.

Mass of CeO_2:

$$m_{CeO_2} = 0.2 \cdot 25 \text{ g} = 5 \text{ g}$$

Moles of CeO_2:

$$n_{CeO_2} = \frac{m_{CeO_2}}{M_{CeO_2}} = \frac{5}{172.1} \text{ mol} = 2.91 \cdot 10^{-2} \text{ mol}$$

Moles of $Ce(NO_3)_2 6 H_2O$:

$$n_{Ce(NO_3)_2 6 H_2O} = n_{CeO_2}$$

Mass of $Ce(NO_3)_2 6 H_2O$:

$$m_{Ce(NO_3)_2 6 H_2O} = n_{Ce(NO_3)_2 6 H_2O} \cdot M_{Ce(NO_3)_2 6 H_2O}$$
$$= 2.91 \cdot 10^{-2} \cdot 434.25 \text{ g} = \underline{12.6163 \text{ g}}$$

The amount of metal precursor was calculated based on the total mass of each support. 5 wt.% Co on $CeO_2-Al_2O_3$ aged at 1173 K will be used as an example.

$$m_{CeO_2-Al_2O_3} = 4.3251 \text{ g}$$

$$m_{Co} = 0.05 \cdot m_{CeO_2-Al_2O_3} = 0.05 \cdot 4.3251 \text{ g} = 0.2163 \text{ g}$$

$$n_{Co} = \frac{m_{Co}}{M_{Co}} = \frac{0.2163}{58,93} \text{ mol} = 3.67 \cdot 10^{-3} \text{ mol}$$

$$n_{Co(NO_3)_2 6 H_2O} = n_{Co}$$

$$m_{Co(NO_3)_2 6 H_2O} = n_{Co(NO_3)_2 6 H_2O} \cdot M_{Co(NO_3)_2 6 H_2O}$$
$$= 3.67 \cdot 10^{-3} \cdot 291.03 \text{ g} = \underline{1.0680 \text{ g}}$$

BET surface area

In order to find the amount of nitrogen adsorbed on the first monolayer of the material, only the first part of the adsorption isotherm, e.g. up till $p/p_0 = 0.2$, is taken into account. Plotting the $P/V_a(P_0-P)$ as a function of $P/P0$ gives a straight line, as shown in Figure B.1 for the case of $CeO_2-Al_2O_3$ calcined at 1173 K, which has the slope α and intersects the y-axis at η.
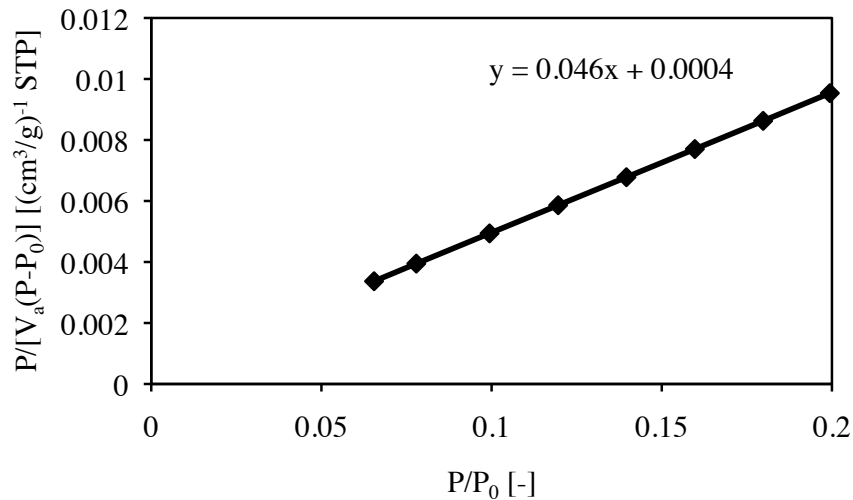
Figure B.1: The BET plot for $CeO_2-Al_2O_3$ (1173 K)

The volume adsorbed in the first monolayer, V_0, calculated applying equation (2.2).

$$V_0 = \frac{1}{0.046 + 0.0004} = 21.60 \text{ cm}^3/\text{g (STP)}$$

The number of molecules adsorbed, N_0, is given by equation (2.3)

$$N_0 = \frac{2.16 \cdot 10^{-5} \cdot 101\,325}{1.38 \cdot 10^{-23} \cdot 273.15} = 5.80 \cdot 10^{20} \text{ molecules/g}$$

At 77 K N_2 occupies 0.162 nm^2 [4]. The total surface area is therefore

$$S_{BET} = 5.80 \cdot 10^{20} \cdot 0.162 \cdot 10^{-18} = 9.40 \cdot 10^{20} = \underline{94 \text{ m}^2/\text{g}}$$

This number agrees well with the number provided by the apparatus.

Dispersion and metal particle size

The volume of hydrogen adsorbed was found by extrapolating the linear part at low pressures, as shown in Figure C.5 for $Co/CeO_2-Al_2O_3$ (1173 K).

$$v_{ads} = 0.7657 \text{ cm}^3/\text{g (STP)}$$

The dispersion is calculated employing equation (2.7):

$$D = \frac{0.7657 \cdot 58.933 \cdot 2}{0.05 \cdot 22400} \cdot 100\% = \underline{8.06\%}$$

The particle size is calculated with equation (2.9):

$$d_m = \frac{99.6}{8.06} = \underline{12.4 \text{ nm}}$$

Conversion

Exp. 7 at 923 K is used in this example calculation.

$$X_{CH_4} = \frac{(0.0553 + 0.0045) \text{ mmol/s}}{(0.0553 + 0.0045 + 0.0243) \text{ mmol/s}} \cdot 100\% = \underline{71.10\%}$$

Selectivity

Exp. 7 at 923 K is used in this example calculation.

$$S_{CO} = \frac{0.0553 \text{ mmol/s}}{0.0553 + 0.0045 \text{ mmol/s}} \cdot 100\% = \underline{92.30\%}$$

Site-time yield

Exp. 7 at 923 K is used in this example calculation.

Catalyst: $Co/CeO_2-Al_2O_3$ (1173 K)
$m_{cat} = 0.1016$ g
$D_{Co} = 0.08058$
$M_{Co} = 58.93$ g/mol

The experimental rate of reaction is found by

$$r = \frac{(0.0553 + 0.0045) \cdot 10^{-3} \text{ mol/s}}{0.1016 \text{ g}} = 5.88157 \cdot 10^{-4} \text{ mol/(s} \cdot \text{g)}$$

The site-time yield is

$$\text{STY} = \frac{5.88157 \cdot 10^{-4} \text{ (mol/s} \cdot \text{g)} \cdot 58.93 \text{ g/mol}}{0.05 \cdot 0.08058} = \underline{8.6 \text{ s}^{-1}}$$

Appendix C

Characterization

C.1   N$_2$ adsorption-desorption

BET surface area

In order to get an impression of the accuracy of the N$_2$ adsorption-desorption method for estimating the specific surface area the experiment was done twice with samples from the same batch. The results are listed in Table C.4.

Table C.1: BET surface area of CeO$_2$−Al$_2$O$_3$ of two analyses from the same batch (Sep-12)

	CeO$_2$−Al$_2$O$_3$	
T$_{calc.}$ [K]	First	Second
1173	93.9	94.1
1273	73.9	70.6
1373	46.9	49.0
1423	24.0	23.5
1473	4.6	4.5

The BET surface area of the first batch of CeO$_2$−Al$_2$O$_3$ made during spring 2012 (Jan-12) and the Puralox used in the synthesis is presented in Table C.2.

Table C.2: BET surface area for CeO$_2$−Al$_2$O$_3$ [63] and the Puralox

T$_{calc.}$ [K]	CeO$_2$−Al$_2$O$_3$	Puralox
1173	103	129
1273	71	100
1373	33	9
1423	10	6
1473	3	4

The BET surface area of $Co/CeO_2-Al_2O_3$ and $CeO_2-Al_2O_3$ (Apr-12) calcined at 1373 K are presented in Table C.3.

Table C.3: BET surface area for $CeO_2-Al_2O_3$ and $Co/CeO_2-Al_2O_3$ [63]

$T_{calc.}$ [K]	$CeO_2-Al_2O_3$	$Co/CeO_2-Al_2O_3$
1173	-	90
1273	-	66
1373	37.7	37
1423	-	11
1473	-	5

Adsorption desorption isotherms

In Figure C.1 the adsorption-desorption isotherms for $CeO_2-Al_2O_3$ are shown.

(a) $CeO_2-Al_2O_3$ 1173 K

(b) $CeO_2-Al_2O_3$ 1273 K

(c) $CeO_2-Al_2O_3$ 1373 K

(d) $CeO_2-Al_2O_3$ 1423 K

(e) $CeO_2-Al_2O_3$ 1473 K
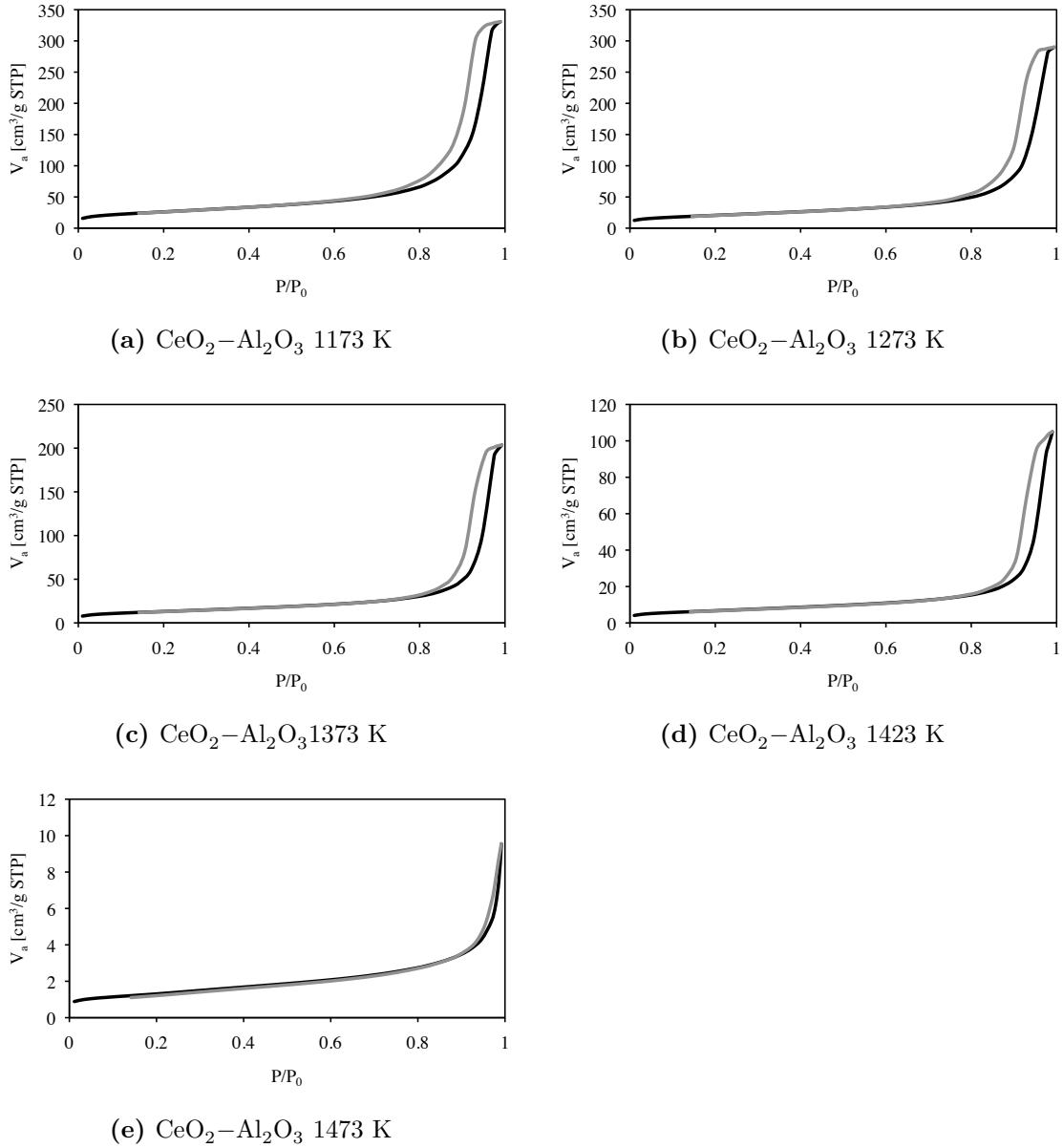
Figure C.1: The N$_2$ adsorption-desorption isotherms for $CeO_2-Al_2O_3$

In Figure C.2 the adsorption-desorption isotherms for Puralox are shown.

(a) Puralox 1173 K

(b) Puralox 1273 K

(c) Puralox1373 K

(d) Puralox 1423 K

(e) Puralox 1473 K
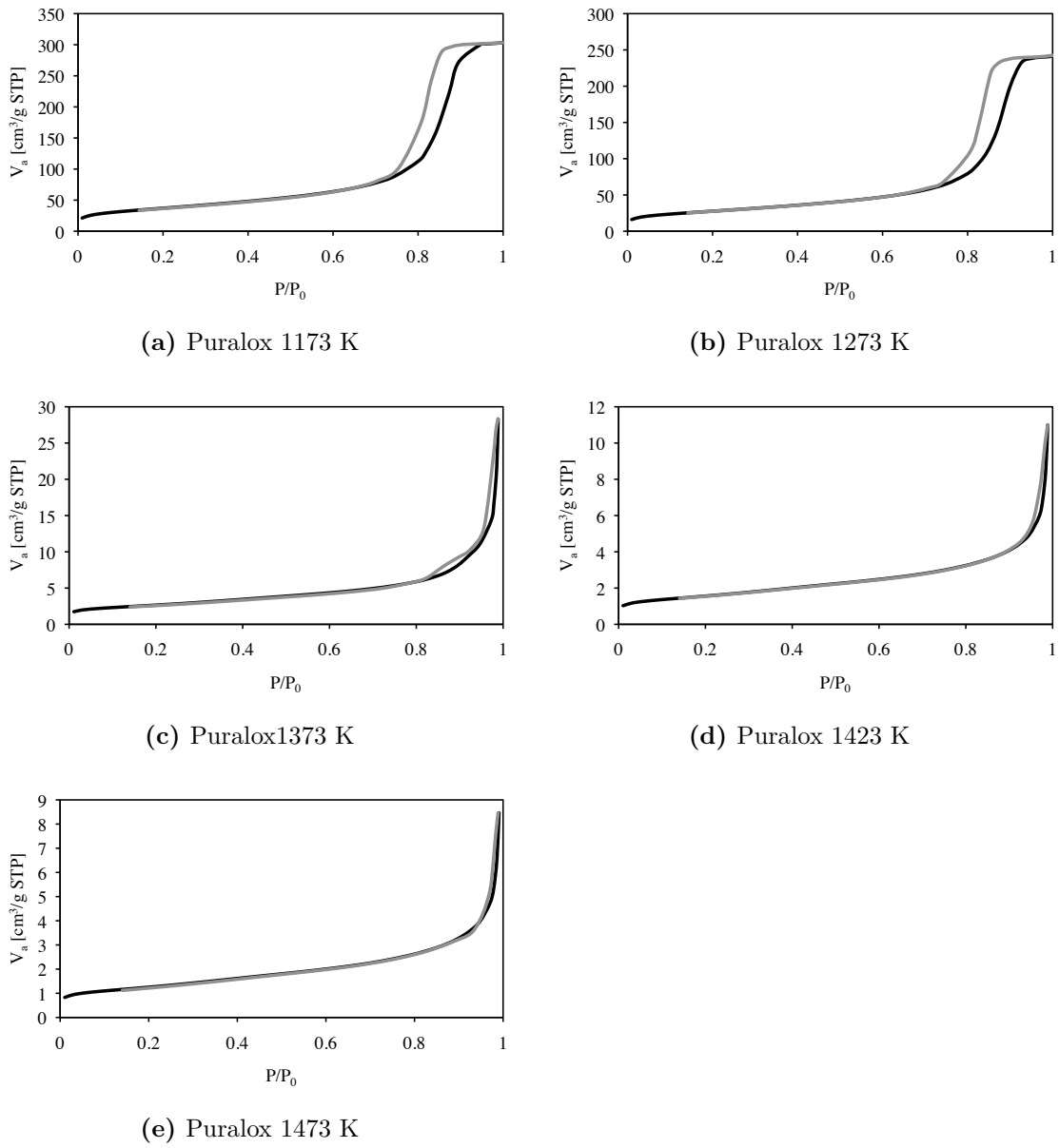
Figure C.2: The N_2 adsorption-desorption isotherms for $CeO_2-Al_2O_3$

BJH desorption dV/dH pore volume

Table C.4: The BJH desorption pore volume and average pore size of CeO$_2$−Al$_2$O$_3$ of two analyses from the same batch (Sep-12)

| T$_{calc.}$ [K] | Pore volume [cm^3/g] | | Pore size [Å] | |
| | CeO$_2$−Al$_2$O$_3$ | | | |
	First	Second	First	Second
1173	0.51	0.52	171	169
1273	0.45	0.43	195	191
1373	0.32	0.33	223	219
1423	0.16	0.17	234	240
1473	0.02	0.02	132	167

Table C.5: The BJH desorption pore volume and average pore size of CeO$_2$−Al$_2$O$_3$ [63] and the Puralox

| T$_{calc.}$ [K] | Pore volume [cm^3/g] | | Pore size [Å] | |
	CeO$_2$−Al$_2$O$_3$	Puralox	CeO$_2$−Al$_2$O$_3$	Puralox
1173	0.36	0.47	101	100
1273	0.30	0.37	123	108
1373	0.15	0.04	146	191
1423	0.06	0.01	214	136
1473	0.01	0.01	195	125

Table C.6: The BJH desorption pore volume and average pore size of Co/CeO$_2$−Al$_2$O$_3$ [63] and CeO$_2$−Al$_2$O$_3$

| T$_{calc.}$ [K] | Pore volume [cm^3/g] | | Pore size [Å] | |
	CeO$_2$−Al$_2$O$_3$	Puralox	CeO$_2$−Al$_2$O$_3$	Puralox
1173	-	0.35	-	119
1273	-	0.29	-	136
1373	0.17	0.17	144	146
1423	-	0.06	-	180
1473	-	0.03	-	244

The BJH desorption pore size distribution graphs for the $CeO_2-Al_2O_3$ calcined at temperatures ranging from 1173 K to 1473 K are shown in Figure C.3.
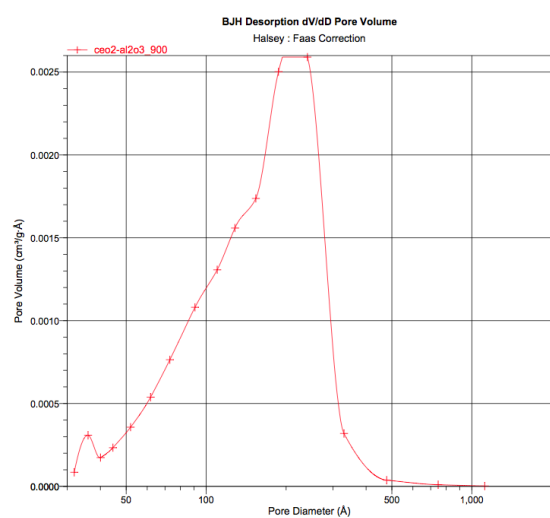
(a) CeO$_2$−Al$_2$O$_3$ 1173 K
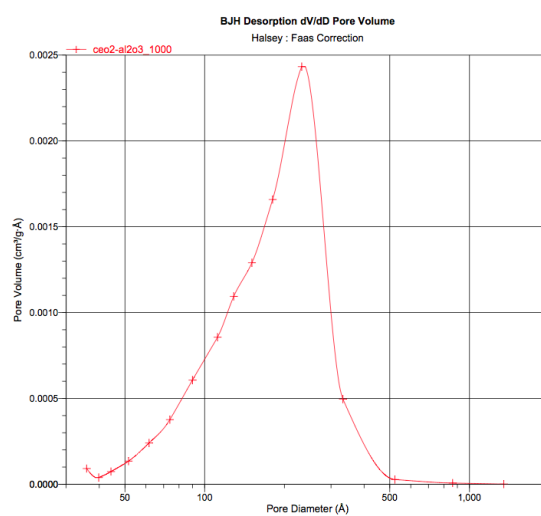
(b) CeO$_2$−Al$_2$O$_3$ 1273 K
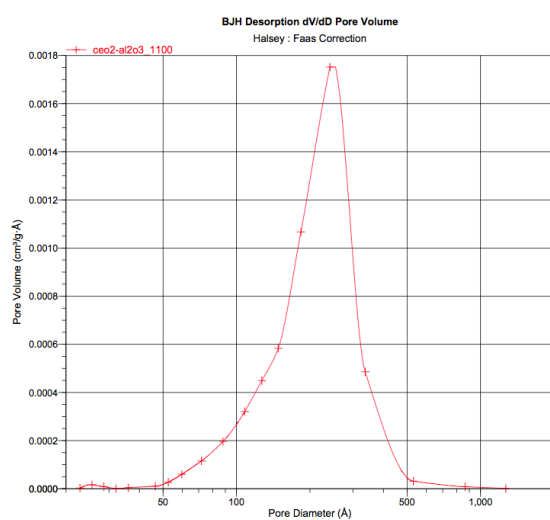
(c) CeO$_2$−Al$_2$O$_3$ 1373 K
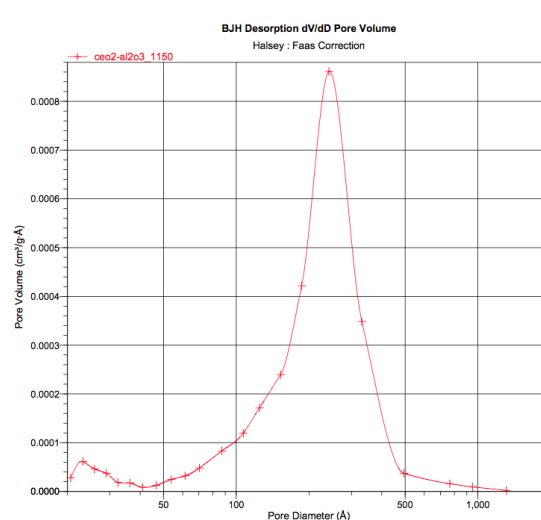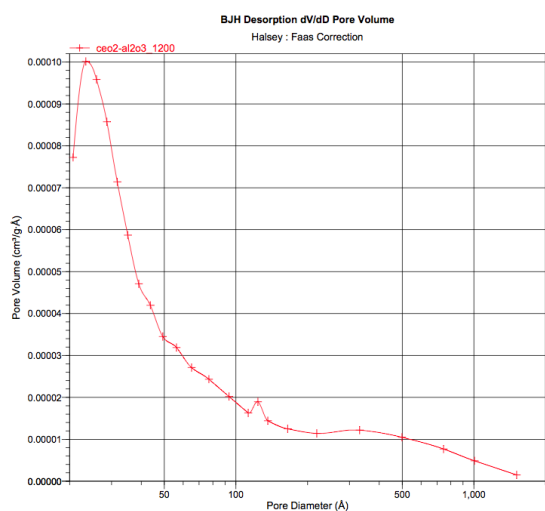
(d) CeO$_2$−Al$_2$O$_3$ 1423 K

(e) CeO$_2$−Al$_2$O$_3$ 1473 K

Figure C.3: The BJH pore size distribution for Puralox calcined at temperatures ranging from 1173 K to 1473 K.

The BJH desorption pore size distribution graphs for Puralox calcined at temperatures ranging from 1173 K to 1473 K are shown in Figure C.4.
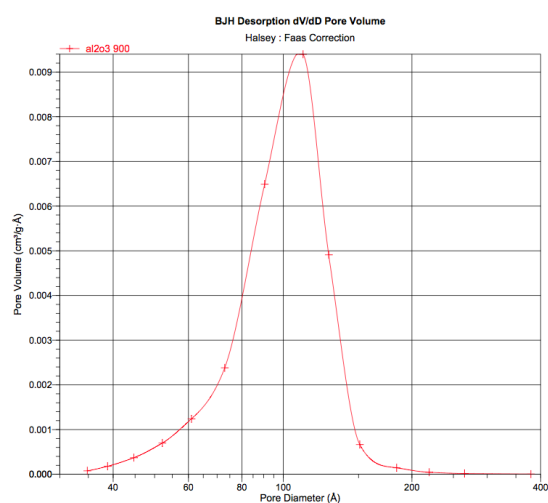
(a) Puralox 1173 K
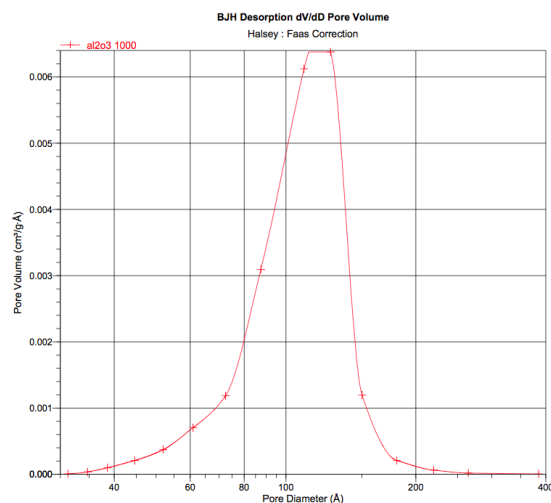
(b) Puralox 1273 K
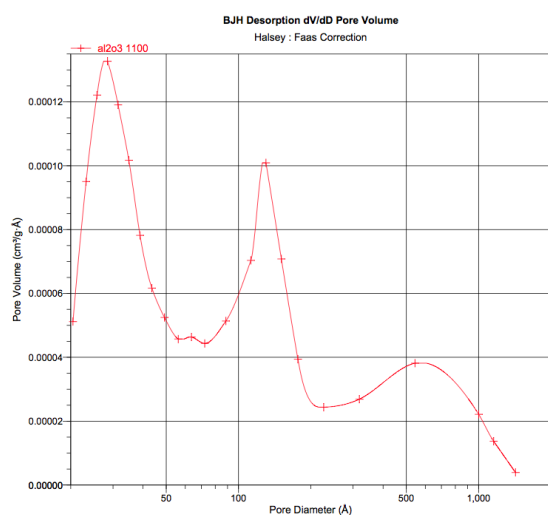
(c) Puralox 1373 K
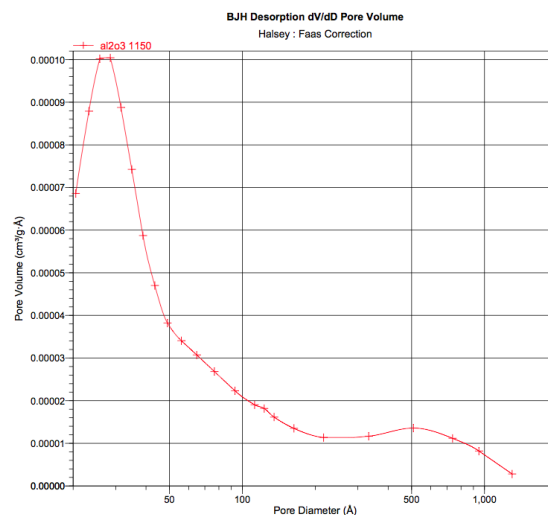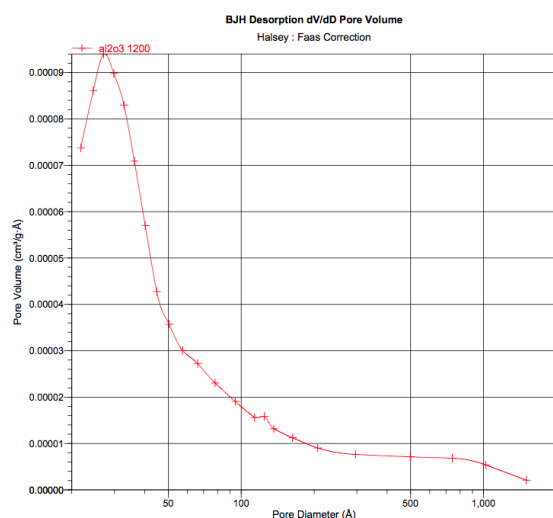
(d) Puralox 1423 K

(e) Puralox 1473 K

Figure C.4: The BJH pore size distribution for Puralox calcined at temperatures ranging from 1173 K to 1473 K.

C.2 X-ray diffraction

The crystallite sizes of CeO_2 and Co_3O_4 were found by using EVA and TOPAS. With the former, one of the peaks is used when calculating the crystallite size, whereas the Rietveld refinement of the whole diffractogram is used in TOPAS.

In Table C.7 the crystallite sizes of CeO_2 from both pure $CeO_2-Al_2O_3$ and $Co/CeO_2-Al_2O_3$ are listed, both from EVA and TOPAS.

Table C.7: Crystallite sizes of at different calcination temperatures

	CeO_2				**Co_3O_4**	
Precursor	$CeO_2-Al_2O_3$		$Co/CeO_2-Al_2O_3$		$Co/CeO_2-Al_2O_3$	
Software	EVA	TOPAS	EVA	TOPAS	EVA	TOPAS
$T_{calc.}$						
1173 K	11.8	13.4	16.9	20.2	6.6	n/a
1273 K	15.6	17.9	24.9	27.8	7.2	n/a
1373 K	24.6	30.4	30.8	38.4	12.8	13.3
1423 K	36.5	47.6	39.6	59.4	20.0	12.9
1473 K	45.6	65.4	47.2	75.1	22.9	17.2

C.3 H$_2$ chemisorption

Table C.8 through C.12 give the results for the chemisorption of Co/CeO$_2$−Al$_2$O$_3$ and the plotted data are shown in Figure C.5 through C.9.

Table C.8: H$_2$ Chemisorption data for Co/CeO$_2$−Al$_2$O$_3$ calcined at 1173 K

First analysis		Second analysis	
P/P$_0$	**V$_a$ [cm^3/g STP]**	**P/P$_0$**	**V$_a$ [cm^3/g STP]**
9.6750	0.7166	10.5698	0.2892
54.1237	0.7963	54.0550	0.3491
106.6903	0.8553	106.6941	0.3942
157.8569	0.9037	156.7932	0.4277
207.0135	0.9411	207.4097	0.4595
257.7961	0.9859	257.0307	0.4865
307.9065	1.0166	307.8053	0.5218
357.6777	1.0635	357.4594	0.5391
407.3768	1.0950	407.4852	0.5784
457.722	1.0213	457.6010	0.6021
517.8861	1.0855	518.0195	0.6231
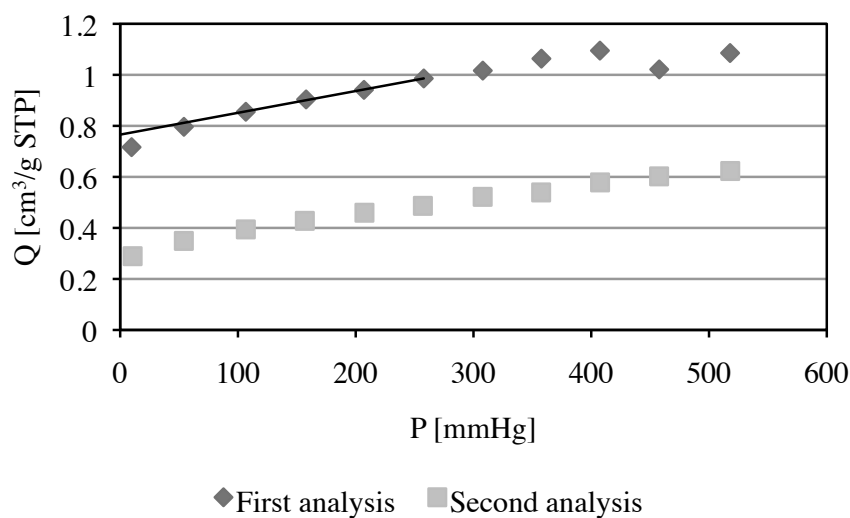
Figure C.5: The adsorption isotherm of H$_2$ chemisorption for Co/CeO$_2$−Al$_2$O$_3$ calcined at 1173 K

Table C.9: H_2 Chemisorption data for $Co/CeO_2-Al_2O_3$ calcined at 1273 K

First analysis		Second analysis	
P/P$_0$	**V$_a$ [cm^3/g STP]**	**P/P$_0$**	**V$_a$ [cm^3/g STP]**
10.3538	0.8038	10.5580	0.2949
54.0313	0.8836	54.5906	0.3533
106.8578	0.9259	106.4421	0.3935
156.3109	0.9665	156.6343	0.4193
206.5588	1.0017	207.2540	0.4488
256.3264	1.0345	257.1314	0.4845
306.7675	1.0771	307.2908	0.5192
356.7166	1.1079	357.2574	0.5652
407.4068	1.1341	407.2942	0.6027
457.0459	1.2228	456.3232	0.6486
517.5375	1.2960	517.6616	0.6997
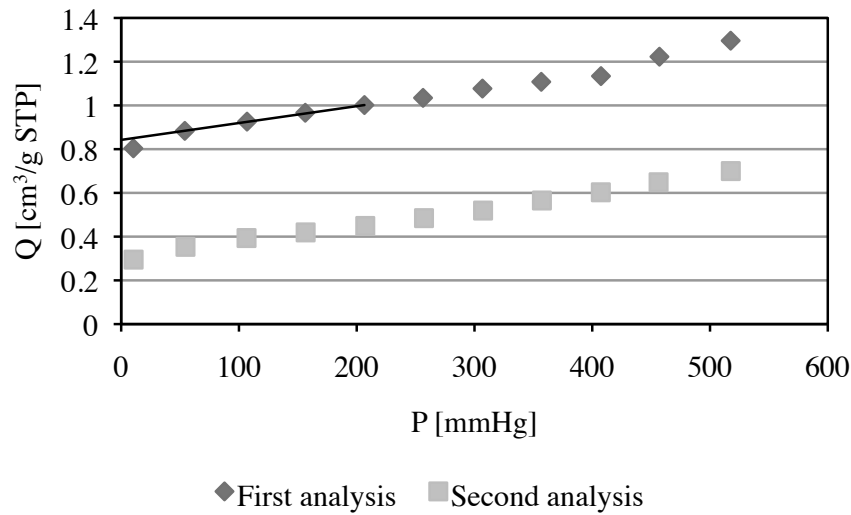
Figure C.6: The adsorption isotherm of H_2 chemisorption for $Co/CeO_2-Al_2O_3$ calcined at 1273 K

Table C.10: H_2 Chemisorption data for $Co/CeO_2-Al_2O_3$ calcined at 1373 K

First analysis		Second analysis	
P/P_0	V_a [cm³/g STP]	P/P_0	V_a [cm³/g STP]
9.5172	0.7943	9.6550	0.2888
55.0464	0.8703	54.7502	0.3503
107.4533	0.9115	107.0788	0.3873
156.6354	0.9256	157.1984	0.4106
207.4255	0.9451	207.9897	0.4282
257.5388	0.9760	257.5368	0.4504
307.1696	1.0208	307.7672	0.4667
357.6861	1.0592	357.5424	0.4825
407.4469	1.0870	407.5204	0.5137
457.4972	1.1144	457.4799	0.5508
517.9102	1.1383	517.8643	0.5850
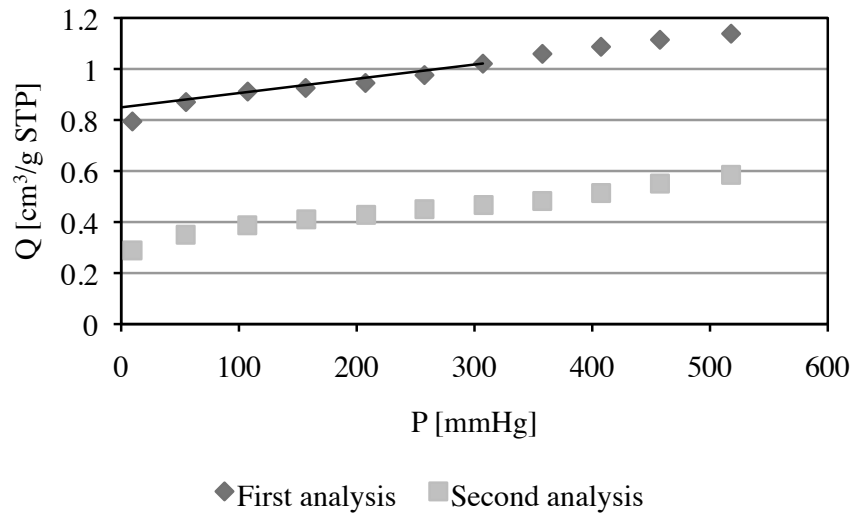
Figure C.7: The adsorption isotherm of H_2 chemisorption for $Co/CeO_2-Al_2O_3$ calcined at 1373 K

Table C.11: H$_2$ Chemisorption data for Co/CeO$_2$−Al$_2$O$_3$ calcined at 1423 K

First analysis		Second analysis	
P/P$_0$	**V$_a$ [cm^3/g STP]**	**P/P$_0$**	**V$_a$ [cm^3/g STP]**
9.9035	0.4730	11.1963	0.1177
55.1918	0.4856	54.9367	0.1288
106.5599	0.4810	106.7342	0.1284
157.1880	0.4631	157.3044	0.1262
207.3917	0.4582	207.3874	0.1239
257.1719	0.4590	257.4606	0.1138
307.4581	0.4631	306.5461	0.1225
356.5165	0.4783	357.3186	0.1326
407.2294	0.4887	407.3521	0.1546
457.2349	0.5098	457.275	0.1674
517.8289	0.5446	517.462	0.1976
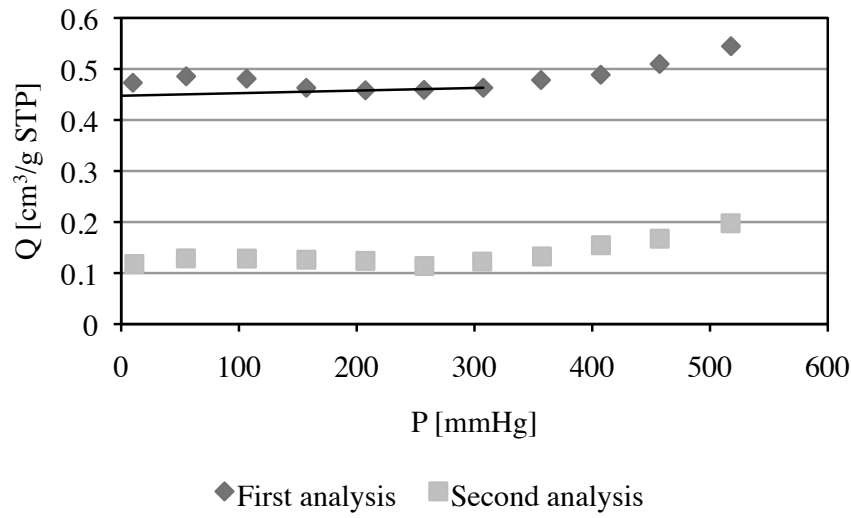
Figure C.8: The adsorption isotherm of H$_2$ chemisorption for Co/CeO$_2$−Al$_2$O$_3$ calcined at 1423 K

Table C.12: H$_2$ Chemisorption data for Co/CeO$_2$−Al$_2$O$_3$ calcined at 1473 K

First analysis		Second analysis	
P/P$_0$	**V$_a$ [cm^3/g STP]**	**P/P$_0$**	**V$_a$ [cm^3/g STP]**
9.5548	0.3241	10.2200	0.0983
55.0482	0.3376	55.2308	0.1145
106.6004	0.3402	106.6445	0.1254
157.7086	0.3440	157.3533	0.1312
207.2371	0.3459	206.9592	0.1402
257.4166	0.3576	257.2630	0.1523
306.6872	0.3689	307.4733	0.1717
357.4034	0.3973	357.4156	0.1983
406.5036	0.4076	406.9850	0.2269
457.4913	0.4484	456.5145	0.2555
517.6219	0.4895	517.9586	0.2895
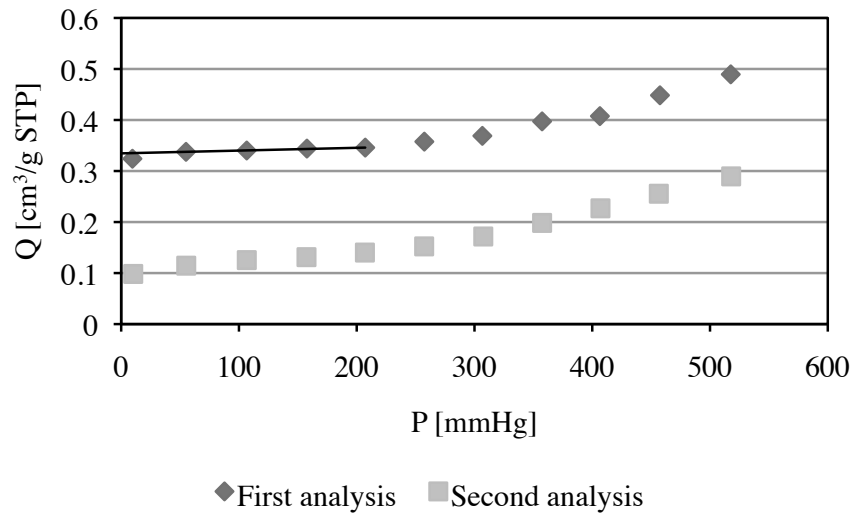
Figure C.9: The adsorption isotherm of H$_2$ chemisorption for Co/CeO$_2$−Al$_2$O$_3$ calcined at 1473 K

Appendix D

Activity testing

D.1 Calibration of the MFC

The calibration of the MFC was done with a soap film meter and provided an overview of the gas velocity over the whole range of openings of the flow controller. In Table D.1 the correlation between the flow, F [L/h], of gas and the percentage opening of the gas tubes for each mass flow controller is listed.

Table D.1: The linear correlations between the percentage opening of the MFC and the flow

MFC #	Gas	F=f(% open) [mL/min]
1	Air	F = 28.141x + 17.3387
2	CH_4	F = 3.077x - 1.2885
3	H_2	F = 0.5676x - 0.7565
4	N_2	F = 5.5796x + 3.5858

The calibration curves are shown in Figure D.1.

(a) 1. Air

(b) 2. CH$_4$

(c) 3. H$_2$

(d) 4. N$_2$
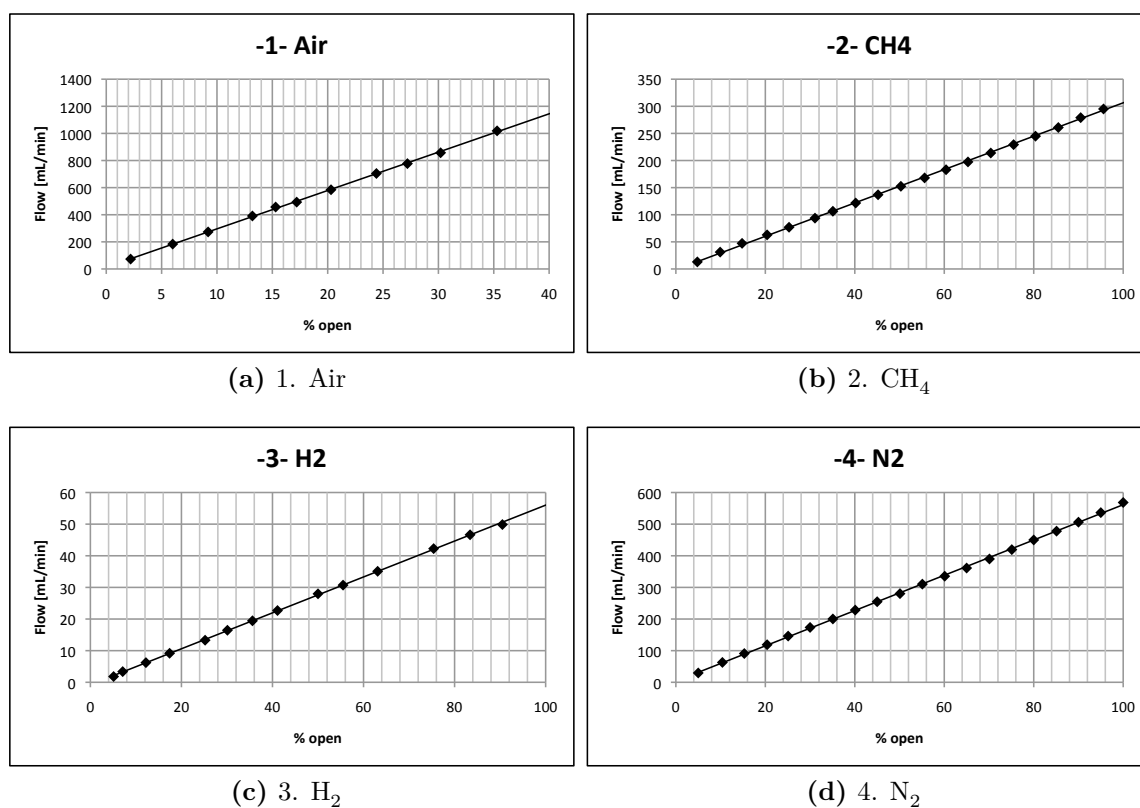
Figure D.1: The calibration curves for the gases used in the set-up

D.2 Calibration of the GC

In Table D.3 the calibration table for the GC is presented.

Table D.2: GC calibration table

RT	Detector	Component	Area	Amount [vol.%]	Response factor
2.024	TCD	H_2	64.2465	722.24	$8.8955\cdot10^{-2}$
3.120	FID	Methane	0.501	409.94	$1.2221\cdot10^{-3}$
3.611	FID	Ethane	0.1015	162.14	$6.2601\cdot10^{-4}$
4.814	FID	Ethylene	0.1023	159.23	$6.4246\cdot10^{-4}$
4.968	TCD	O_2	21	6444.7	$3.2585\cdot10^{-3}$
5.427	TCD	N_2	2.94	1240.9	$2.3692\cdot10^{-3}$
6.190	FID	Propane	0.1035	244.45	$4.2341\cdot10^{-4}$
6.981	TCD	CO	30.8	12651	$2.4346\cdot10^{-3}$
10.003	FID	Propylene	0.1029	241.1	$4.2679\cdot10^{-4}$
10.471	FID	N-Butane	0.152	479.28	$3.1714\cdot10^{-4}$
11.025	TCD	Methane	0.501	157.12	$3.1886\cdot10^{-3}$
12.097	FID	I-Butene	0.1007	305.91	$3.2918\cdot10^{-4}$
12.462	FID	N-Pentane	0.152	600.19	$2.5325\cdot10^{-4}$
13.187	FID	I-Pentane	0.1026	387.19	$2.6499\cdot10^{-4}$
14.240	TCD	CO_2	0.495	229.33	$2.1585\cdot10^{-3}$
14.472	FID	N-Hexane	0.1	450.94	$2.2176\cdot10^{-4}$

The temperature program used during analysis is given in Table D.3 and a draft is given in Figure D.2.

Table D.3: GC temperature program.

Ramp [°C/min]	T [°C]	t [min]
	50	6.80
85	83	0.39
	83	2.00
80	115	0.40
53	180	1.23
	180	5.50
Cool down	50	6.69
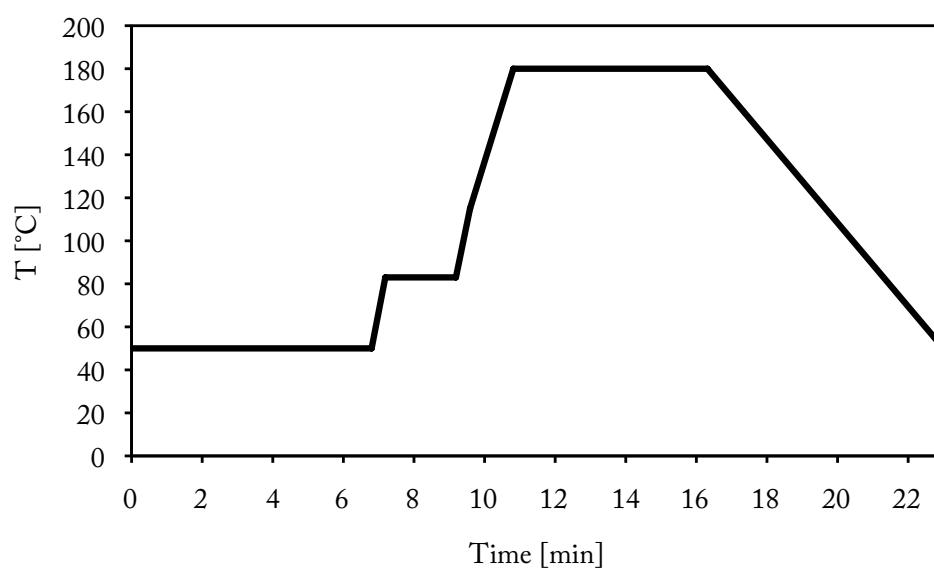
Figure D.2: A schematic illustration of the temperature program used in the GC analysis.

D.3 Experimental conditions

Table D.4: An overview over the experimental conditions during catalytic partial oxidation of methane

Exp.	Catalyst T_{calc}	Reduction	GHSV $[L_{CH_4}/g_{cat}\cdot h]$	$T_{furnace}$ [K]
1	1273 K	973 K, 10 K/min, 2h	75	573/798/1023
2	1273 K	973 K, 10 K/min, 2h	75	923/1023
3	1173 K	973 K, 10 K/min, 2h	75	623/773/923
4	1473 K	973 K, 10 K/min, 2h	75	673/823/923
5	1373 K	973 K, 10 K/min, 2h	75	923
6	1273 K	973 K, 10 K/min, 2h	75	923/1023/1123
7	1173 K	973 K, 10 K/min, 2h	75	923/1023/1123
8	1273 K	973 K, 10 K/min, 2h	75	923/1023/1123
9	1273 K	No	75	923/1023
11	1423 K	973 K, 10 K/min, 2h	75	923/1023/1123
12	1373 K	973 K, 10 K/min, 2h	75	923/1023/1123
13	1473 K	973 K, 10 K/min, 2h	75	923/1023/1123
14	1273 K	No	250	923/1023/1123
15	1273 K	No	500	923/1023/1123/1023
16	1273 K	No	400	1023
17	1273 K	973 K, 10 K/min, 2h	150/250/350/ 400/450/250	1023
18	Monolith	973 K, 10 K/min, 2h	8000 [h^{-1}]	1023
19	1273 K	973 K, 10 K/min, 2h	75	1023

D.4   Experimental results

Experiment 7

Catalyst: $Co/CeO_2-Al_2O_3$ (1173 K)
$m_{catalyst} = 0.1016$ g
$GHSV = 75$ $L_{CH_4}/g_{cat}\cdot h$
Reduction: 50 mL/min 50 vol.% H_2 in N_2, 10 K/min, 973 K, 2h

Table D.5: Exp. 7. Feed gas

Compound	V	y	F
	[mL/min (STP)]	[-]	[mmol/s]
CH_4	127.0	0.2958	0.0874
O_2	63.5	0.1479	0.0437
N_2	236.2	0.5500	0.1626
Total	429.4	1.0000	0.2956

Table D.6: Exp. 7. Product data, $T_{furnace} = 923$ K

Compound	y_{GC}	y_{GC}	$y_{norm.}$	F	X	S	Y
	[vol.%]	[-]	[-]	[mmol/s]	[%]	[%]	[%]
CH_4 (FID)	6.2668						
H_2	26.4901			0.1031		81.6	59.0
N_2	43.4140	0.4341	0.6593	0.1626			
CO	14.7596	0.1476	0.2241	0.0553		92.5	
CH_4 (TCD)	6.4840	0.0648	0.0985	0.0243	71.1		
CO_2	1.1956	0.0120	0.0182	0.0045		7.5	
H_2O				0.0232		18.4	
F_{H_2}/F_{CO}	1.9						
F_{H_2O}/F_{CO_2}	5.2						
ε_C	3.9						

Table D.7: Exp. 7. Product data, $T_{furnace} = 1023$ K

Compound	y_{GC} [vol.%]	y_{GC} [-]	$y_{norm.}$ [-]	F [mmol/s]	X [%]	S [%]	Y [%]
CH_4 (FID)	4.4867	0.0449					
H_2	29.4058	0.2941		0.1196		86.1	68.4078
N_2	41.8423	0.4184	0.6584	0.1626			
CO	16.6102	0.1661	0.2614	0.0645		97.3	
CH_4 (TCD)	4.6314	0.0463	0.0729	0.0180	78.7		
CO_2	0.4684	0.0047	0.0074	0.0018		2.7	
H_2O				0.0193		13.9	
F_{H_2}/F_{CO}	1.9						
F_{H_2O}/F_{CO_2}	10.6						
ε_C	3.5						

Table D.8: Exp. 7. Product data, $T_{furnace} = 1123$ K

Compound	y_{GC} [vol.%]	y_{GC} [-]	$y_{norm.}$ [-]	F [mmol/s]	X [%]	S [%]	Y [%]
CH_4 (FID)	3.4414	0.0344					
H_2	31.3216	0.3132		0.1301		88.7	74.4
N_2	41.0886	0.4109	0.6580	0.1626			
CO	17.6576	0.1766	0.2828	0.0699		99.3	
CH_4 (TCD)	3.5694	0.0357	0.0572	0.0141	83.3		
CO_2	0.1255	0.0013	0.0020	0.0005		0.7	
H_2O				0.0166		11.3	
F_{H_2}/F_{CO}	1.9						
F_{H_2O}/F_{CO_2}	33.4						
ε_C	3.4						

Table D.9: Exp. 7. Temperature data

$d_{\text{bed entrance}}$ [cm]	T [°C]	$d_{\text{bed entrance}}$ [cm]	T [°C]	$d_{\text{bed entrance}}$ [cm]	T [°C]
$\mathbf{T_{\text{furnace}}} = 650$ °C		$\mathbf{T_{\text{furnace}}} = 750$ °C		$\mathbf{T_{\text{furnace}}} = 850$ °C	
-4.8	676.0	-5.8	771.9	-5.8	869.8
-4.3	678.0	-5.3	773.0	-5.3	871.4
-3.8	678.8	-4.8	774.0	-4.8	872.5
-3.3	679.0	-4.3	775.0	-4.3	874.0
-2.8	679.8	-3.8	776.0	-3.8	875.2
-2.3	680.3	-3.3	777.0	-3.3	876.0
-1.8	681.3	-2.8	777.5	-2.8	876.3
-1.3	685.0	-2.3	778.2	-2.3	876.6
-0.8	692.6	-1.8	779.0	-1.8	877.2
-0.6	699.0	-1.3	780.5	-1.3	877.0
-0.5	706.0	-0.8	784.0	-0.8	877.0
-0.3	716.8	-0.6	786.4	-0.6	877.8
-0.1	725.5	-0.3	792.4	-0.3	878.6
0.0	728.2	-0.1	796.0	-0.1	875.4
0.2	718.2	0.1	790.0	0.2	862.0
0.3	708.6	0.5	771.0	0.3	854.0
0.4	703.2	0.7	766.5	0.4	851.5
0.5	693.4	1.2	764.8	0.5	849.5
0.7	688.2	1.7	763.7	0.6	849.0
1.2	674.7	2.2	760.7	0.7	851.5
1.7	670.7	2.7	758.0	0.9	854.0
2.2	664.8	3.2	755.5	1.2	857.4
2.7	661.3	3.7	751.5	1.7	860.0
3.2	657.6	4.2	748.3	2.2	859.0
				2.7	857.0
				3.2	854.0
				4.2	850.0

Experiment 8

Catalyst: $Co/CeO_2-Al_2O_3$ (1273 K)
$m_{\text{catalyst}} = 0.0990$ g
GHSV = 75 $L_{CH_4}/g_{\text{cat}} \cdot$h
Reduction: 50 mL/min 50 vol.% H_2 in N_2, 10 K/min, 973 K, 2h

Table D.10: Exp. 8. Feed gas

Compound	V	y	F
	[mL/min (STP)]	[-]	[mmol/s]
CH$_4$	123.8	0.2958	0.0852
O$_2$	61.9	0.1479	0.0426
N$_2$	230.1	0.5500	0.1584
Total	418.4	1.0000	0.2881

Table D.11: Exp. 8. Product data, T$_{furnace}$ = 923 K

Compound	y$_{GC}$	y$_{GC}$	y$_{norm.}$	F	X	S	Y
	[vol.%]	[-]	[-]	[mmol/s]	[%]	[%]	[%]
CH$_4$ (FID)	5.8532	0.0585					
H$_2$	26.8539	0.2685		0.1036		82.7	60.8
N$_2$	42.5829	0.4258	0.6589	0.1584			
CO	14.9109	0.1491	0.2307	0.0555		93.3	
CH$_4$ (TCD)	6.0558	0.0606	0.0937	0.0225	72.5		
CO$_2$	1.0761	0.0108	0.0167	0.0040		6.7	
H$_2$O				0.0217		17.3	
F$_{H_2}$/F$_{CO}$	1.9						
F$_{H_2O}$/F$_{CO_2}$	5.4						
ε_C	3.7						

Table D.12: Exp. 8. Product data, T$_{furnace}$ = 1023 K

Compound	y$_{GC}$	y$_{GC}$	y$_{norm.}$	F	X	S	Y
	[vol.%]	[-]	[-]	[mmol/s]	[%]	[%]	[%]
CH$_4$ (FID)	4.1392	0.0414					
H$_2$	30.0136	0.3001		0.1197		87.0	70.2
N$_2$	41.4887	0.4149	0.6582	0.1584			
CO	16.8765	0.1688	0.2677	0.0644		97.8	
CH$_4$ (TCD)	4.2971	0.0430	0.0682	0.0164	80.1		
CO$_2$	0.3735	0.0037	0.0059	0.0014		2.2	
H$_2$O				0.0179		13.0	
F$_{H_2}$/F$_{CO}$	1.9						
F$_{H_2O}$/F$_{CO_2}$	12.6						
ε_C	3.4						

Table D.13: Exp. 8. Product data, $T_{furnace} = 1123$ K

Compound	y_{GC} [vol.%]	y_{GC} [-]	$y_{norm.}$ [-]	F [mmol/s]	X [%]	S [%]	Y [%]
CH_4 (FID)	3.2316						
H_2	31.7275			0.1289		89.3	75.6
N_2	40.7684		0.6577	0.1584			
CO	17.8063		0.2873	0.0692		99.6	
CH_4 (TCD)	3.3484		0.0540	0.0130	84.2		
CO_2	0.0630		0.0010	0.0002		0.4	
H_2O				0.0155		10.7	
F_{H_2}/F_{CO}	1.9						
F_{H_2O}/F_{CO_2}	63.3						
ε_C	3.2						

Table D.14: Exp. 8. Temperature data

$T_{furnace} = 650$ °C		$T_{furnace} = 750$ °C		$T_{furnace} = 850$ °C	
$d_{bed\ entrance}$ [cm]	T [°C]	$d_{bed\ entrance}$ [cm]	T [°C]	$d_{bed\ entrance}$ [cm]	T [°C]
-3.4	664.0	-3.4	760.0	-3.4	856.7
-2.9	665.0	-2.9	761.5	-2.9	858.2
-2.4	666.5	-2.4	762.8	-2.4	859.8
-1.9	668.3	-1.9	764.0	-1.9	860.4
-1.4	671.3	-1.4	765.0	-1.4	861.2
-0.9	678.5	-0.9	767.5	-0.9	862.2
-0.7	689.3	-0.4	779.0	-0.6	863.7
-0.4	703.5	-0.2	786.0	-0.4	866.0
-0.3	706.5	-0.1	788.5	-0.3	867.0
-0.1	719.0	0.0	790.3	-0.1	868.0
0.0	726.0	0.1	786.5	0.0	866.0
0.1	729.0	0.2	782.3	0.1	862.0
0.3	707.2	0.3	770.2	0.2	858.0
0.6	690.0	0.5	767.0	0.4	846.0
1.1	673.4	0.6	766.0	0.5	847.0
1.6	668.0	1.1	760.7	0.6	848.0
2.1	665.0	1.6	760.2	1.1	852.8
2.6	661.6	2.1	759.0	1.6	855.9
3.1	659.0	2.6	757.5	2.1	855.6
3.6	657.0	3.1	755.5	2.6	855.0
4.1	654.3	3.6	754.0	3.1	854.3
4.6	651.5	4.1	751.5	3.6	852.0
		4.6	750.0	4.1	850.0

Experiment 11

Catalyst: $Co/CeO_2-Al_2O_3$ (1423 K)
$m_{catalyst} = 0.0948$ g
$GHSV = 75$ $L_{CH_4}/g_{cat} \cdot h$
Reduction: 50 mL/min 50 vol.% H_2 in N_2, 10 K/min, 973 K, 2h

Table D.15: Exp 11. Feed gas

Compound	V	y	F
	[mL/min (STP)]	[-]	[mmol/s]
CH_4	118.5	0.2958	0.0816
O_2	59.3	0.1479	0.0408
N_2	220.4	0.5500	0.1517
Total	400.6	1.0000	0.2758

Table D.16: Exp. 11. Product data, $T_{furnace} = 923$ K

Compound	y_{GC}	y_{GC}	$y_{norm.}$	F	X	S	Y
	[vol.%]	[-]	[-]	[mmol/s]	[%]	[%]	[%]
CH_4 (FID)	7.1244	0.0712					
H_2	24.4586	0.2446		0.0889		79.1	54.5
N_2	43.9491	0.4395	0.6610	0.1517			
CO	13.5938	0.1359	0.2044	0.0469		89.4	
CH_4 (TCD)	7.3408	0.0734	0.1104	0.0253	67.4		
CO_2	1.6082	0.0161	0.0242	0.0056		10.6	
H_2O				0.0236		20.9	
F_{H_2}/F_{CO}	1.9						
F_{H_2O}/F_{CO_2}	4.2						
ε_C	4.6						

Table D.17: Exp. 11. Product data, $T_{furnace} = 1023$ K

Compound	y_{GC}	y_{GC}	$y_{norm.}$	F	X	S	Y
	[vol.%]	[-]	[-]	[mmol/s]	[%]	[%]	[%]
CH_4 (FID)	4.8543	0.0485					
H_2	28.4612	0.2846		0.1081		85.0	66.3
N_2	42.4264	0.4243	0.6599	0.1517			
CO	16.1667	0.1617	0.2515	0.0578		96.1	
CH_4 (TCD)	5.0345	0.0503	0.0783	0.0180	77.0		
CO_2	0.6610	0.0066	0.0103	0.0024		3.9	
H_2O				0.0190		15.0	
F_{H_2}/F_{CO}	1.9						
F_{H_2O}/F_{CO_2}	8.1						
ε_C	4.2						

Table D.18: Exp. 11. Product data, $T_{furnace}$ = 1123 K

Compound	y_{GC} [vol.%]	y_{GC} [-]	$y_{norm.}$ [-]	F [mmol/s]	X [%]	S [%]	Y [%]
CH_4 (FID)	3.7521						
H_2	30.5797			0.1185		87.8	72.6
N_2	41.7166		0.6595	0.1517			
CO	17.4012		0.2751	0.0633		98.6	
CH_4 (TCD)	3.8813		0.0614	0.0141	82.0		
CO_2	0.2543		0.0040	0.0009		1.4	
H_2O				0.0165		12.2	
F_{H_2}/F_{CO}	1.9						
F_{H_2O}/F_{CO_2}	17.8						
ε_C	4.0						

Table D.19: Exp. 11. Temperature data

$T_{furnace}$ = 650 °C		$T_{furnace}$ = 750 °C		$T_{furnace}$ = 850 °C	
$d_{bed\ entrance}$ [cm]	T [°C]	$d_{bed\ entrance}$ [cm]	T [°C]	$d_{bed\ entrance}$ [cm]	T [°C]
-3.9	666.0	-3.9	766.5	-3.9	868.9
-3.4	667.3	-3.4	767.5	-3.4	869.8
-2.9	668.0	-2.9	768.2	-2.9	870.0
-2.4	669.0	-2.4	769.0	-2.4	870.0
-1.9	670.0	-1.9	769.5	-1.9	870.0
-1.4	673.3	-1.4	770.2	-1.4	869.4
-0.9	679.9	-0.9	772.5	-0.9	869.0
-0.5	688.0	-0.5	775.5	-0.5	867.6
-0.4	693.8	-0.4	778.0	-0.4	865.5
-0.2	706.5	-0.2	779.9	0.0	851.5
0.0	713.3	0.0	778.5	0.2	846.5
0.2	713.0	0.2	773.0	0.5	827.0
0.5	690.0	0.5	759.0	0.7	833.5
0.7	683.4	0.7	757.5	1.2	848.8
1.2	672.3	1.0	758.6	1.7	854.3
1.7	667.5	1.2	759.0	2.2	855.0
2.2	665.2	1.7	759.0	2.7	855.0
2.7	663.0	2.2	759.0		
3.2	660.8	3.2	757.5		
4.2	656.0				

Experiment 12

Catalyst: $Co/CeO_2-Al_2O_3$ (1373 K)
$m_{catalyst} = 0.0959$ g
GHSV = 75 $L_{CH_4}/g_{cat}\cdot$h
Reduction: 50 mL/min 50 vol.% H_2 in N_2, 10 K/min, 973 K, 2h

Table D.20: Exp. 12. Feed gas

Compound	V	y	F
	[mL/min (STP)]	[-]	[mmol/s]
CH_4	119.9	0.2958	0.0825
O_2	59.9	0.1479	0.0413
N_2	222.9	0.5500	0.1535
Total	405.3	1.0000	0.2790

Table D.21: Exp. 12. Product data, $T_{furnace} = 923$ K

Compound	y_{GC}	y_{GC}	$y_{norm.}$	F	X	S	Y
	[vol.%]	[-]	[-]	[mmol/s]	[%]	[%]	[%]
CH_4 (FID)	12.9794	0.1298					
H_2	26.8429	0.2684		0.1001		82.4	60.7
N_2	43.8678	0.4387	0.6600	0.1535			
CO	15.2555	0.1526	0.2295	0.0534		93.2	
CH_4 (TCD)	6.2280	0.0623	0.0937	0.0218	72.4		
CO_2	1.1174	0.0112	0.0168	0.0039		6.8	
H_2O				0.0213		17.6	
F_{H_2}/F_{CO}	1.9						
F_{H_2O}/F_{CO_2}	5.5						
ε_C	4.2						

Table D.22: Exp. 12. Product data, $T_{furnace} = 1023$ K

Compound	y_{GC}	y_{GC}	$y_{norm.}$	F	X	S	Y
	[vol.%]	[-]	[-]	[mmol/s]	[%]	[%]	[%]
CH_4 (FID)	4.0186	0.0402					
H_2	30.1648	0.3016		0.1176		87.3	71.2
N_2	42.2746	0.4227	0.6589	0.1535			
CO	17.3658	0.1737	0.2707	0.0630		98.2	
CH_4 (TCD)	4.1870	0.0419	0.0653	0.0152	80.9		
CO_2	0.3272	0.0033	0.0051	0.0012		1.8	
H_2O				0.0171		12.7	
F_{H_2}/F_{CO}	1.9						
F_{H_2O}/F_{CO_2}	14.4						
ε_C	3.8						

Table D.23: Exp. 12. Product data, $T_{furnace} = 1123$ K

Compound	y_{GC} [vol.%]	y_{GC} [-]	$y_{norm.}$ [-]	F [mmol/s]	X [%]	S [%]	Y [%]
CH_4 (FID)	3.1549	0.0315					
H_2	31.7625	0.3176		0.1259		89.4	76.3
N_2	41.6465	0.4165	0.6587	0.1535			
CO	18.2467	0.1825	0.2886	0.0672		99.7	
CH_4 (TCD)	3.2891	0.0329	0.0520	0.0121	84.8		
CO_2	0.0476	0.0005	0.0008	0.0002		0.3	
H_2O				0.0149		10.6	
F_{H_2}/F_{CO}	1.9						
F_{H_2O}/F_{CO_2}	85.1						
ε_C	3.6						

Table D.24: Exp. 12. Temperature data

$T_{furnace} = 650$ °C		$T_{furnace} = 750$ °C		$T_{furnace} = 850$ °C	
$d_{bed\ entrance}$ [cm]	T [°C]	$d_{bed\ entrance}$ [cm]	T [°C]	$d_{bed\ entrance}$ [cm]	T [°C]
-3.7	660.7	-3.7	765.5	-3.7	868.4
-3.2	662.4	-3.2	767.0	-3.2	870.0
-2.7	664.0	-2.7	768.8	-2.7	871.4
-2.2	665.5	-2.2	769.7	-2.2	872.5
-1.7	667.5	-1.7	771.2	-1.7	873.8
-1.2	671.2	-1.2	773.3	-1.2	874.9
-1.0	675.0	-0.7	777.9	-1.0	875.9
-0.7	682.0	-0.5	781.5	-0.7	877.3
-0.5	688.9	-0.4	786.0	-0.5	879.6
-0.3	699.8	-0.3	789.0	-0.3	881.2
-0.2	707.5	-0.2	790.5	-0.2	882.9
-0.1	714.0	-0.1	793.8	-0.1	883.8
0.0	720.8	0.0	796.2	0.1	884.0
0.1	724.0	0.2	795.4	0.3	872.5
0.2	722.0	0.3	790.0	0.4	867.5
0.3	716.0	0.5	779.5	0.8	868.0
0.8	684.7	0.8	773.5	1.3	870.0
1.3	673.5	1.3	770.8	1.8	871.0
1.8	668.4	1.8	769.4	2.3	870.9
2.3	664.7	2.3	768.0	3.3	868.0
2.8	662.0	2.8	766.0		
3.3	659.3	3.3	765.0		

Experiment 13

Catalyst: $Co/CeO_2-Al_2O_3$ (1473 K)
$m_{catalyst} = 0.0953$ g
GHSV = 75 $L_{CH_4}/g_{cat}\cdot$h
Reduction: 50 mL/min 50 vol.% H_2 in N_2, 10 K/min, 973 K, 2h

Table D.25: Exp. 13. Feed gas

Compound	V	y	F
	[mL/min (STP)]	[-]	[mmol/s]
CH_4	119.1	0.2958	0.0820
O_2	59.6	0.1479	0.0410
N_2	221.5	0.5500	0.1525
Total	402.8	1.0000	0.2773

Table D.26: Exp. 13. Product data, $T_{furnace}$ = 923 K

Compound	y_{GC}	y_{GC}	$y_{norm.}$	F	X	S	Y
	[vol.%]	[-]	[-]	[mol/s]	[%]	[%]	[%]
CH_4 (FID)	8.2222	0.0822					
H_2	22.8772	0.2288		0.0806		75.7	49.1
N_2	45.1510	0.4515	0.6598	0.1525			
CO	12.8968	0.1290	0.1885	0.0436		87.4	
CH_4 (TCD)	8.5200	0.0852	0.1245	0.0288	63.4		
CO_2	1.8633	0.0186	0.0272	0.0063		12.6	
H_2O				0.0259		24.3	
F_{H_2}/F_{CO}	1.9						
F_{H_2O}/F_{CO_2}	4.1						
ε_C	4.1						

Table D.27: Exp. 13. Product data, $T_{furnace}$ = 1023 K

Compound	y_{GC}	y_{GC}	$y_{norm.}$	F	X	S	Y
	[vol.%]	[-]	[-]	[mmol/s]	[%]	[%]	[%]
CH_4 (FID)	5.9001	0.0590					
H_2	26.6775	0.2668		0.0995		82.2	60.7
N_2	43.4655	0.4347	0.6596	0.1525			
CO	15.4121	0.1541	0.2339	0.0541		94.5	
CH_4 (TCD)	6.1133	0.0611	0.0928	0.0215	72.7		
CO_2	0.9047	0.0090	0.0137	0.0032		5.5	
H_2O				0.0216		17.8	
F_{H_2}/F_{CO}	1.8						
F_{H_2O}/F_{CO_2}	6.8						
ε_C	4.0						

Table D.28: Exp. 13. Product data, $T_{furnace} = 1123$ K

Compound	y_{GC} [vol.%]	y_{GC} [-]	$y_{norm.}$ [-]	F [mmol/s]	X [%]	S [%]	Y [%]
CH_4 (FID)	5.4248	0.0542					
H_2	27.6745	0.2767		0.1036		83.3	63.2
N_2	43.3825	0.4338	0.6592	0.1525			
CO	16.1483	0.1615	0.2454	0.0568		96.2	
CH_4 (TCD)	5.6418	0.0564	0.0857	0.0198	74.8		
CO_2	0.6413	0.0064	0.0097	0.0023		3.8	
H_2O				0.0207		16.7	
F_{H_2}/F_{CO}	1.8						
F_{H_2O}/F_{CO_2}	9.2						
ε_C	3.9						

Table D.29: Exp. 13. Temperature data

$T_{furnace} = 650$ °C		$T_{furnace} = 750$ °C		$T_{furnace} = 850$ °C	
$d_{bed\ entrance}$ [cm]	T [°C]	$d_{bed\ entrance}$ [cm]	T [°C]	$d_{bed\ entrance}$ [cm]	T [°C]
-3.8	665.7	-3.8	773.0	-3.8	878.6
-3.3	667.2	-3.3	774.5	-3.3	880.6
-2.8	669.2	-2.8	776.0	-2.8	882.7
-2.3	670.5	-2.3	777.0	-2.3	883.3
-1.8	671.5	-1.8	777.2	-1.8	882.7
-1.3	674.5	-1.3	777.7	-1.3	881.5
-1.1	677.5	-1.1	778.5	-1.1	881.3
-0.8	682.0	-0.8	780.3	-0.8	880.6
-0.5	694.0	-0.3	788.0	-0.5	880.5
-0.3	700.0	-0.2	789.8	-0.3	880.6
-0.2	710.5	-0.1	793.0	-0.1	879.1
-0.1	716.8	0	793.2	0	874.3
0	720.3	0.1	792.0	0.1	872.5
0.1	721.3	0.2	787.0	0.2	867.0
0.2	716.5	0.3	779.3	0.3	862.5
0.3	708.5	0.5	772.0	0.4	858.0
0.5	692.8	0.7	769.3	0.5	857.0
0.7	682.3	1.2	767.0	0.7	860.3
1.2	670.5	1.7	765.3	1.2	866.8
1.7	664.5	2.2	763.2	1.7	867.9
2.2	660.5	3.2	758.3	2.2	866.9
3.2	652.0			2.7	866.1
				3.2	864.0

Experiment 17

Catalyst: $Co/CeO_2-Al_2O_3$ (1273 K)
$m_{catalyst} = 0.0196$ g
Reduction: 50 mL/min 50 vol.% H_2 in N_2, 10 K/min, 973 K, 2h
$T_{furnace} = 1023$ K

Table D.30: Exp. 17. Feed data, GHSV = 150 $L_{CH_4}/g_{cat}\cdot$h

Compound	V	y	F
	[mL/min (STP)]	[-]	[mmol/s]
CH_4	49.0	0.2958	0.0337
O_2	24.5	0.1479	0.0169
N_2	91.1	0.5500	0.0627
Total	165.7	1.0000	0.1141

Table D.31: Exp. 17. Product data, GHSV = 150 $L_{CH_4}/g_{cat}\cdot$h, TOS = 17 min. Analysis 1

Compound	y_{GC}	y_{GC}	$y_{norm.}$	F	X	S	Y
	[vol.%]	[-]	[-]	[mmol/s]	[%]	[%]	[%]
CH_4 (FID)	4.1461	0.0415					
H_2	29.2200	0.2922		0.0468		85.9	69.3
N_2	41.4382	0.4144	0.6624	0.0627			
CO	16.4640	0.1646	0.2632	0.0249		97.8	
CH_4 (TCD)	4.2905	0.0429	0.0686	0.0065	79.7		
CO_2	0.3694	0.0037	0.0059	0.0006		2.2	
H_2O				0.0077		14.1	
F_{H_2}/F_{CO}	1.9						
F_{H_2O}/F_{CO_2}	13.8						
ε_C	5.2						

Table D.32: Exp. 17. Product data, GHSV = 150 L$_{CH_4}$/g$_{cat}$·h, TOS = 40 min. Analysis 2

Compound	y$_{GC}$ [vol.%]	y$_{GC}$ [-]	y$_{norm.}$ [-]	F [mmol/s]	X [%]	S [%]	Y [%]
CH$_4$ (FID)	4.29878	0.0430					
H$_2$	28.74706	0.2875		0.0461		85.4	69.3
N$_2$	41.37285	0.4137	0.6623	0.0627			
CO	16.23832	0.1624	0.2600	0.0246		97.6	
CH$_4$ (TCD)	4.44821	0.0445	0.0712	0.0067	78.9		
CO$_2$	0.40681	0.0041	0.0065	0.0006		2.4	
H$_2$O				0.0079		14.6	
F$_{H_2}$/F$_{CO}$	1.9						
F$_{H_2O}$/F$_{CO_2}$	12.8						
ε_C	5.2						

Table D.33: Exp. 17. Product data, GHSV = 150 L$_{CH_4}$/g$_{cat}$·h, TOS = 64 min. Analysis 3

Compound	y$_{GC}$ [vol.%]	y$_{GC}$ [-]	y$_{norm.}$ [-]	F [mmol/s]	X [%]	S [%]	Y [%]
CH$_4$ (FID)	4.53540	0.0454					
H$_2$	28.35036	0.2835		0.0454		85.1	67.3
N$_2$	41.49611	0.4150	0.6615	0.0627			
CO	16.07491	0.1607	0.2563	0.0243		97.0	
CH$_4$ (TCD)	4.66516	0.0467	0.0744	0.0071	78.0		
CO$_2$	0.49140	0.0049	0.0078	0.0007		3.0	
H$_2$O				0.0079		14.9	
F$_{H_2}$/F$_{CO}$	1.9						
F$_{H_2O}$/F$_{CO_2}$	10.7						
ε_C	4.9						

Table D.34: Exp. 17. Feed data, GHSV = 250 $L_{CH_4}/g_{cat}\cdot h$

Compound	V	y	F
	[mL/min (STP)]	[-]	[mmol/s]
CH_4	81.7	0.2958	0.0562
O_2	40.8	0.1479	0.0281
N_2	151.9	0.5500	0.1046
Total	276.1	1.0000	0.1901

Table D.35: Exp. 17. Product data, GHSV = 250 $L_{CH_4}/g_{cat}\cdot h$, TOS = 98 min. Analysis 1

Compound	y_{GC}	y_{GC}	$y_{norm.}$	F	X	S	Y
	[vol.%]	[-]	[-]	[mmol/s]	[%]	[%]	[%]
CH_4 (FID)	6.40338	0.0640					
H_2	26.41300	0.2641		0.0647		80.6	57.5
N_2	43.11167	0.4311	0.6551	0.1046			
CO	15.35850	0.1536	0.2334	0.0372		95.6	
CH_4 (TCD)	6.63548	0.0664	0.1008	0.0161	70.8		
CO_2	0.69982	0.0070	0.0106	0.0017		4.4	
H_2O				0.0156		19.4	
F_{H_2}/F_{CO}	1.7						
F_{H_2O}/F_{CO_2}	9.2						
ε_C	2.1						

Table D.36: Exp. 17. Product data, GHSV = 250 $L_{CH_4}/g_{cat}\cdot h$, TOS = 121 min. Analysis 2

Compound	y_{GC}	y_{GC}	$y_{norm.}$	F	X	S	Y
	[vol.%]	[-]	[-]	[mmol/s]	[%]	[%]	[%]
CH_4 (FID)	6.89747	0.0690					
H_2	25.19463	0.2519		0.0615		78.9	54.7
N_2	43.11038	0.4311	0.6553	0.1046			
CO	14.78143	0.1478	0.2247	0.0359		94.9	
CH_4 (TCD)	7.09735	0.0710	0.1079	0.0172	68.7		
CO_2	0.79919	0.0080	0.0121	0.0019		5.1	
H_2O				0.0165		21.2	
F_{H_2}/F_{CO}	1.7						
F_{H_2O}/F_{CO_2}	8.5						
ε_C	2.2						

Table D.37: Exp. 17. Product data, GHSV = 250 L_{CH_4}/g_{cat}·h, TOS = 145 min. Analysis 3

Compound	y_{GC} [vol.%]	y_{GC} [-]	$y_{norm.}$ [-]	F [mmol/s]	X [%]	S [%]	Y [%]
CH_4 (FID)	7.45760	0.0746					
H_2	24.31932	0.2432		0.0584		77.1	51.9
N_2	43.65208	0.4365	0.6552	0.1046			
CO	14.39773	0.1440	0.2161	0.0345		94.0	
CH_4 (TCD)	7.65877	0.0766	0.1150	0.0183	66.7		
CO_2	0.91477	0.0091	0.0137	0.0022		6.0	
H_2O				0.0174		22.9	
F_{H_2}/F_{CO}	1.7						
F_{H_2O}/F_{CO_2}	7.9						
ε_C	2.2						

Table D.38: Exp. 17. Feed data, GHSV = 350 L_{CH_4}/g_{cat}·h

Compound	V [mL/min (STP)]	y [-]	F [mmol/s]
CH_4	114.3	0.2958	0.0787
O_2	57.2	0.1479	0.0394
N_2	212.6	0.5500	0.1464
Total	386.6	1.0000	0.2661

Table D.39: Exp. 17. Product data, GHSV = 350 L_{CH_4}/g_{cat}·h, TOS = 178 min. Analysis 1

Compound	y_{GC} [vol.%]	y_{GC} [-]	$y_{norm.}$ [-]	F [mmol/s]	X [%]	S [%]	Y [%]
CH_4 (FID)	9.30382	0.0930					
H_2	21.19302	0.2119		0.0688		71.4	43.7
O_2	0.293756	0.0029	0.0042	0.0009	97.6		
N_2	45.98390	0.4598	0.6557	0.1464			
CO	13.04207	0.1304	0.1860	0.0415		91.4	
CH_4 (TCD)	9.59128	0.0959	0.1368	0.0305	59.8		
CO_2	1.22345	0.0122	0.0174	0.0039		8.6	
H_2O				0.0275		28.6	
F_{H_2}/F_{CO}	1.7						
F_{H_2O}/F_{CO_2}	7.1						
ε_C	3.5						

Table D.40: Exp. 17. Product data, GHSV = 350 $L_{CH_4}/g_{cat} \cdot h$, TOS = 201 min. Analysis 2

Compound	y_{GC} [vol.%]	y_{GC} [-]	$y_{norm.}$ [-]	F [mmol/s]	X [%]	S [%]	Y [%]
CH_4 (FID)	10.01085	0.1001					
H_2	19.96280	0.1996		0.0635		68.8	40.4
O_2	0.36739	0.0037	0.0052	0.0012	97.1		
N_2	46.65882	0.4666	0.6552	0.1464			
CO	12.47266	0.1247	0.1751	0.0391		90.3	
CH_4 (TCD)	10.36973	0.1037	0.1456	0.0325	57.1		
CO_2	1.34352	0.0134	0.0189	0.0042		9.7	
H_2O				0.0289		31.2	
F_{H_2}/F_{CO}	1.6						
F_{H_2O}/F_{CO_2}	6.9						
ε_C	3.6						

Table D.41: Exp. 17. Product data, GHSV = 350 $L_{CH_4}/g_{cat} \cdot h$, TOS = 225 min. Analysis 3

Compound	y_{GC} [vol.%]	y_{GC} [-]	$y_{norm.}$ [-]	F [mmol/s]	X [%]	S [%]	Y [%]
CH_4 (FID)	10.79475	0.1079					
H_2	18.75379	0.1875		0.0583		65.8	37.0
O_2	0.416235	0.0042	0.0058	0.0013	96.7		
N_2	47.40020	0.4740	0.6548	0.1464			
CO	11.94293	0.1194	0.1650	0.0369		89.1	
CH_4 (TCD)	11.16284	0.1116	0.1542	0.0345	54.6		
CO_2	1.46237	0.0146	0.0202	0.0045		10.9	
H_2O				0.0302		34.2	
F_{H_2}/F_{CO}	1.6						
F_{H_2O}/F_{CO_2}	6.7						
ε_C	3.6						

Table D.42: Exp. 17. Feed data, GHSV = 400 $L_{CH_4}/g_{cat}\cdot$h

Compound	V	y	F
	[mL/min (STP)]	[-]	[mmol/s]
CH_4	130.7	0.2958	0.0900
O_2	65.3	0.1479	0.0450
N_2	243.0	0.5500	0.1673
Total	441.8	1.0000	0.3042

Table D.43: Exp. 17. Product data, GHSV = 400 $L_{CH_4}/g_{cat}\cdot$h, TOS = 253 min. Analysis 1

Compound	y_{GC}	y_{GC}	$y_{norm.}$	F	X	S	Y
	[vol.%]	[-]	[-]	[mmol/s]	[%]	[%]	[%]
CH_4 (FID)	9.30382	0.0930					
H_2	17.08852	0.1709		0.0594		62.2	33.0
O_2	0.589407	0.0059	0.0079	0.0020	95.5		
N_2	48.63683	0.4864	0.6547	0.1673			
CO	11.16338	0.1116	0.1503	0.0384		87.2	
CH_4 (TCD)	12.25341	0.1225	0.1649	0.0421	51.1		
CO_2	1.64425	0.0164	0.0221	0.0057		12.8	
H_2O				0.0362		37.9	
F_{H_2}/F_{CO}	1.6						
F_{H_2O}/F_{CO_2}	6.4						
ε_C	4.2						

Table D.44: Exp. 17. Product data, GHSV = 400 $L_{CH_4}/g_{cat}\cdot$h, TOS = 276 min. Analysis 2

Compound	y_{GC}	y_{GC}	$y_{norm.}$	F	X	S	Y
	[vol.%]	[-]	[-]	[mmol/s]	[%]	[%]	[%]
CH_4 (FID)	12.86877	0.1287					
H_2	15.61770	0.1562		0.0527		58.3	29.3
O_2	0.712714	0.0071	0.0094	0.0024	94.7		
N_2	49.55625	0.4956	0.6540	0.1673			
CO	10.45510	0.1046	0.1380	0.0353		85.4	
CH_4 (TCD)	13.25441	0.1325	0.1749	0.0447	48.0		
CO_2	1.79420	0.0179	0.0237	0.0061		14.7	
H_2O				0.0377		41.7	
F_{H_2}/F_{CO}	1.5						
F_{H_2O}/F_{CO_2}	6.2						
ε_C	4.3						

Table D.45: Exp. 17. Product data, GHSV = 400 $L_{CH_4}/g_{cat}\cdot h$, TOS = 300 min. Analysis 3

Compound	$\mathbf{y_{GC}}$ [vol.%]	$\mathbf{y_{GC}}$ [-]	$\mathbf{y_{norm.}}$ [-]	F [mmol/s]	X [%]	S [%]	Y [%]
CH_4 (FID)	14.06558	0.1407					
H_2	13.86766	0.1387		0.0450		53.3	25.0
O_2	0.867279	0.0087	0.0112	0.0029	93.6		
N_2	50.68615	0.5069	0.6531	0.1673			
CO	9.61194	0.0961	0.1238	0.0317		82.9	
CH_4 (TCD)	14.46732	0.1447	0.1864	0.0478	44.5		
CO_2	1.97986	0.0198	0.0255	0.0065		17.1	
H_2O				0.0394		46.7	
F_{H_2}/F_{CO}	1.4						
F_{H_2O}/F_{CO_2}	6.0						
ε_C	4.4						

Table D.46: Exp. 17. Feed data, GHSV = 450 $L_{CH_4}/g_{cat}\cdot h$

Compound	V [mL/min (STP)]	y [-]	F [mmol/s]
CH_4	147.0	0.2958	0.1012
O_2	73.5	0.1479	0.0506
N_2	273.4	0.5500	0.1882
Total	497.0	1.0000	0.3422

Table D.47: Exp. 17. Product data, GHSV = 450 $L_{CH_4}/g_{cat}\cdot h$, TOS = 330 min. Analysis 1

Compound	$\mathbf{y_{GC}}$ [vol.%]	$\mathbf{y_{GC}}$ [-]	$\mathbf{y_{norm.}}$ [-]	F [mmol/s]	X [%]	S [%]	Y [%]
CH_4 (FID)	15.73267	0.1573					
H_2	11.58552	0.1159		0.0471		47.7	23.3
O_2	1.39274	0.0139	0.0173	0.0045	91.2		
N_2	52.34104	0.5234	0.6499	0.1673			
CO	8.43107	0.0843	0.1047	0.0269		79.7	
CH_4 (TCD)	16.22612	0.1623	0.2015	0.0519	39.5		
CO_2	2.15099	0.0215	0.0267	0.0069		20.3	
H_2O				0.0516		52.3	
F_{H_2}/F_{CO}	1.8						
F_{H_2O}/F_{CO_2}	7.5						
ε_C	15.3						

Table D.48: Exp. 17. Product data, GHSV = 450 $L_{CH_4}/g_{cat}\cdot$h, TOS = 353 min. Analysis 2

Compound	$\mathbf{y_{GC}}$ [vol.%]	$\mathbf{y_{GC}}$ [-]	$\mathbf{y_{norm.}}$ [-]	**F** [mmol/s]	**X** [%]	**S** [%]	**Y** [%]
CH_4 (FID)	17.24136	0.1724					
H_2	9.35638	0.0936		0.0381		41.6	18.8
O_2	1.624	0.0162	0.0196	0.0051	90		
N_2	53.70556	0.5371	0.6491	0.1673			
CO	7.17356	0.0717	0.0867	0.0223		74.6	
CH_4 (TCD)	17.78301	0.1778	0.2149	0.0554	35.1		
CO_2	2.44935	0.0245	0.0296	0.0076		25.5	
H_2O				0.0535		58.4	
F_{H_2}/F_{CO}	1.7						
F_{H_2O}/F_{CO_2}	7.0						
ε_C	15.7						

Table D.49: Exp. 17. Product data, GHSV = 450 $L_{CH_4}/g_{cat}\cdot$h, TOS = 377 min. Analysis 3

Compound	$\mathbf{y_{GC}}$ [vol.%]	$\mathbf{y_{GC}}$ [-]	$\mathbf{y_{norm.}}$ [-]	**F** [mmol/s]	**X** [%]	**S** [%]	**Y** [%]
CH_4 (FID)	18.35337	0.1835					
H_2	8.01167	0.0801		0.0333		38.6	16.4
O_2	2.22649	0.0223	0.0264	0.0068	86.5		
N_2	54.47626	0.5448	0.6448	0.1673			
CO	6.43640	0.0644	0.0762	0.0198		72.7	
CH_4 (TCD)	18.92726	0.1893	0.2240	0.0581	31.8		
CO_2	2.41810	0.0242	0.0286	0.0074		27.3	
H_2O				0.0529		61.4	
F_{H_2}/F_{CO}	1.7						
F_{H_2O}/F_{CO_2}	7.1						
ε_C	15.7						

Table D.50: Exp. 17. Feed data, GHSV = 150 L$_{CH_4}$/g$_{cat}$·h

Compound	V	y	F
	[mL/min (STP)]	[-]	[mmol/s]
CH$_4$	49.0	0.2958	0.0337
O$_2$	24.5	0.1479	0.0169
N$_2$	91.1	0.5500	0.0627
Total	165.7	1.0000	0.1141

Table D.51: Exp. 17. Product data, GHSV = 150 L$_{CH_4}$/g$_{cat}$·h, TOS = 404 min. Analysis 1

Compound	y$_{GC}$	y$_{GC}$	y$_{norm.}$	F	X	S	Y
	[vol.%]	[-]	[-]	[mmol/s]	[%]	[%]	[%]
CH$_4$ (FID)	24.41721	0.2442					
H$_2$	1.01555	0.0102	0.0108	0.0011		6.4	1.6
O$_2$	4.10695	0.0411	0.0435	0.0044	74.1		
N$_2$	59.07316	0.5907	0.6261	0.0627			
CO	1.08690	0.0109	0.0115	0.0012		22.1	
CH$_4$ (TCD)	25.22214	0.2522	0.2673	0.0268	16.4		
CO$_2$	3.84158	0.0384	0.0407	0.0041		78.0	
H$_2$O				0.0157		93.6	
F$_{H_2}$/F$_{CO}$	0.9						
F$_{H_2O}$/F$_{CO_2}$	3.9						
ε_C	5.1						

Table D.52: Exp. 17. Product data, GHSV = 150 L$_{CH_4}$/g$_{cat}$·h, TOS = 427 min. Analysis 2

Compound	y$_{GC}$	y$_{GC}$	y$_{norm.}$	F	X	S	Y
	[vol.%]	[-]	[-]	[mmol/s]	[%]	[%]	[%]
CH$_4$ (FID)	24.93293	0.2493					
H$_2$	0.95709	0.0096	0.0101	0.0010		6.2	1.5
O$_2$	4.47949	0.0448	0.0474	0.0048	71.6		
N$_2$	58.67799	0.5868	0.6208	0.0627			
CO	1.03185	0.0103	0.0109	0.0011		21.9	
CH$_4$ (TCD)	25.68872	0.2569	0.2718	0.0275	15.5		
CO$_2$	3.68378	0.0368	0.0390	0.0039		78.1	
H$_2$O				0.0152		93.7	
F$_{H_2}$/F$_{CO}$	0						
F$_{H_2O}$/F$_{CO_2}$	0.6						
ε_C	3.7						

Table D.53: Exp. 17. Temperature data

$d_{b.e.}$ [cm]	T [°C]	$d_{b.e.}$ [cm]	T [°C]	$d_{b.e.}$ [cm]	T [°C]	$d_{b.e.}$ [cm]	T [°C]
GHSV = 0		**GHSV = 150**		**GHSV = 250**		**GHSV = 350**	
-2.2	770.6	-3.2	769.5	-3.2	766.5	-3.2	761.3
-1.7	770.6	-2.7	769.5	-2.7	766.7	-2.7	762.0
-1.2	770.4	-2.2	769.5	-2.2	767.3	-2.2	762.7
-0.7	770.0	-1.7	770.0	-1.7	768.0	-1.7	764.3
-0.2	768.8	-1.2	771.0	-1.2	770.0	-1.2	767.6
0.0	767.5	-0.7	774.3	-0.7	777.8	-0.7	777.5
0.3	765.9	-0.2	780.5	-0.2	790.5	-0.2	804.0
0.8	765.5	-0.1	781.8	-0.1	796.0	-0.1	814.5
1.3	765.0	0.0	782.5	0.0	799.2	0.0	818.5
1.8	763.8	0.1	781.7	0.1	802.4	0.1	830.6
2.3	761.6	0.2	779.5	0.2	803.7	0.2	835.8
2.8	759.0	0.3	773.2	0.3	796.5	0.3	827.5
		0.8	766.5	0.8	787.0	0.4	822.0
		1.3	764.1	1.3	777.2	0.8	792.3
		1.8	762.0	1.8	770.0	1.3	777.2
		2.3	759.2	2.3	761.0	1.8	769.3
		2.8	756.5	2.8	757.4	2.3	763.2
						2.8	757.0
		GHSV = 400		**GHSV = 450**		**GHSV = 150**	
		-3.2	754.8	-3.2	740.3	-3.2	753.0
		-2.7	756.0	-2.7	741.8	-2.7	753.5
		-2.2	757.0	-2.2	743.2	-2.2	754.0
		-1.7	759.0	-1.7	745.7	-1.7	755.3
		-1.2	764.4	-1.2	751	-1.2	758.5
		-0.7	777.8	-0.7	766.6	-0.7	766.8
		-0.2	813.4	-0.2	818.2	-0.2	793.0
		-0.1	830.0	-0.1	832.7	-0.1	797.0
		0.0	847.5	0.0	853.5	0	805.5
		0.1	858.3	0.1	866.8	0.1	809.5
		0.2	866.8	0.2	879.5	0.2	812.6
		0.3	862.3	0.3	877.8	0.3	809.5
		0.8	806.0	0.8	813.3	0.8	772.2
		1.3	784.5	1.3	780	1.3	758.3
		1.8	773.2	1.8	768	1.8	750.7
		2.3	764.0	2.3	758	2.3	745.3
		2.8	757.0	2.8	751	2.8	741.0

Experiment 18

Catalyst: Monolithic $Co/CeO_2-Al_2O_3$
GHSV = 75 $L_{CH_4}/g_{cat}\cdot h$
Reduction: 50 mL/min 50 vol.% H_2 in N_2, 10 K/min, 973 K, 2h
$T_{furnace}$ = 1023 K

Table D.54: Exp. 18. Feed data

Compound	V	y	F
	[mL/min (STP)]	[-]	[mmol/s]
CH_4	166.7	0.2958	0.1148
O_2	83.3	0.1479	0.0574
N_2	309.9	0.5500	0.2134
Total	563.5	1.0000	0.3880

Table D.55: Exp. 18. Product data, TOS = 20 min

Compound	y_{GC}	y_{GC}	$y_{norm.}$	F	X	S	Y
	[vol.%]	[-]	[-]	[mmol/s]	[%]	[%]	[%]
CH_4 (FID)	5.65530	0.0566					
H_2	26.52139	0.2652				82.7	61.8
N_2	42.35700	0.4236	0.6599	0.2134			
CO	15.23627	0.1524	0.2374	0.0768		94.8	
CH_4 (TCD)	5.76368	0.0576	0.0898	0.0290	73.6		
CO_2	0.83066	0.0083	0.0129	0.0042		5.2	
H_2O						17.3	
F_{H_2}/F_{CO}	1.9						
F_{H_2O}/F_{CO_2}	7.1						
ε_C	4.2						

Table D.56: Exp. 18. Product data, TOS = 43 min

Compound	y_{GC}	y_{GC}	$y_{norm.}$	F	X	S	Y
	[vol.%]	[-]	[-]	[mmol/s]	[%]	[%]	[%]
CH_4 (FID)	6.22378	0.0622					
H_2	25.85705	0.2586				81.1	58.9
N_2	43.25364	0.4325	0.6601	0.2134			
CO	14.97149	0.1497	0.2285	0.0739		94.1	
CH_4 (TCD)	6.36192	0.0636	0.0971	0.0314	71.4		
CO_2	0.94347	0.0094	0.0144	0.0047		5.9	
H_2O						18.9	
F_{H_2}/F_{CO}	1.8						
F_{H_2O}/F_{CO_2}	6.8						
ε_C	4.2						

Table D.57: Exp. 18. Product data, TOS = 66 min

Compound	y_{GC} [vol.%]	y_{GC} [-]	$y_{norm.}$ [-]	F [mmol/s]	X [%]	S [%]	Y [%]
CH_4 (FID)	6.67019	0.0667					
H_2	25.21102	0.2521				79.7	56.7
N_2	43.78924	0.4379	0.6600	0.2134			
CO	14.70402	0.1470	0.2216	0.0717		93.4	
CH_4 (TCD)	6.81776	0.0682	0.1028	0.0332	69.8		
CO_2	1.03211	0.0103	0.0156	0.0050		6.6	
H_2O						20.3	
F_{H_2}/F_{CO}	1.8						
F_{H_2O}/F_{CO_2}	6.6						
ε_C	4.2						

Table D.58: Exp. 18. Product data, TOS = 93 min

Compound	y_{GC} [vol.%]	y_{GC} [-]	$y_{norm.}$ [-]	F [mmol/s]	X [%]	S [%]	Y [%]
CH_4 (FID)	7.27604	0.0728					
H_2	24.32662	0.2433		0.1237		78.1	53.9
N_2	44.41157	0.4441	0.6601	0.2134			
CO	14.31895	0.1432	0.2128	0.0688		92.5	
CH_4 (TCD)	7.38795	0.0739	0.1098	0.0355	67.7		
CO_2	1.16137	0.0116	0.0173	0.0056		7.5	
H_2O				0.0348		22.0	
F_{H_2}/F_{CO}	1.8						
F_{H_2O}/F_{CO_2}	6.2						
ε_C	4.3						

Table D.59: Exp. 18. Product data, TOS = 117 min

Compound	y_{GC} [vol.%]	y_{GC} [-]	$y_{norm.}$ [-]	F [mmol/s]	X [%]	S [%]	Y [%]
CH_4 (FID)	7.62628	0.0763					
H_2	23.73046	0.2373		0.1190		76.7	51.9
N_2	44.92350	0.4492	0.6602	0.2134			
CO	14.07545	0.1408	0.2068	0.0669		92.0	
CH_4 (TCD)	7.81888	0.0782	0.1149	0.0371	66.2		
CO_2	1.23165	0.0123	0.0181	0.0059		8.1	
H_2O				0.0362		23.3	
F_{H_2}/F_{CO}	1.8						
F_{H_2O}/F_{CO_2}	6.2						
ε_C	4.3						

Table D.60: Exp. 18. Product data, TOS = 141 min

Compound	y_{GC} [vol.%]	y_{GC} [-]	$y_{norm.}$ [-]	F [mmol/s]	X [%]	S [%]	Y [%]
CH_4 (FID)	7.90545	0.0791					
H_2	23.25627	0.2326		0.1159		75.7	50.5
N_2	45.14907	0.4515	0.6601	0.2134			
CO	13.89302	0.1389	0.2031	0.0657		91.7	
CH_4 (TCD)	8.08638	0.0809	0.1182	0.0382	65.2		
CO_2	1.26541	0.0127	0.0185	0.0060		8.4	
H_2O				0.0371		24.3	
F_{H_2}/F_{CO}	1.8						
F_{H_2O}/F_{CO_2}	6.2						
ε_C	4.3						

Table D.61: Exp. 18. Product data, TOS = 165 min

Compound	y_{GC} [vol.%]	y_{GC} [-]	$y_{norm.}$ [-]	F [mmol/s]	X [%]	S [%]	Y [%]
CH_4 (FID)	8.20171	0.0820					
H_2	22.92471	0.2292		0.1134		75.0	49.4
N_2	45.43115	0.4543	0.6601	0.2134			
CO	13.76351	0.1376	0.2000	0.0646		91.4	
CH_4 (TCD)	8.33200	0.0833	0.1211	0.0391	64.4		
CO_2	1.30269	0.0130	0.0189	0.0061		8.7	
H_2O				0.0379		25.0	
F_{H_2}/F_{CO}	1.8						
F_{H_2O}/F_{CO_2}	6.2						
ε_C	4.2						

Table D.62: Exp. 18. Product data, TOS = 188 min

Compound	y_{GC} [vol.%]	y_{GC} [-]	$y_{norm.}$ [-]	F [mmol/s]	X [%]	S [%]	Y [%]
CH_4 (FID)	8.36258	0.0836					
H_2	22.58740	0.2259		0.1112		74.3	48.5
N_2	45.66332	0.4566	0.6601	0.2134			
CO	13.64696	0.1365	0.1973	0.0638		91.1	
CH_4 (TCD)	8.53496	0.0853	0.1234	0.0399	63.7		
CO_2	1.33308	0.0133	0.0193	0.0062		8.9	
H_2O				0.0385		25.7	
F_{H_2}/F_{CO}	1.7						
F_{H_2O}/F_{CO_2}	6.2						
ε_C	4.2						

Table D.63: Exp. 18. Product data, TOS = 212 min

Compound	y_{GC} [vol.%]	y_{GC} [-]	$y_{norm.}$ [-]	F [mmol/s]	X [%]	S [%]	Y [%]
CH_4 (FID)	8.51483	0.0851					
H_2	22.33921	0.2234		0.1095		71.8	47.7
N_2	45.80784	0.4581	0.6599	0.2134			
CO	13.56216	0.1356	0.1954	0.0632		90.9	
CH_4 (TCD)	8.69260	0.0869	0.1252	0.0405	63.2		
CO_2	1.35101	0.0135	0.0195	0.0063		9.1	
H_2O				0.0390		26.3	
F_{H_2}/F_{CO}	1.7						
F_{H_2O}/F_{CO_2}	6.2						
ε_C	4.2						

Table D.64: Exp. 18. Product data, TOS = 235 min

Compound	y_{GC} [vol.%]	y_{GC} [-]	$y_{norm.}$ [-]	F [mmol/s]	X [%]	S [%]	Y [%]
CH_4 (FID)	8.68445	0.0868					
H_2	22.09340	0.2209		0.1077		73.1	46.9
N_2	46.05902	0.4606	0.6602	0.2134			
CO	13.45982	0.1346	0.1929	0.0624		90.7	
CH_4 (TCD)	8.86859	0.0887	0.1271	0.0411	62.6		
CO_2	1.37661	0.0138	0.0197	0.0064		9.3	
H_2O				0.0396		26.9	
F_{H_2}/F_{CO}	1.7						
F_{H_2O}/F_{CO_2}	6.2						
ε_C	4.2						

Table D.65: Exp. 18. Product data, TOS = 258 min

Compound	y_{GC} [vol.%]	y_{GC} [-]	$y_{norm.}$ [-]	F [mmol/s]	X [%]	S [%]	Y [%]
CH_4 (FID)	8.83333	0.0883					
H_2	21.81531	0.2182		0.1058		72.5	46.1
N_2	46.22755	0.4623	0.6600	0.2134			
CO	13.36730	0.1337	0.1908	0.0617		90.5	
CH_4 (TCD)	9.05138	0.0905	0.1292	0.0418	62.0		
CO_2	1.39815	0.0140	0.0200	0.0065		9.5	
H_2O				0.0401		27.5	
F_{H_2}/F_{CO}	1.7						
F_{H_2O}/F_{CO_2}	6.2						
ε_C	4.2						

Table D.66: Exp. 18. Product data, TOS = 282 min

Compound	y_{GC} [vol.%]	y_{GC} [-]	$y_{norm.}$ [-]	F [mmol/s]	X [%]	S [%]	Y [%]
CH_4 (FID)	9.00413	0.0900					
H_2	21.57338	0.2157		0.1039		71.9	45.3
N_2	46.44846	0.4645	0.6598	0.2134			
CO	13.27724	0.1328	0.1886	0.0610		90.3	
CH_4 (TCD)	9.24096	0.0924	0.1313	0.0425	61.4		
CO_2	1.42612	0.0143	0.0203	0.0066		9.7	
H_2O				0.0407		28.1	
F_{H_2}/F_{CO}	1.7						
F_{H_2O}/F_{CO_2}	6.2						
ε_C	4.1						

Table D.67: Exp. 18. Temperature data

$d_{bed\ entrance}$ [cm]	T [°C]
-2.6	753
-2.5	754.7
-2	760.5
-1.5	767.5
-1	786.8
-0.5	832.3
-0.3	874.2
-0.1	888.2
0	896.6
0.1	897.2
0.2	891.6
0.3	880.6
0.4	868
0.5	857.2
0.6	843.5
0.7	832.4
0.8	814.8
0.9	799.2
1	795
1.5	771.5
2	762
2.5	759.8
3	758
3.5	757

Experiment 19

Catalyst: $Co/CeO_2-Al_2O_3$ (1273 K)
$m_{catalyst}$ = 0.0953 g
GHSV = 75 L_{CH_4}/g_{cat}·h
Reduction: 50 mL/min 50 vol.% H_2 in N_2, 10 K/min, 973 K, 2h
$T_{furnace}$ = 1023 K

Table D.68: Exp. 19. Feed data

Compound	V	y	F
	[mL/min (STP)]	[-]	[mmol/s]
CH_4	119.1	0.2958	0.0820
O_2	59.6	0.1479	0.0410
N_2	221.5	0.5500	0.1525
Total	402.8	1.0000	0.2773

Table D.69: Exp. 19. Product data, TOS = 20 min

Compound	y_{GC}	y_{GC}	$y_{norm.}$	F	X	S	Y
	[vol.%]	[-]	[-]	[mmol/s]	[%]	[%]	[%]
CH_4 (FID)	4.21818	0.0422					
H_2	29.07686	0.2908		0.1139		86.6	69.5
N_2	41.45171	0.4145	0.6582	0.1525			
CO	16.70295	0.1670	0.2652	0.0615		97.6	
CH_4 (TCD)	4.41949	0.0442	0.0702	0.0163	79.5		
CO_2	0.40325	0.0040	0.0064	0.0015		2.4	
H_2O				0.0176		13.4	
F_{H_2}/F_{CO}	1.9						
F_{H_2O}/F_{CO_2}	11.9						
ε_C	3.4						

Table D.70: Exp. 19. Product data, TOS = 43.5 min

Compound	y_{GC}	y_{GC}	$y_{norm.}$	F	X	S	Y
	[vol.%]	[-]	[-]	[mmol/s]	[%]	[%]	[%]
CH_4 (FID)	4.23144	0.0423					
H_2	29.20115	0.2920		0.1141		86.7	69.6
N_2	41.44205	0.4144	0.6581	0.1525			
CO	16.72784	0.1673	0.2656	0.0616		97.7	
CH_4 (TCD)	4.40389	0.0440	0.0699	0.0162	79.6		
CO_2	0.39950	0.0040	0.0063	0.0015		2.3	
H_2O				0.0175		13.3	
F_{H_2}/F_{CO}	1.9						
F_{H_2O}/F_{CO_2}	11.9						
ε_C	3.4						

Table D.71: Exp. 19. Product data, TOS = 67 min

Compound	y_{GC} [vol.%]	y_{GC} [-]	$y_{norm.}$ [-]	F [mmol/s]	X [%]	S [%]	Y [%]
CH_4 (FID)	4.31026	0.0431					
H_2	29.83804	0.2984		0.1141		86.7	69.6
N_2	42.24395	0.4224	0.6579	0.1525			
CO	17.06227	0.1706	0.2657	0.0616		97.7	
CH_4 (TCD)	4.49619	0.0450	0.0700	0.0162	79.5		
CO_2	0.40718	0.0041	0.0063	0.0015		2.3	
H_2O				0.0175		13.3	
F_{H_2}/F_{CO}	1.9						
F_{H_2O}/F_{CO_2}	11.9						
ε_C	3.3						

Table D.72: Exp. 19. Product data, TOS = 90.5 min

Compound	y_{GC} [vol.%]	y_{GC} [-]	$y_{norm.}$ [-]	F [mmol/s]	X [%]	S [%]	Y [%]
CH_4 (FID)	4.32529	0.0433					
H_2	29.90699	0.2991		0.1141		86.7	69.5
N_2	42.30182	0.4230	0.6577	0.1525			
CO	17.09220	0.1709	0.2658	0.0616		97.7	
CH_4 (TCD)	4.51105	0.0451	0.0701	0.0163	79.5		
CO_2	0.41037	0.0041	0.0064	0.0015		2.3	
H_2O				0.0174		13.3	
F_{H_2}/F_{CO}	1.9						
F_{H_2O}/F_{CO_2}	11.8						
ε_C	3.2						

Table D.73: Exp. 19. Product data, TOS = 114 min

Compound	y_{GC} [vol.%]	y_{GC} [-]	$y_{norm.}$ [-]	F [mmol/s]	X [%]	S [%]	Y [%]
CH_4 (FID)	4.30727	0.0431					
H_2	29.91702	0.2992		0.1141		86.7	69.5
N_2	42.34386	0.4234	0.6578	0.1525			
CO	17.10200	0.1710	0.2657	0.0616		97.6	
CH_4 (TCD)	4.51677	0.0452	0.0702	0.0163	79.5		
CO_2	0.41389	0.0041	0.0064	0.0015		2.3	
H_2O				0.0174		13.3	
F_{H_2}/F_{CO}	1.9						
F_{H_2O}/F_{CO_2}	11.7						
ε_C	3.2						

Table D.74: Exp. 19. Product data, TOS = 137.5 min

Compound	y_{GC} [vol.%]	y_{GC} [-]	$y_{norm.}$ [-]	F [mmol/s]	X [%]	S [%]	Y [%]
CH_4 (FID)	4.33104	0.0433					
H_2	29.90007	0.2990		0.1140		86.7	69.5
N_2	42.33013	0.4233	0.6577	0.1525			
CO	17.09554	0.1710	0.2656	0.0616		97.6	
CH_4 (TCD)	4.51888	0.0452	0.0702	0.0163	79.5		
CO_2	0.41572	0.0042	0.0065	0.0015		2.4	
H_2O				0.0174		13.3	
F_{H_2}/F_{CO}	1.9						
F_{H_2O}/F_{CO_2}	11.6						
ε_C	3.2						

Table D.75: Exp. 19. Product data, TOS = 161 min

Compound	y_{GC} [vol.%]	y_{GC} [-]	$y_{norm.}$ [-]	F [mmol/s]	X [%]	S [%]	Y [%]
CH_4 (FID)	4.32335	0.0432					
H_2	29.85996	0.2986		0.1138		86.7	69.4
N_2	42.30262	0.4230	0.6575	0.1525			
CO	17.08043	0.1708	0.2655	0.0616		97.6	
CH_4 (TCD)	4.54312	0.0454	0.0706	0.0164	79.4		
CO_2	0.41730	0.0042	0.0065	0.0015		2.4	
H_2O				0.0174		13.3	
F_{H_2}/F_{CO}	1.9						
F_{H_2O}/F_{CO_2}	11.6						
ε_C	3.1						

Table D.76: Exp. 19. Product data, TOS = 184.5 min

Compound	y_{GC} [vol.%]	y_{GC} [-]	$y_{norm.}$ [-]	F [mmol/s]	X [%]	S [%]	Y [%]
CH_4 (FID)	4.31464	0.0431					
H_2	29.80962	0.2981		0.1138		86.7	69.4
N_2	42.29908	0.4230	0.6575	0.1525			
CO	17.07003	0.1707	0.2653	0.0615		97.6	
CH_4 (TCD)	4.54661	0.0455	0.0707	0.0164	79.4		
CO_2	0.41874	0.0042	0.0065	0.0015		2.4	
H_2O				0.0175		13.3	
F_{H_2}/F_{CO}	1.9						
F_{H_2O}/F_{CO_2}	11.6						
ε_C	3.1						

Table D.77: Exp. 19. Product data, TOS = 208 min

Compound	y_{GC} [vol.%]	y_{GC} [-]	$y_{norm.}$ [-]	F [mmol/s]	X [%]	S [%]	Y [%]
CH_4 (FID)	4.37308	0.0437					
H_2	29.86480	0.2986		0.1137		86.7	69.3
N_2	42.36307	0.4236	0.6575	0.1525			
CO	17.07712	0.1708	0.2650	0.0615		97.6	
CH_4 (TCD)	4.56366	0.0456	0.0708	0.0164	79.3		
CO_2	0.42600	0.0043	0.0066	0.0015		2.4	
H_2O				0.0175		13.3	
F_{H_2}/F_{CO}	1.9						
F_{H_2O}/F_{CO_2}	11.4						
ε_C	3.1						

Table D.78: Exp. 19. Product data, TOS = 231.5 min

Compound	y_{GC} [vol.%]	y_{GC} [-]	$y_{norm.}$ [-]	F [mmol/s]	X [%]	S [%]	Y [%]
CH_4 (FID)	4.38328	0.0438					
H_2	29.79834	0.2980		0.1136		86.7	69.2
N_2	42.32066	0.4232	0.6573	0.1525			
CO	17.06091	0.1706	0.2650	0.0615		97.6	
CH_4 (TCD)	4.57897	0.0458	0.0711	0.0165	79.3		
CO_2	0.42731	0.0043	0.0066	0.0015		2.4	
H_2O				0.0175		13.3	
F_{H_2}/F_{CO}	1.9						
F_{H_2O}/F_{CO_2}	11.3						
ε_C	3.0						

Table D.79: Exp. 19. Product data, TOS = 255 min

Compound	y_{GC} [vol.%]	y_{GC} [-]	$y_{norm.}$ [-]	F [mmol/s]	X [%]	S [%]	Y [%]
CH_4 (FID)	4.40805	0.0441					
H_2	30.09847	0.3010		0.1135		86.7	69.2
N_2	42.71077	0.4271	0.6572	0.1525			
CO	17.20940	0.1721	0.2648	0.0615		97.5	
CH_4 (TCD)	4.62761	0.0463	0.0712	0.0165	79.2		
CO_2	0.43664	0.0044	0.0067	0.0016		2.5	
H_2O				0.0174		13.3	
F_{H_2}/F_{CO}	1.9						
F_{H_2O}/F_{CO_2}	11.2						
ε_C	3.0						

Table D.80: Exp. 19. Product data, TOS = 278.5 min

Compound	y_{GC} [vol.%]	y_{GC} [-]	$y_{norm.}$ [-]	F [mmol/s]	X [%]	S [%]	Y [%]
CH_4 (FID)	4.33876	0.0434					
H_2	29.79069	0.2979		0.1138		86.7	69.4
N_2	42.40401	0.4240	0.6581	0.1525			
CO	17.04185	0.1704	0.2645	0.0613		97.5	
CH_4 (TCD)	4.54419	0.0454	0.0705	0.0163	79.4		
CO_2	0.44277	0.0044	0.0069	0.0016		2.5	
H_2O				0.0175		13.4	
F_{H_2}/F_{CO}	1.9						
F_{H_2O}/F_{CO_2}	11.2						
ε_C	3.4						

Table D.81: Exp. 19. Product data, TOS = 302 min

Compound	y_{GC} [vol.%]	y_{GC} [-]	$y_{norm.}$ [-]	F [mmol/s]	X [%]	S [%]	Y [%]
CH_4 (FID)	4.33656	0.0434					
H_2	29.76854	0.2977		0.1138		86.6	69.4
N_2	42.41900	0.4242	0.6581	0.1525			
CO	17.03341	0.1703	0.2643	0.0612		97.4	
CH_4 (TCD)	4.55159	0.0455	0.0706	0.0164	79.3		
CO_2	0.44979	0.0045	0.0070	0.0016		2.6	
H_2O				0.0175		13.4	
F_{H_2}/F_{CO}	1.9						
F_{H_2O}/F_{CO_2}	10.9						
ε_C	3.4						

Table D.82: Exp. 19. Product data, TOS = 325.5 min

Compound	y_{GC} [vol.%]	y_{GC} [-]	$y_{norm.}$ [-]	F [mmol/s]	X [%]	S [%]	Y [%]
CH_4 (FID)	4.34470	0.0434					
H_2	29.71357	0.2971		0.1136		86.6	69.2
N_2	42.42237	0.4242	0.6581	0.1525			
CO	17.01866	0.1702	0.2640	0.0612		97.4	
CH_4 (TCD)	4.57214	0.0457	0.0709	0.0164	79.3		
CO_2	0.44919	0.0045	0.0070	0.0016		2.6	
H_2O				0.0176		13.4	
F_{H_2}/F_{CO}	1.9						
F_{H_2O}/F_{CO_2}	10.9						
ε_C	3.4						

Table D.83: Exp. 19. Product data, TOS = 349 min

Compound	y_{GC} [vol.%]	y_{GC} [-]	$y_{norm.}$ [-]	F [mmol/s]	X [%]	S [%]	Y [%]
CH_4 (FID)	4.38009	0.0438					
H_2	29.66823	0.2967		0.1134		86.6	69.2
N_2	42.40797	0.4241	0.6580	0.1525			
CO	17.00164	0.1700	0.2638	0.0611		97.4	
CH_4 (TCD)	4.58597	0.0459	0.0712	0.0165	79.2		
CO_2	0.45479	0.0045	0.0071	0.0016		2.6	
H_2O				0.0176		13.4	
F_{H_2}/F_{CO}	1.9						
F_{H_2O}/F_{CO_2}	10.8						
ε_C	3.4						

Table D.84: Exp. 19. Temperature data

TOS [min]	$T_{bed\ entrance}$ [°C]
20.0	769.0
43.5	772.0
67.0	773.7
90.5	775.0
114.0	775.7
137.5	776.4
161.0	777.0
184.5	777.5
208.0	777.8
231.5	778.0
255.0	778.7
278.5	779.2
302.0	779.5
325.5	780.0

Appendix E

Risk assessment

NTNU		Hazardous activity identification process	Risikovurdering	Nummer	Dato
HMS			HMS-avd.	HMSRV2601	
			Godkjent av	Side	Erstatter

Unit: _Kjemisk prosessteknologi_   **Date:** _02.11.2012_

Line manager: _Øyvind Gregersen_

Participants in the identification process (including their function): Sophie Glas (student)

De Chen (supervisor)

Short description of the main activity/main process: Synthesis and characterization of Co/CeO2-Al2O3 catalyst

ID no.	Activity/process	Responsible person	Laws, regulations etc.	Existing documentation	Existing safety measures	Comment
1	Handling chemicals (Ce(NO3)2 6H2O, citric acid, PEG, Co(NO3)2 6H2O, NaOH, HNO3, EG, Al2O3, acetone)	Sophie Glas	"Kjemikalieforskriften"	MSDS	Goggles, gloves, lab coat, fume hood	
2	Synthesis of catalyst	SG	"Kjemikalieforskriften"	MSDS	Goggles, gloves, lab coat, fume hood	
3	Heating/evaporation of reaction mixture	SG	"Kjemikalieforskriften"	MSDS	Goggles, fume hood	Make sure that the vapour does not escape into the room

4	Calcination in high temperature furnace	Georg Voß		Apparatus card, MSDS	Goggles, insulating gloves	Done in high temperature furnace
5	BET	Magnus Rønning, Karing W. Dragsten		Apparatus card, MSDS	Safety goggles, gloves, insulating gloves, lab coat	
6	XRD	Julian Tolchard		Apparatus card, MSDS	Lab coat, gloves, goggles	
7	TPR	Thorbjørn Gjervan		Apparatus card, MSDS	Lab coat, gloves, goggles, gas detector	Use of 7% H2 in Ar

NTNU		Risk assessment		Utarbeidet av	Nummer		Dato
				HMS-avd.	HMSRV2603		04-02-11
HMS /KS				Godkjent av	Side	Erstatter	

Unit: _Kjemisk prosessteknologi_   **Date:** _02.11.2012_

Line manager: _Øyvind Gregersen_

Participants in the identification process (including their function): _Sophie Glas (student)_

De Chen (supervisor)

Signatures:

ID no.	Activity from the identification process form	Potential undesirable incident/strain	Likelihood:	Consequence:				Risk value	Comments/status Suggested measures
			Likelihood (1-5)	Human (A-E)	Environment (A-E)	Economy/ material (A-E)	Reputation (A-E)	Human	
1	Handling chemicals (Ce(NO3)2 6H2O, citric acid, PEG, Co(NO3)2 6H2O, NaOH, HNO3, EG, Al2O3, acetone)	Spilling of the chemicals, contact with skin, respiratory system	2	C	A	A		2B	Avoid direct contact with the chemicals, vapors and dust. Do not let chemicals enter the drain.
2	Synthesis of catalyst	Spilling of the chemicals, contact with skin, respiratory system	2	B	A	A		1B	Avoid direct contact.
3	Heating/evaporation of reaction mixture	Inhale vapor, burning	1	C	A	A		1B	Evaporation in a designated area.

4	Calcination in high temperature furnace	Burning injuries	1	A	A	A	1A	Wait until object is cooled down.Use insulating gloves when handling hot objects. Plan where to put the hot objects.
5	BET	Spilling of liquid N2 (77K)	2	C	A	A	1B	Careful when pooring N2 into flask
6	XRD	Spilling of catalyst powder, contact with skin, X-rays	1	B	B	A	1B	Deposit spilled powder in designated bins. Clean with acetone.
7	TPR	Gas leak, contact with hot object, temperature runaway	3	A	A	A	3A	Check for gas leak at every junction, especially near the reactor. If incident, close gas flask and abort the experiment

NTNU		Risikovurdering	Nummer		Dato
		HMS-avd.	HMSRV2601		
HMS	Hazardous activity identification process	Godkjent av	Side	Erstatter	

Unit: _Kjemisk prosessteknologi_   **Date:**   26.11.2012

Line manager: _Øyvind Gregersen_

Participants in the identification process (including their function): Sophie Glas (student), De Chen (supervisor), Karin W. Dragsten

Short description of the main activity/main process: Catalytic partial oxidation of methane at moderate temperatures

ID no.	Activity/process	Responsible person	Laws, regulations etc.	Existing documentation	Existing safety measures	Comment
1	Assembling/use of flamable gases: H2, CH4	Sophie Glas/De Chen		MSDS (H2: EIGA067A, CH4: EIGA078A)	Room detector, local detector, leak testing, gloves, goggles, lab coat	
2	Assembling/use of flamable gases: H2, CH4	Sophie Glas/De Chen		MSDS (H2: EIGA067A, CH4: EIGA078A)	Room detector, local detector, leak testing, gloves, goggles, lab coat	
3	Assembling/use of non-toxic and inert gases: N2, air	Sophie Glas/De Chen		MSDS (N2: EIGA089A, O2: EIGA097A)	Room detector, local detector, leak testing, gloves, goggles, lab coat	

4	Heating				Sophie Glas/De Chen		Thermocouples, Eurotherm	Upper temperature limit, furnace off when exceeding limit
5	GC	User manual		Sophie Glas/De Chen		
6	Handling of catalyst	MSDS		Sophie Glas/De Chen		Gloves, goggles, lab coat, mask for nose and mouth	Filling/emptying reactor

NTNU		Risk assessment		Utarbeidet av	Nummer	Dato
![HMS /KS]				HMS-avd.	HMSRV2603	04-02-11
				Godkjent av	Side	Erstatter

Unit: _Kjemisk prosessteknologi_ **Date:** 26.11.2012

Line manager: _Øyvind Gregersen_

Participants in the identification process (including their function): _Sophie Glas (student), De Chen (supervisor), Karin W. Dragsten_

Signatures:

ID no.	Activity from the identification process form	Potential undesirable incident/strain	Likelihood: Likelihood (1-5)	Consequence: Human (A-E)	Consequence: Environment (A-E)	Consequence: Economy/ material (A-E)	Consequence: Reputation (A-E)	Risk value Human	Comments/status Suggested measures
1	Assembling/use of flamable gases: H2, CH4	Leakage	3	A	A	A		A3	
2	Assembling/use of flamable gases: H2, CH4	Fire	1	B	C	C		B1	Control amounts of gas, monitor temperature
3	Assembling/use of non-toxic and inert gases: N2, air	Leakage	3	A	A	A		A3	

#	Activity	Hazard						Code	Measure
4	Heating	Temperature runaway	2	A	B	B		A2	Pre-set temperature program, control program before experiment
5	GC	No gas flow	2	A	A	B		A2	Always carrier gas, check pressure in gas containers
6	Handling of catalyst	Spilling on skin, inhalation	2	B	B	A		2B	Transport catalyst in closed containers, use designated equipment.

Operating Instructions

Instrument/Apparatus: 2.13 Metan OX (Catalytic partial oxidation of methane)	
Serial Number: 2.13 (Metan OX)	Placement: Chemistry hall D
Original Manual: None	

Log book with signature for training & maintenance:

Risk Evaluation
Date: 16.10.2012
Archived:

Compulsory Protection Equipment:		Hazards:	
Safety Goggles	x	Fire	x
Gloves	x	Chemicals/Gasses	x
Hearing Protection		Electricity/Power	x
Protective Clothing	x	Temperature/Pressure	x
Breathing Protection		Cutting/Crushing	
Shielding		Rotating Equipment	
Other		Hazardous Waste	x
None		Beyond regular working hours	x
		Others	
		None	

Operating Instructions
Reduce catalyst in situ with H2
Catalytic partial oxidation of methane.
Methane-air-mixture: CH4:O2:N2 of 2:1:3.72
Heat reactor from 573 K to 1173 K at 10 K/min
Keep temperature constant for a certain number of hours

Emergency Procedure
(Emergency Stop Procedure, Image of Switches/Stop Procedure):
Emergency stop: Red button on electricity box, electricity shut-down of furnace and mass flow controllers
Close gas bottles manually

Maintenance Routines
Frequency: When needed
Service Agreements: None
Maintenance Contact: None
Maintenance Described In Seperate Attachment None outside mainentance

Equipment Responsible:	Deputy:
Name: De Chen	Name: Sophie Glas
Telephone: 73593149	Telephone:
Mobile: 48222428	Mobile: 92683961
Signature:	Signature:

Controlled & Updated:

Date:	Date:	Date:
Date:	Date:	Date: